# Faculty of Science and Technology

## MASTER'S THESIS

| | |
|---|---|
| Study program/ Specialization : <br><br> **Engineering Structures and Materials/** <br> **Civil Engineering** | Autumn semester, 2019 <br><br> **Open / Restricted access** |
| <br> Writer: **Yanni Zhang** <br> | <br><br> ......................................................... <br> (Writer's signature) |
| Faculty Supervisor: **Prof. Muk Chen Ong** <br><br> Co-Supervisor(s): **Dr. Guang Yin** | |
| Thesis title: <br><br> Numerical Simulations of Flow around Subsea Covers at High Reynolds Numbers | |
| Credit (ECTS) : <br><br> **30** | |
| Keywords: <br><br> RANS; turbulent boundary layer flow; high Reynolds; <br><br> hydrodynamic quantities; subsea structure | Pages : ..........69......... <br><br> +Appendix: …42……. <br><br> Stavanger, 15$^{th}$ Jan 2020 |

# Abstract

Glass Reinforced Plastic (GRP) covers are widely used to protect the subsea equipment from external damage. In this work, numerical simulations of a fully developed turbulent boundary layer flow over square and trapezoidal wall-mounted GRP covers are performed using a open source tool: OpenFOAM. The aim of this master thesis is to evaluate the effect on flow characteristics from the shape of the structure, the boundary layer thickness and the Reynolds number. The trapezoidal obstacles with different slope angles are under investigation. Hydrodynamic quantities of turbulent boundary layer flow with various boundary layer thicknesses ($\delta/D$=0.73, 1.96 and 2.52) are examined. The structures are subjected into turbulent flows at Reynolds numbers of $0.5 \times 10^6$, $1 \times 10^6$ and $2 \times 10^6$ according to the free stream velocity and dimension of structures.

Three classes of mesh sets were conducted in OpenFOAM supported mesh tool, GMSH. Two-dimensional Reynolds-averaged Navier-Stokes (RANS) equations are solved by $k - \omega$ Shear Stress Transport ($k - \omega$ SST) turbulence model. The square cylinder geometry with characteristic length D has been investigated to validate the capability of RANS $k - \omega$ SST model. The obtained results in present study show good agreements with previously published experiment data. The results of the streamlines, pressure and velocity distributions were also analyzed for different geometries.

# Acknowledgements

This thesis completes my master's degree in Engineering Structures and Materials at the University of Stavanger.

I want to express my deepest appreciation to my supervisor Prof. Muk Chen Ong who has provided me with help and guidance throughout the semester. This thesis could not reach its present form without his consistent inspiration.

Furthermore, I would like to thank Dr. Yin for his help with academic and technical support as well as his patience to answer all my questions throughout the duration of my work.

Last but not least, I am grateful to all my friends who have helped and encouraged me and special thanks to my family for supporting me to overcome the difficult time in the past.

# Table of Contents

# List of Figures

# List of Table

# Abbreviations

| | |
|---|---|
| 2D | Two-Dimensional |
| 3D | Three-Dimensional |
| CD | Cross-Diffusion |
| CFD | Computational Fluid Dynamics |
| CFL | Courant-Friedrichs-Lewy |
| DNS | Direct Numerical Simulation |
| FVM | Finite Volume Method |
| GRP | Glass Reinforced Plastic |
| LES | Large Eddy Simulation |
| OpenFOAM | Open Source Field Operation and Mainipulation |
| PDE | Partial Differential Equation |
| RANS | Reynolds-Averaged Navier-Stokes |
| SIMPLE | Semi-Implicit Method for Pressure Linked Equations |
| SST | Shear Stress Transport |

# List of Symbols

| | | |
|---|---|---|
| $\phi_1$ | Corresponding Constant | [-] |
| $\phi_2$ | Constant in $k - \varepsilon$ Model | [-] |
| $C_D$ | Drag Force Coefficient | [-] |
| $C_L$ | Lift Force Coefficient | [-] |
| $F_d$ | Drag Force | [N] |
| $F_l$ | Lift Force | [N] |
| $Re_{cr}$ | Engineering Critical Reynolds Number | [-] |
| $U_\infty$ | Free Stream Flow Velocity | [m/s] |
| $u'$ | Fluctuating Velocity | [m/s] |
| $u^+$ | Non-dimensional Velocity | [-] |
| $u^*$ | Friction Velocity | [m/s] |
| $u_i$ | Cartesian component of the velocity vector | [m/s] |
| $u_j$ | Cartesian component of the velocity | [m/s] |
| $u_\tau$ | Shear Velocity | [m/s] |
| $v_t$ | Eddy Viscosity | [m2/s] |
| $x_R$ | Recirculation Length | [m] |
| $y^+$ | Non-dimensional Veritical Distance | [m] |
| $\delta_{ij}$ | Kronecker Delta | [-] |
| $\mu_t$ | Turbulent Viscosity of Fluid | [kg/m·s] |
| $\sigma_k$ | Turbulent Prandtl Number for Kinetic Energy | [-] |
| $\nabla$ | Material Derivative Operator | [-] |
| D | Structure Height | [m] |
| g | Gravitational Acceleration | Kgm2s |
| Re | Reynolds Number | [-] |
| y | Vertical Distance Normal to the Wall | [m] |
| $\Omega$ | Control Volume | |
| $A$ | Projected Area | [m2] |
| $E$ | Logarithmic-Law Constant | [-] |
| $H$ | The Height of A Rectangular Computational Model | [m] |
| $L$ | The Length of A Rectangular Computational Model | [m] |
| $U$ | Mean Velocity | [m/s] |
| $V$ | Volume of Displace Water | [m3] |
| $k$ | Turbulence Kinetic Energy | [kg· (m2/s2)] |

| $l$ | Turbulence Length Scale | [m] |
| $p$ | Modified Pressure | [kg/m·s$^2$] |
| $t$ | Time | [s] |
| $u$ | Velocity in the x direction | [m/s] |
| $x$ | Horizontal Length | [m] |
| $\alpha$ | Angle of Steepness for Trapezoids | [°] |
| $\delta$ | Boundary Layer Thickness | [m] |
| $\varepsilon$ | Dissipation Rate | [m$^2$/s$^3$] |
| $\theta$ | Angle that the outer normal of dA on the structure makes with the positive flow direction | [°] |
| $\kappa$ | Von Karman's Constant | [-] |
| $\mu$ | Dynamic Viscosity | [kg/m·s] |
| $\rho$ | Fluid Density | [kg/m$^3$] |
| $\tau$ | Wall Shear Stress | [kg/m·s$^2$] |
| $\upsilon$ | Kinematic Viscosity | [m$^2$/s] |
| $\omega$ | Specific Dissipation Rate | [s$^{-1}$] |

# 1 Introduction

## 1.1 Background and motivation

In order to fulfill the rising global demand for oil and gas, the development of offshore industry switches to deep-water fields. Subsea equipment implemented in such fields are developed to cope with the strict requirements in terms of extreme hydrodynamic environments. In addition, these subsea structures are exposed to impact loads of the drop-objects as well as fishing activity loads. Hence, the protection covers are used to protect the submerged equipment from critical damages and even gas or oil leakage.

In recent time, Glass Reinforced Plastic (GRP) covers are becoming attractive alternatives opposed to metal covers due to its low-cost and high resistance against corrosion. Furthermore, GPR covers are significantly lighter than steel equivalents, thus it is easier to be transported and installed. However, there is a challenge for implementation of GPR covers on the seabed in terms of on-bottom stability problem due to its lightweight.

The hydrodynamic loads which are important to the stability of GRP covers include wave load and current load. In deep-water fields, the current and wave induced turbulent flow are generally at high Reynolds number, denoted as $Re$. Apart from Reynolds number, the flow characteristics around the structure are also influenced by the thickness of incident boundary layer and geometry of structures (Adams & Johnston 1988). Nowadays, these hydrodynamic problems are solved by either experiments or numerical simulations. For high Reynolds number flows, Computational Fluid Dynamics (CFD) method is preferable over experiments because it is complicated and expensive to create high Reynolds number flow conditions.

In this thesis, numerical simulations of flow around two-dimensional (2D) rectangular and trapezoidal structures are carried out using OpenFOAM, an open source CFD code. The turbulence is resolved by employing the $k - \omega\ SST$ RANS model. Hydrodynamic quantities, recirculation lengths, pressure and velocity distributions for different geometries of the structure are studied. Previous experimental data is used to validate the numerical results.

## 1.2 Literature review

Turbulent flow around wall-mounted obstacles is widely adopted as a representative model of various practical applications encountered in offshore industry. A typical example in offshore engineering is the subsea cover for pipelines mounted on the seabed. In deep-water fields, these structures are commonly subjected to high Reynolds number flow conditions. Kuijpers and Nielsen (2016) reported that the typical maximum velocity near the seabed is in order of $1$ m/s. The Reynolds number for a subsea structure of 1m height is in order of $1 \times 10^6$ (Fredsoe & Sumer 1997). Here the Reynolds number $Re = U_\infty D/v$, where $U_\infty$ is the free stream velocity, $D$ is the height of structure and $v$ is the kinematic viscosity of the fluid.

The characteristics of flow over the subsea structures have been extensively investigated through experimental and numerical simulations. The range of the Reynolds number from the earlier investigations covers the laminar flow regime at $0.5 < Re < 150$ (Tritton 1959) to the turbulent flow regime at large $Re$ in order of $1 \times 10^6$. Pattenden et al. (2007) simulated the flow past a surface-mounted circular cylinder using LES (Large Eddy Simulation) and DES (Detached Eddy Simulation) at a Reynolds number of $2.0 \times 10^5$. However, the poor resolution was detected using LES compared with DES. Akoz and Kirkgoz (2009) studied the turbulence flow at $R_e$ varying from $1.0 \times 10^3$ to $7.0 \times 10^3$ by several turbulence models such as the $k - \varepsilon$, $k - \omega$ and $k - \omega\ SST$ turbulence model. It was indicated that reasonable predictions were achieved using the $k - \omega$ and $k - \omega\ SST$ model. The results of both studies were validated with experimentally obtained data using particle image velocity (PIV).

Unlike the problem of flow around circular cylinders, the separate point of the flow is fixed at the leading corner of sharp-edged structures such as rectangular or trapezoidal cylinders; moreover, the vortex shedding behind the structures is suppressed by the wall. However, the shape of the structure is still strongly related to the surrounding flow fields. In the present study, CFD simulations are carried out to study the hydrodynamic quantities of flow around wall-mounted rectangular and trapezoidal cylinders with different slope angles.

Studies of flow around structures with geometries other than circular cylinder were also available in literatures. At low Reynolds number ($R_e = 4000$), the behaviors of flow over the tandem wall-mounted square cylinders are investigated by Dai et al. (Dai et al. 2017). The standard $k - \omega$ turbulence model were validated by comparing the horizontal velocity profiles with the experimental measurement reported by Crabb et al. (1977).

Tauqeer et al. (2017) investigated the turbulent boundary-layer flow around subsea covers with different geometries using the $k - \varepsilon$ turbulence model. The structures are subjected to sub-critical flow at Reynolds numbers of $3.41 \times 10^4 < R_e < 1.19 \times 10^5$. The nominal boundary layer thickness $\delta/D$ considered in study varies from 0.73 to 2.55. The flow past square structures at the same Reynolds number range were also studied by Arie et al. (1975) using experiments. For drag coefficient with $\delta/D \geq 1.7$, the numerical results reported by Tauqeer et al. (2017) matches well with the reported experimental data published by ARIE et al. (1975). The horizontal velocity profiles were further validated against the experimental measurements conducted by Liu et al. (2008).

Even though the problems of flow around the wall-mounted square cylinders have already been investigated by many researchers, further studies are still essential to provide more realistic simulation. In deep-water fields, the subsea structures are subjected to high Reynolds number boundary layer flows. In the present study, the numerical solution of flow over a square cylinder using the $k - \omega \, SST$ model has been compared with Liu et al.(2008). Furthermore, the hydrodynamic quantities of rectangular and trapezoidal structures with a variety slope angles are investigated. The length of the bottom is kept the same to ensure that projection area in lift force direction is consistent.

## 1.3  Outline

**Chapter 1** gives an introduction of the background for the topic and motivation for the thesis

**Chapter 2** provides the hydrodynamic theories related to characteristics of turbulent flow over wall-mounted structures under turbulent flow. This includes theory on flow over bluff and streamlined bodies, an introduction to turbulence and fundamental laws for governing equations.

**Chapter 3** introduces the concept of Computational Fluid Dynamics (CFD) and the software used in the present work. Reynolds-averaged Navier-Stokes (RANS) equations and $k-\omega$ SST turbulence model are explained in this chapter.

**Chapter 4** describes the CFD model and gives an explanation for boundary conditions applied throughout the simulation.

**Chapter 5** presents and discusses the results of simulations, including the convergence and the validation study. In addition, the contour plots of the velocity field, pressure field and streamlines plots are shown and discussed in detail.

**Chapter 6** draws the conclusions of this work.

**Chapter 7** offers the possible directions for further research.

# 2 Theory

This chapter gives an introduction to the basic theories related to the simulation of the flow over wall-mounted structures, including the knowledge of flow physics, turbulent boundary layer as well as applications of the fundamental governing equations.

## 2.1 Flow Characteristics

The flow over wall-mounted structures is different from the flow around a suspended structure, e.g. a free-spanning pipeline. For the latter situation, the vortex shedding occurs in the downstream after the flow detaches from both the top and bottom of the structure. As shown in Figure 2.1, the flow separation leads to the formation of unstable vortex back the cylinder. At high Reynolds number flow conditions, the vortices shed from either side in an alternating way. In contrast, for a wall-mounted structure such as a GRP subsea cover, a large wake will be formed in the back of the structure instead of vortex shedding, which is suppressed by the wall.

Figure 2.1: Vortex formation behind a circular cylinder (Sunden 2011).

The forces exerted on wall-mounted structures are characterized by lift force acting normal to the body surface and drag force which is acting along the tangential direction of body surface. The drag forces are generally categorized into friction drag and pressure drag. Friction drag is in principle generated in the boundary layer due to the viscosity between the fluid and the surface of the immersed object. The pressure drag is formed by the difference in pressure between the front and back of the object.

According to research conducted by Adams and Johnston (1988), the characteristics of the boundary layer flow depends upon the geometry of the structure, Reynolds number as well as the boundary layer thickness. The structures can be categorized according to their physical shapes, as being either *streamlined* or *bluff*. *A streamlined body* refers to a body shape which is better aligned with the flow pattern, as shown in Figure 2.2 (a). A property of such bodies is

that the viscous friction dominates the drag force. *A bluff body* refers to a body with a large separated wake region of disrupted flow in the downstream of the body, as shown in Figure 2.2(b).



(a)



(b)
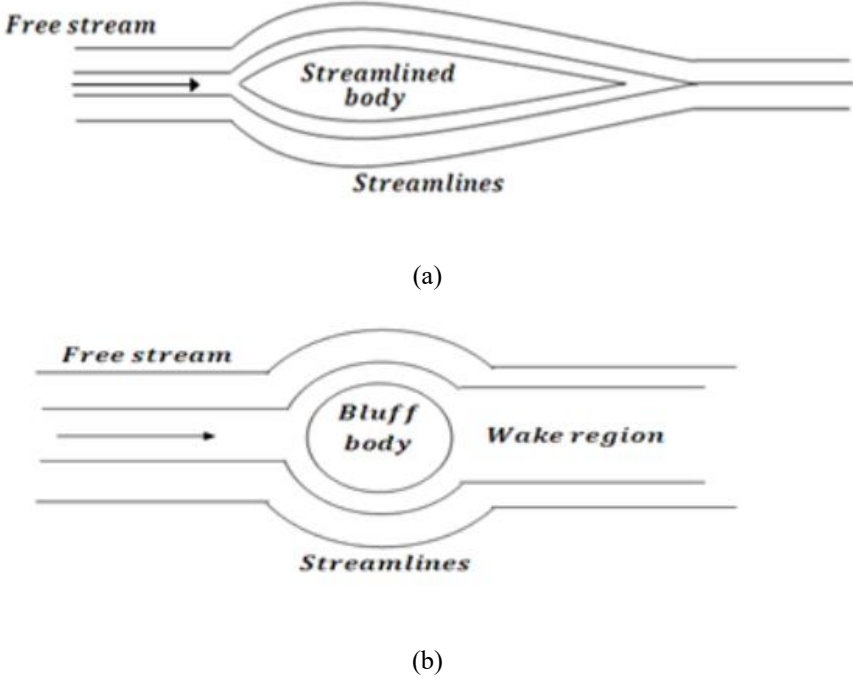
Figure 2.2: Flow patterns over streamlined body and bluff body.

## 2.2 Turbulence

A fluid flow can be classified as either turbulent or laminar. This section gives a brief relevant theoretical description to the turbulence.

### 2.2.1 Laminar Flow and Turbulent Flow

Reynolds number is an essential dimensionless quantity in fluid mechanics to characterize the flow behavior in any type of flow situations. Besides, the Reynolds number is also a key factor used to estimate whether the flow is laminar, transient or turbulent. By definition, it indicates the ratio between the inertial force and the viscous force as expressed in the following equation (Cencel & Cimbala 2006):

$$Re = \frac{Ineritial\ force}{Viscous\ force} = \frac{U_\infty D}{\upsilon} \qquad (2.1)$$

where $U_\infty$ is the characteristic free stream velocity, $D$ is a characteristic length of the geometry, $\upsilon$ is kinematic viscosity of the fluid.

*Laminar flows* occur at low velocities or low Reynolds numbers, that is when the viscous force is dominant over the inertial force, in accordance with Eq.(2.1). In such situations the fluid particles are kept flowing orderly in a straight line without lateral interruptions. Conversely, *turbulent flows* occur if the inertial forces dominate over the viscous ones. Turbulent flows are characterized by irregularity, diffusivity, rotationality and dissipation, observed commonly in everyday phenomena like smoke rising from a cigarette or air in high velocities. A comparison between laminar and turbulent flow, as well as the transition between them, are shown in Figure 2.3:
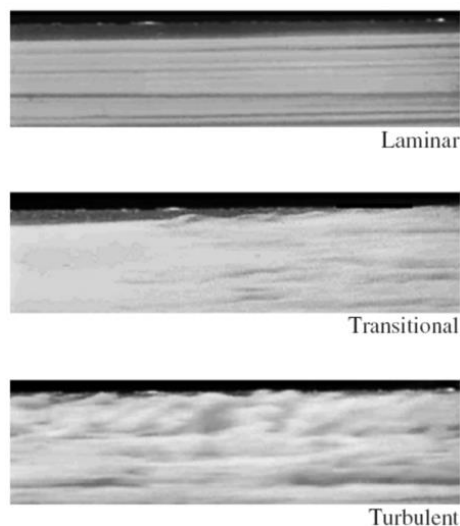


Figure 2.3: Laminar, transitional and turbulent flows over a flat plate (Cencel & Cimbala 2006).

The critical value of the Reynolds number is the limit where flow switches over from being laminar into being turbulent. For a smooth cylindrical structure immersed in a flow at Reynolds numbers ranging within the interval of (200, 300), a transition to turbulence takes place according to Fredsoe and Sumer (1997), as displayed in Figure 2.4:
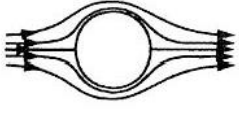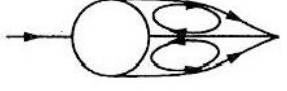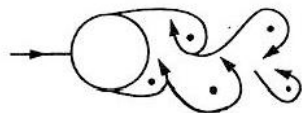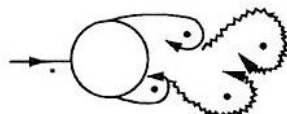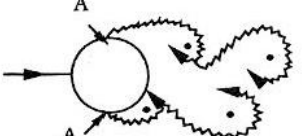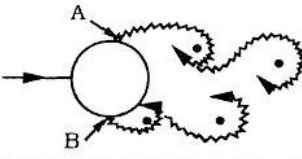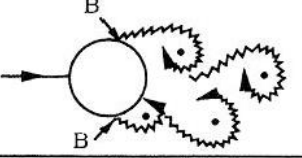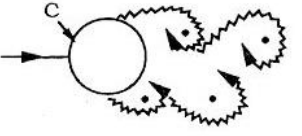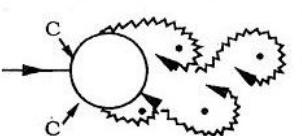
| | | | |
|---|---|---|---|
| a) | | No separation. Creeping flow | Re < 5 |
| b) | | A fixed pair of symmetric vortices | 5 < Re < 40 |
| c) | | Laminar vortex street | 40 < Re < 200 |
| d) | | Transition to turbulence in the wake | 200 < Re < 300 |
| e) | A ... A | Wake completely turbulent. A:Laminar boundary layer separation | $300 < Re < 3{\times}10^5$ Subcritical |
| f) | A ... B | A:Laminar boundary layer separation B:Turbulent boundary layer separation;but boundary layer laminar | $3 \times 10^5 < Re < 3.5 \times 10^5$ Critical (Lower transition) |
| g) | B ... B | B: Turbulent boundary layer separation;the boundary layer partly laminar partly turbulent | $3.5 \times 10^5 < Re < 1.5 \times 10^6$ Supercritical |
| h) | C | C: Boundary layer completely turbulent at one side | $1.5{\times}10^6 < Re < 4{\times}10^6$ Upper transition |
| i) | C ... C | C: Boundary layer completely turbulent at two sides | $4{\times}10^6 < Re$ Transcritical |

Figure 2.4: Flow regimes around a cylinder in steady current (Fredsoe & Sumer 1997).

In this thesis, the simulations are performed at the Reynolds numbers ranging within $[0.5 \times 10^6, 2 \times 10^6]$, indicating that the investigated flow is a fully developed turbulent boundary layer flow.

Turbulent flows have chaotic variations of velocity, pressure and other time-dependent properties. Fully developed turbulent flows are explored in this thesis. The fluctuation of velocity with time at a specified measurement position in a turbulence flow is exhibited in Figure 2.5.
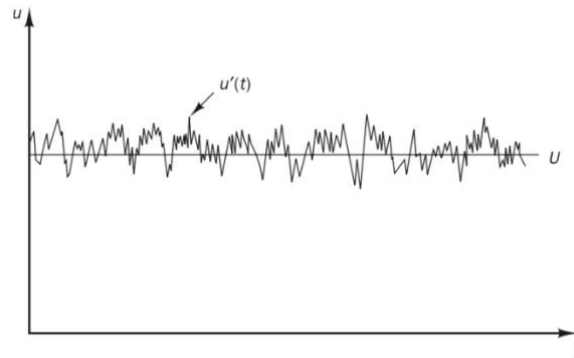


Figure 2.5: A specified position velocity measurement in a turbulent flow (Cencel & Cimbala 2006).

The velocity of a turbulent flow $u(t)$ can be decomposed into a mean velocity $U$ and a fluctuating velocity $u'(t)$, as expressed in Eq. (2.2):

$$u(t) = U + u'(t) \qquad (2.2)$$

For a steady state flow solved by RANS method, the mean flow component of the velocity is invariant with respect to time, and the time averaging values of fluctuation component, $u'(t)$, should be zero as further explained in Chapter 3.2.1.

There are turbulent eddies with a wide range of spatial length scales in turbulent flow as illustrated in Figure 2.6. The large eddies are dominated by inertial forces rather than viscous forces. The size of large eddies is in the same order of the characteristic length of geometry, $D$, and the velocity of the large eddies is in the same order as the free stream velocity $U_\infty$. The kinetic energy is dissipated into heat while the large eddies transform to small eddies according to the principle of energy cascade. (Versteeg & Malalasekera 1995).
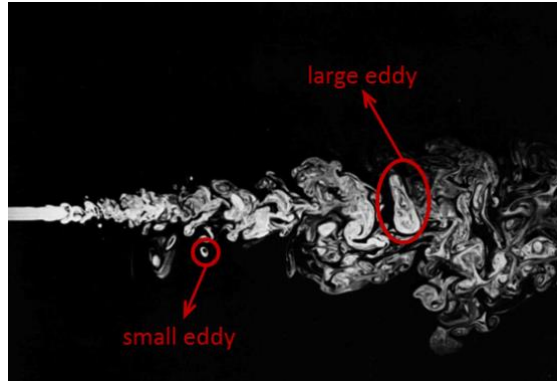
Figure 2.6: Turbulent flow visualization (Akan 2012).

## 2.2.2 Turbulent Boundary Layer

At high Reynolds numbers, the boundary layer of a flow is a relatively thin layer adjacent to the wall where the viscous effects predominate. As demonstrated in Figure 2.7, the flow of a fluid over a flat plate starts from a laminar flow and eventually develops into the turbulent flow. The flow velocity on the surface of the plate is zero as a result of the no-slip condition and increases away from the wall to the free-stream velocity.
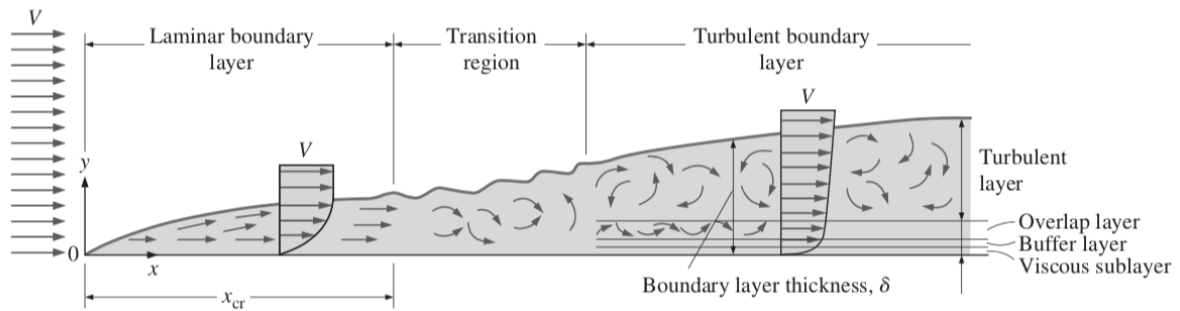


Figure 2.7: The development of the boundary layer for flow over a flat plate.(Cencel & Cimbala 2006).

The turbulent boundary layer is divided into four regions with respect to the distance from the wall. The layers in question, from bottom to top, are the viscous sublayer, the buffer layer, the overlap layer and the turbulent layer. In these four different layers, the effect of viscosity decreases progressively while the effect of turbulence exhibits the opposite tendency. Each layer has its own properties that can be expressed by two non-dimensional parameters. Namely, the non-dimensional shear velocity, $u^+$, which is defined as the ration between velocity and shear stress velocity and the non-dimensional vertical distance from the bottom wall $y^+$, which are

expressed as:

$$u^+ = \frac{U}{u_\tau} \tag{2.3}$$

where $u$ is the velocity, $u_\tau$ is the shear velocity and $u_\tau = \sqrt{\frac{\tau}{\rho}}$, $\tau$ is the wall shear stress.

$$y^+ = \frac{yu_\tau}{v} \tag{2.4}$$

where $y$ is the vertical distance from the wall, $v$ is the kinematic viscosity.

As shown in Figure 2.7, the first layer closet to the no-slip boundary is known as the viscous sublayer. It is worth mentioning that the thickness of the viscous sublayer accounts for 1% of the total boundary layer thickness, i.e. $y^+ \leq 5$ (Cencel & Cimbala 2006). The viscous force dominates throughout this thin layer. This means the viscous sublayer is laminar, independently from whether or not the whole boundary layer is regarded as turbulent. The ratio between the velocity $u^+$ and $y^+$ is approximately equal to 1. This linear relationship is expressed in dimensionless form as Eq. (2.5):

$$\frac{u}{u_\tau} = \frac{yu_\tau}{v} \tag{2.5}$$

According to Eq. (2.3) and Eq. (2.4), the non-dimensional form of the law of the wall within viscous sublayer can be obtained:

$$u^+ = y^+ \tag{2.6}$$

11

Following the viscous sublayer is the buffer layer, in which the turbulent effects turns to be crucial; however, the viscous effect still dominates. In this transitional region between full turbulent layer and laminar sublayer, small-scaled eddies are produced from large eddies. Consequently, the properties of the flow are challenged to be accurately predicted. The critical variation occurs nearly at $y^+ = 11$, where the interception of the linear solution and logarithmic solution exist. This suggests the linear approximation before 11 wall units is more accurate, while the logarithmic approximation is better than linear approximation after 11 wall units (Absi 2009).

The region outside of the buffer layer is the overlap layer, also known as the log-law layer. In the log-law layer, between 30 wall units to 500 wall units, the dominated turbulent shear stress varies gradually with $y^+$. The velocity profile is computed by the log-law as below:

$$u^+ = \frac{1}{\kappa} \ln(E y^+) \tag{2.7}$$

where von Karman's constant $\kappa$ is approximately equal to 0.4 and the log-law constant $E$ is approximately equal to 9.8 in OpenFOAM for smooth walls. Velocity profiles in different layers of the turbulent boundary layer is shown in Figure 2.8.
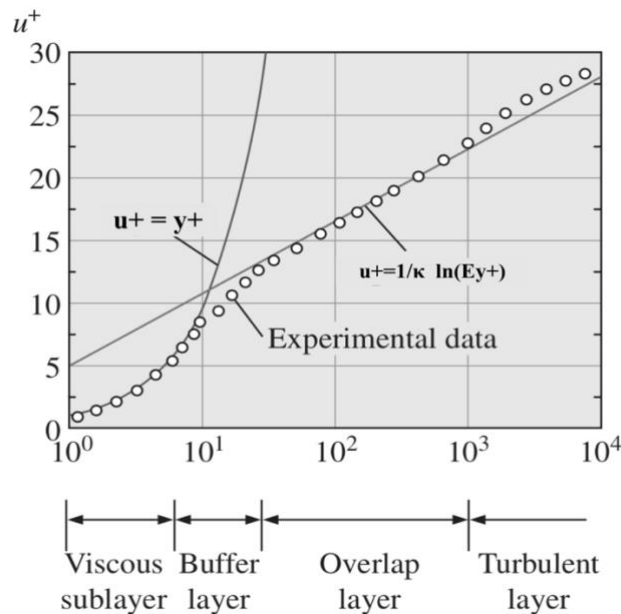


Figure 2.8: Comparison of the Law of Wall and the Logarithmic Law Velocity Profiles (Cencel & Cimbala 2006).

There is also an inertia-dominated outer turbulent layer far from the wall. In this region, the inertial effect and eddy motion are significant while the viscous effect is negligible. An acceptable approximation for the outer turbulent layer can be obtained by assuming the following logarithmic form:

$$\frac{U_\infty - U}{u_\tau} = -\frac{1}{\kappa}\ln\left(\frac{y}{\delta}\right) + C \tag{2.8}$$

where $C$ is a constant. This logarithmic form is called the velocity defect law or the law of the wake. (Versteeg & Malalasekera 1995).

## 2.3 Hydrodynamic Coefficients

The net force of the pressure force, acting normal to the surface and shear forces, acting tangential to the surface, can describe the drag and lift force as:

$$F_D = \int_A dF_D = \int_A (-p\cos(\theta_n) + \tau_w\sin(\theta_n))dA \tag{2.9}$$

$$F_L = \int_A dF_D = \int_A (-p\cos(\theta_n) - \tau_w\sin(\theta_n))dA \tag{2.10}$$

where $dF_D$ is the differential drag force, $dF_L$ is the differential lift force, $dA$ is the differential cross-sectional area, $\theta_n$ is the angle which the force works normal to $dA$ (Cencel & Cimbala 2006).

The drag and lift force acting on immersed wall-mounted structures are dependent on several factors including the density of fluid $\rho$, the shape of structures and the velocity of incoming flow. In order to obtain the drag and lift forces on different structures under different flow conditions, it is more appropriate to use the non-dimensional drag and lift coefficients, which are defined as follows:

$$C_d = \frac{F_D}{\frac{1}{2}\rho U_\infty^2 A} \tag{2.11}$$

$$C_l = \frac{F_L}{\frac{1}{2}\rho U_\infty^2 A}$$ (2.12)

where $A$ indicates the front projected area of the body (Cencel & Cimbala 2006).

## 2.4 Governing Equations

The fluid flow investigated throughout the present study is incompressible and isothermal. The motion of an incompressible flow in the physical domain is governed by various properties such as velocity, pressure, density, viscosity and so on. The Navier-Stokes system equations along with the continuity equation are broadly used to examine the velocity vector field of the flow. The fluid is regarded as a continuum, and the governing equations are derived from the statements of the conservation laws of fluid motion (Cencel & Cimbala 2006):

1. The mass of a fluid is conserved.
2. The rate of change of momentum equals the sum of the forces on a fluid particle (Newton's second law).
3. The rate of change of energy is equal to the sum of the rate of heat addition to and the rate of work done on a fluid particle (Versteeg & Malalasekera 1995).

## 2.5 Conservation of Mass and Momentum

The Mass Conservation Law states that the total mass in a system with constant control volume will not change over time. This can be illustrated as below by applying the continuity equation of density:

$$\frac{\partial \rho}{\partial t} + \nabla \cdot (\rho \vec{V}) = 0$$ (2.13)

For an incompressible fluid, the density is constant over time. Therefore, the equation above can be simplified by setting the derivative of density equal to zero and dividing through by a constant $\rho$:

$$\nabla \cdot \vec{V} = 0$$ (2.14)

The Navier-Stokes equations are derived from Newton's second law, where dictates that the total of body forces and surface forces applied on the control volume equal to the rate of change of momentum. This can be expressed by the following equation:

$$\frac{\partial \vec{V}}{\partial t} + (\vec{V} \cdot \nabla)\vec{V} = -\frac{1}{\rho}\nabla p + v\nabla^2 \vec{V} \tag{2.15}$$

where $\vec{V}$ is the velocity vector of the flow, and $p$ is the pressure. The gravitational term from the Navier-Stokes equation is eliminated since the free-surface effect is not considered in this thesis.

The governing equations for the 2D simulation in this study can be written as:

$$\frac{\partial u_i}{\partial x_i} = 0 \tag{2.16}$$

$$\frac{\partial u_i}{\partial t} + u_j \frac{\partial u_i}{\partial x_j} = -\frac{1}{\rho}\frac{\partial P}{\partial x_i} + v\frac{\partial^2 u_i}{\partial x_j^2} \tag{2.17}$$

where, i,j = 1,2 denotes the directions in the two-dimensional Cartesian coordinates system. $u_i$ is representing the velocity in these directions.

# 3  Computational Fluid Dynamics

Computational Fluid Dynamics (CFD) refers to a branch of numerical techniques used to simulate the fluid dynamic phenomena. In the 1960s, the technology was first incorporated into the design and manufacture of aircraft and jet engines. Due to the advantages in reducing costs and its sufficient accuracy, CFD has been continuously developed to replace the experiment-based approaches and become increasingly significant in a wide range of academic as well as industrial applications.

The fundamental basis of solving most CFD problems is the discretization of the Navier-Stokes equations. Generally, all CFD algorithms contain three main parts as follows:

· **Pre-processor**
· **Solver**
· **Post-processor**

This chapter will further introduce the open source code as well as discretization method adopted in the present study.

## 3.1  OpenFOAM

Open Source Field Operation and Manipulation (OpenFOAM), or OpenFOAM for short, is an open source CFD toolbox with a large range of applications, including but not limited to conduct numerical modelling of solid and fluid mechanic problems.

OpenFOAM is a collection of C++ libraries that used to create executables including solvers and utilities. OpenFOAM offers a variety of standard solvers for solving either incompressible or compressible flows at steady or unsteady state; utilities are tools to perform simple pre- and post-processing tasks, mainly involving data manipulation and algebraic calculations. The overall structure of OpenFOAM is presented in the figure below:
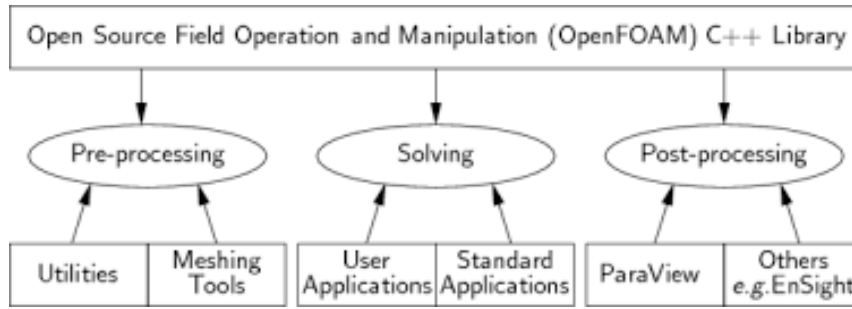
Figure 3.1: The structure of OpenFOAM (Pegonen 2012).

OpenFOAM simulation case is built up by files in a folder structure, and the necessary files required to run an application are included in three subdirectories:

**Constant directory:**
Contains the physical properties of the fluid under consideration, as well as a specified mesh.

**System directory:**
Contains the user-defined parameters involved in the simulation procedure, as well as the discretization schemes used to run case in parallel.

**'Time' directories:**
The initial values and boundary conditions named after each property, e.g. U for Velocity, are included in the 0 folder.

The general structure of an OpenFOAM directory is illustrated in Figure 3.2:
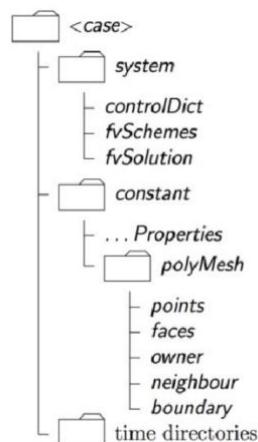


Figure 3.2: The general structure of an OpenFOAM directory.

### 3.1.1 Meshing and Preprocessing

The partial differential equations (PDE) governing the fluid flow are usually not suitable to obtain analytical solutions for complicated cases. Therefore, in order to analyze any fluid flow, a preprocessing step for CFD simulation is required to discretize the problem domain into finite continuum subdomains. The partitioned domain is referred to as a *mesh*, or *grid*. In other words, mesh can be defined as a set of connected cells distributed over the problem domain for a numerical solution of the PDE. The overview of the fluid in the entire domain can be obtained by integrating the solutions inside the finite subdomains. The continuity of the mesh and grid gradation interferes with the accuracy of the numerical solution. In addition, mesh spacing near the wall need to be carefully controlled to capture the gradient information of velocity and pressure.

Although OpenFOAM has a variety of self-built in mesh utilities, the OpenFOAM supported mesh generator GMSH has been used in this study, due to its advanced visualization capabilities and straightforward interaction between the graphic input mode and the scripting language.

### 3.1.2 Solving

OpenFOAM solves the Navier-Stokes equations over a space using the finite volume methods (FVM). In order to solve the Navier-Stokes equation one must discretize the partial differential equations. There are vast discretization schemes available in OpenFOAM. For all cases, the *fvschemes* directory contains the information related to discretization schemes for terms appearing in the relevant governing equations. Typically, the necessary numerical schemes required in *fvschemes* can be divided into following categories*:*

·  **Time schemes**:

   Time schemes refer to the first order derivatives of time, which is specified in the *ddtSchemes* sub-directory

·  **Gradient schemes:**

   Gradient schemes refer to the gradient term discretization, which is specified in the

*gradSchemes* sub-directory. The gradient schemes used in present simulation is Gauss linear, and a *cellLimited* gradient limiter is applied to ensure the stability during computation of the gradients.

· **Divergence schemes:**

The divergence schemes concerning the convective term are contained in *divSchemes* sub-directory. The divergence schemes adopted in discretization of the convective term in this study is bounded Gauss linear upwind, which is bounded and stable with first order accuracy.

· **Laplacian schemes**

The Laplacian schemes are assigned in *laplacianSchemes* sub-directory and is relevant for discretization of Laplacian terms. Laplacian schemes available in present work is Gauss linear limited corrected.

· **Interpolation schemes**

By interpolation schemes located in *interpolationSchemes* sub-directory, the concerning values are interpolated from cell centers to face centers.

· **Surface normal gradient schemes:**

The discretization of surface normal gradient is evaluated at the faces. The surface normal gradient term is contained in *snGradSchemes* sub-directory.

## 3.1.3  Courant number

The governing equations employed in CFD simulation are normally complex non-linear partial differential equations. Numerical errors may lead to significant deviations from the exact solution. Thus, it is necessary to take stability criteria into account in order to avoid uncertainties regarding the simulations. The Courant number, also known as the CFL-number, is a constraint applied to curtail the mesh size or time-step size in order to maintain the stability of simulation. CFL number is defined as:

$$C = U\frac{\Delta t}{\Delta x} \leq C_{max} \qquad\qquad (3.1)$$

where $U$ is the fluid velocity passing through a cell, $\Delta t$ is the time step, $\Delta x$ is the cell length in $x$ direction. The Courant number varies with respect different discretization methods. In general, explicit schemes used for solving Navier-Stokes equations curtails the Courant number to be less than 1.

### 3.1.4  Post-processing

There are a multitude of post-processing utilities, such as Ensight, Tecplot or Paraview, available for dealing with the output data from simulations. In this study, the open source tool Paraview is adopted to draw the desired data for the further analysis carried out by Matlab. In addition, Tecplot360 is also used to visualize results, including the streamline, contour plots of velocity field and pressure field.

## 3.2  Turbulence Modelling

The Reynolds-Average Navier-Stokes (RANS) model is used to solve the flow field instead of the Large Eddy Simulation (LES) or Direct Numerical Simulation (DNS) due to the low computational cost and reasonable engineering accuracy. More details about RANS equations and the turbulence model applied in this study are presented in this section.

### 3.2.1  Reynolds-Averaged Navier-Stokes

The Reynolds -averaged Navier-Stokes (RANS) equations are time averaged equations that are primly used for describing the motion of turbulent flow. According to the Reynolds decomposition, the instantaneous flow variable can be decomposed into a time-averaged term and a time-dependent fluctuation term. The flow property such as velocity, can be decomposed as:

$$u(t) = u'(t) + U \qquad\qquad (3.2)$$

where $U$ is the time-averaged component of velocity, and $u'(t)$ is the fluctuating component of velocity. The mean value of the fluctuating component over a time interval should be equal to zero for a steady state flow:

$$\bar{u}' = \frac{1}{\Delta t} \int_{0}^{\Delta t} u'(t)\, dt \equiv 0 \tag{3.3}$$

By substituting the Eq.(3.2) into Navier-Stokes equations given in Eq. (2.17), the RANS equations can be obtained as:

$$\frac{\partial u_i}{\partial t} + u_j \frac{\partial u_i}{\partial x_j} = -\frac{1}{\rho} \frac{\partial P}{\partial x_i} + v \frac{\partial^2 u_i}{\partial x_j{}^2} - \frac{\partial \overline{u_i' u_j'}}{\partial x_j} \tag{3.4}$$

As explained above, the time-dependent term, $\frac{\partial u_i}{\partial t}$, is equal to zero for steady RANS. Due to the nonlinearity of the Navier-Stokes equations, this transformation introduces a set of unknowns called the *Reynolds stresses*, denoted by $\overline{u_i' u_j'}$, which is a function accounting for turbulent fluctuations in fluid momentum. The Boussinesq hypothesis is employed to model the Reynolds stresses term as an increase effect due to the eddy viscosity. This can be expressed by the formula below:

$$-\overline{u_i' u_j'} = v_t \left( \frac{\partial u_i}{\partial X_j} + \frac{\partial u_j}{\partial X_i} \right) - \frac{2}{3} k \delta_{ij} \tag{3.5}$$

where $k$ is the turbulence kinetic energy; $\delta_{ij}$ is the Kronecker delta and $v_t$ is the eddy viscosity. Kronecker delta is defined as:

$$\delta_{ij} = \begin{cases} 0, & if \ \ i \neq j \\ 1, & if \ \ i = j \end{cases} \tag{3.6}$$

In order to obtain equations containing only the mean velocity and pressure, the turbulence model is required to produce a closed system of solvable equations. Closure of Reynolds stress is computed by utilizing the $k - \omega\ SST$ turbulence model in this study.

### 3.2.2 $k - \omega \, SST$ Turbulence Model

There are various Reynolds stress models for solving the turbulence closure problems. Among those, two RANS based turbulence models, namely the $k - \varepsilon$ model and the $k - \omega$ model, are commonly used. The $k - \omega \, SST$ turbulence model is a hybrid model which is a combination of the two aforementioned models. In the $k - \omega \, SST$ turbulence model, the standard $k-\varepsilon$ model is employed in the outer part of the boundary layer as well as in the free stream region, while the Wilcox $k-\omega$ model is activated by the blending function.

For steady RANS the transport equation of kinetic energy in the $k - \omega \, SST$ model is identical to that of the standard $k - \omega$ model, which can be computed as:

$$\frac{D(\rho k)}{Dt} = \widetilde{P_k} - \beta^* \rho \omega k + \frac{\partial}{\partial x_j} \left[ (\mu + \sigma_k \mu_t) \frac{\partial k}{\partial x_j} \right] \tag{3.7}$$

where $\omega$ indicates the specific dissipation rate and $\widetilde{P_k}$ is used to prevent the build-up of turbulence in the stagnation regions and can be expressed as:

$$\widetilde{P_k} = min \left[ \mu_t \frac{\partial u_i}{\partial x_j} \left( \frac{\partial u_i}{\partial x_j} + \frac{\partial u_j}{\partial x_i} \right), 10\beta^* \rho \omega k \right] \tag{3.8}$$

However, the production of $\omega$ , is slightly different from that of the standard $k - \omega$ model with including the cross-diffusion term from the wall:

$$\frac{D(\rho \omega)}{Dt} = \alpha \rho S^2 - \beta \rho \omega^2 + \frac{\partial}{\partial x_j} \left[ (\mu + \sigma_\omega \mu_t) \frac{\partial \omega}{\partial x_j} \right] + 2(1 - F_1)\rho \sigma_{\omega 2} \frac{\partial k}{\partial x_j} \frac{\partial \omega}{\partial x_j} \tag{3.9}$$

The Cross-diffusion term is given by:

$$CD_{k\omega} = max \left( 2\rho \sigma_\omega \frac{1}{\omega} \frac{\partial k}{\partial x_j} \frac{\partial \omega}{\partial x_j}, 10^{-10} \right) \tag{3.10}$$

Moreover, a blending function $F_1$ is employed to switch the $k - \omega \, SST$ model between the $k - \omega$ and $k - \varepsilon$ by changing $F_1$ from 1 at the near-wall region, and to 0 in the free stream region. The value of the model constants is computed by the following expression:

$$\phi = F_1\phi_1 + (1 - F_1)\phi_2 \tag{3.11}$$

where $\phi_1$ denotes the corresponding constant in $k - \omega$ model and $\phi_2$ denotes the constant in $k - \varepsilon$ model, and blending function $F_1$ is defined as:

$$F_1 = \tanh(arg_1^4) \tag{3.12}$$

In addition, the $k - \omega\ SST$ model curtails the shear stress by implementing the blending function $F_2$; to alter from eddy viscosity model to the Johnson King model in case the shear stress is too large. Turbulence viscosity is given as:

$$v_t = \frac{a_1 k}{max(a_1\omega, SF_2)} \tag{3.13}$$

where $S$ is the invariant measure of the strain rate and $F_2$ is given by:

$$F_2 = \tanh\left\{\left[\max\left(2\frac{\sqrt{k}}{0.09\omega y}, \frac{500v}{y^2\omega}\right)\right]^2\right\} \tag{3.14}$$

he following constants have been adopted in the $SST$ model: $\beta^* = 0.09$, $\alpha_1 = 0.5532$, $\alpha_2 = 0.4403$, $\beta_1 = 0.075$, $\beta_2 = 0.0828$, $\sigma_{k1} = 0.85$, $\sigma_{k2} = 1.0$, $\sigma_{\omega1} = 0.5$, $\sigma_{\omega2} = 0.85616$

## 3.3  Finite Volume Method

The Finite Volume Method is a numerical method used to discretize the governing equations over differential volumes in the form of algebraic equations over finite volumes (Moukalled et al. 2016). The method was first introduced in the simulation of transonic flow through two-dimensional gas turbine cascades by McDonald (McDonald 1971). The Finite Volume Method mainly consists of 3 steps:

Step 1: Grid Generation
Step 2: Discretization
Step 3: Solution of equations

The first step in the FVM routine is to divide the geometry domain into a number of arbitrary control volume. In OpenFOAM, the variable of interest is positioned at the center of the control volume. The governing equations on each control volume are integrated to obtain the discretized equation at the computational node. Hence, the volume integrals can be converted into a surface integral at the cell boundaries using divergence theorem. The integral form of the of the governing equations on the control volume $\Omega$, enclosed by surface S can be expressed by:

$$\oint_s \vec{V} \cdot \vec{n}\, dS = 0 \tag{3.15}$$

$$\frac{\partial}{\partial t} \int_\Omega \vec{V}\, d\Omega + \vec{V} \oint_s V_n\, dS = \oint_s (\vec{\sigma} \cdot \vec{n})\, dS \tag{3.16}$$

Following the integral equations are converted to linear system of algebraic equations comes the final step of the CFD-process, and equations are solved in an iterative method. Various solvers are built in OpenFOAM for specific situations. The basic solver SimpleFoam has been used in this study.

## 3.4 SimpleFoam

SimpleFoam is the OpenFOAM solver that incorporates the SIMPLE algorithm, which stands for Semi-Implicit Method for Pressure Linked Equations. The SIMPLE algorithm was first introduced by Patankar and Spalding (1983). The SIMPLE algorithm has been extensively used to solve the pressure-velocity coupling problem occurring in steady-state simulation of the impressible, turbulent flow. The SIMPLE algorithm is essentially an iterative predicting- and correcting procedure as shown in Figure 3.3:
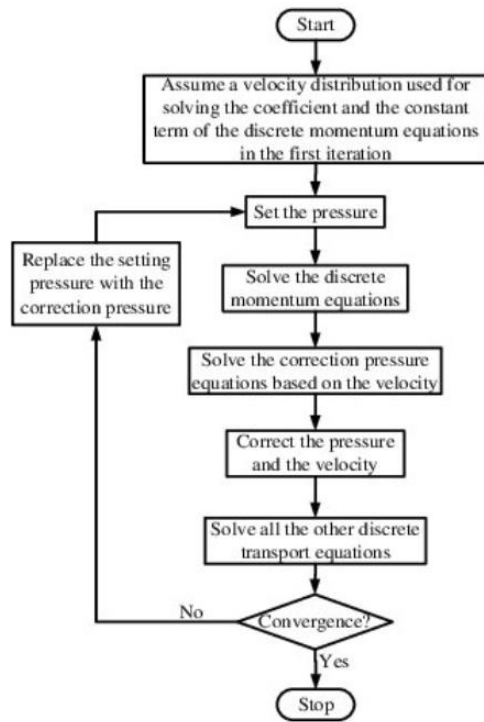
Figure 3.3: Calculation process of simple algorithm (Yu et al. 2019).

# 4 Computational Model

The flow over the wall-mounted subsea covers with different geometries have been modeled in OpenFOAM. The details of the computational model and boundary conditions are described in this chapter.

## 4.1 Geometry of Model

In the pre-processing stage, any CFD simulation case starts with the construction of the flow domain around or in the structure which is of interest. A proper selection of the domain size will make a difference in the computational efficiency and accuracy of results. In the case of the target object immersed in external flows, a sufficiently large computational domain is required to prevent the boundary conditions free from the recirculation zones. However, a large size domain can also lead to a longer simulation process compared with the case of a small domain. In addition to the geometry of the target structure, the Reynolds numbers of flow and the past experimental data are also considered to select the computational domain.

The domain configurations adopted in this study are presented in Figure 4.1 and Figure 4.2 :
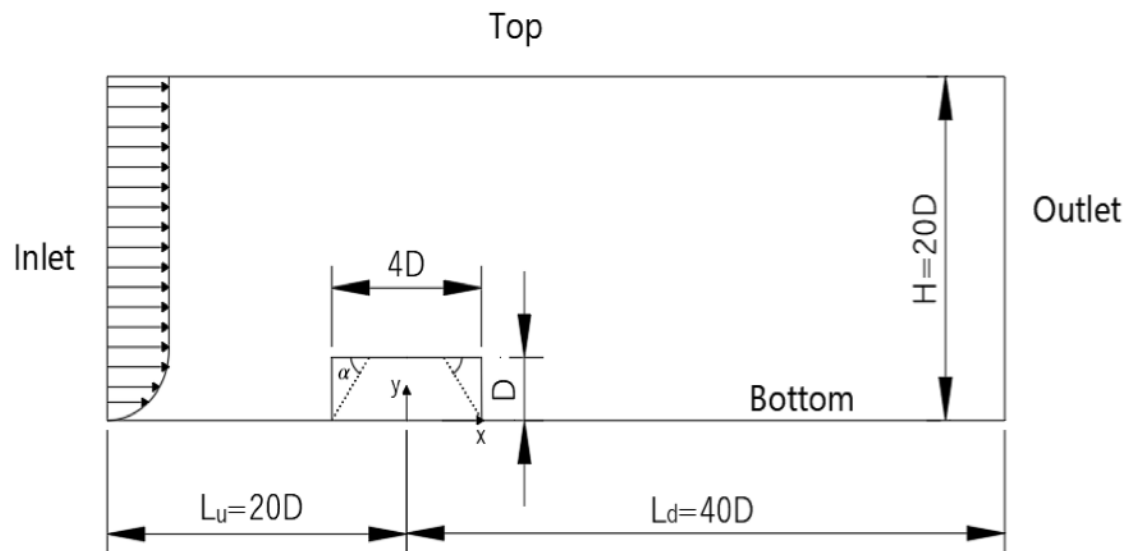


Figure 4.1: Computational domain and boundary conditions for the trapezoid case.
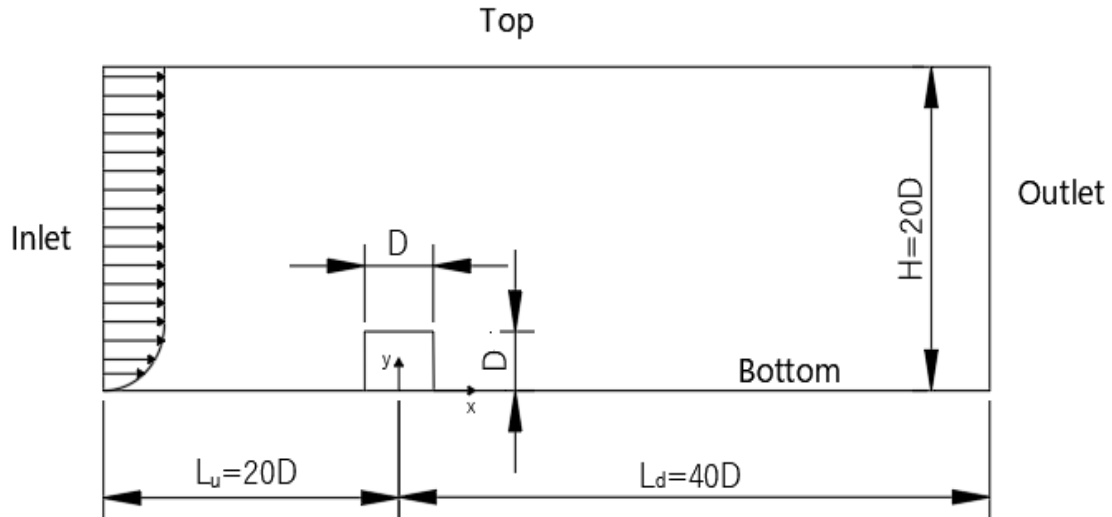
Figure 4.2: Computational domain and boundary conditions for the square case.

The computational domain is a rectangle of size $L$ by $H$; the dimensionless unit of scale introduced in the model is $D$. Both the bottom and height are restricted to the fixed length of $4D$ and $D$, respectively. The center of the bottom edge of the studied object is assigned as the origin of the coordinates system.

High Reynolds number flows require far-field distances in the upper portion of the domain. According to the previous study conducted by Ong et al. (2010) , which is about the numerical study of flow around circular cylinder close to a flat seabed at the similar Reynolds number condition to present case, the flow inlet boundary is set to $20D$ upstream from the center of the structure and the outlet is set to $40D$ downstream from the center of the structure. The distances from the inlet and outlet boundary to the center of object are assigned to be $(L_u, L_d) =$ $(20D,40D)$. The whole computational domain is sufficient to eliminate the far-field effect on flow performance around the structure while the boundary conditions have been applied at the exterior of the flow domain.

## 4.2   Boundary Conditions

*Boundary conditions* refer to a series of constrains concerning the partial differential equations imposed at boundaries. The appropriate initial values and boundary conditions are significant for a successful CFD simulation. It is worth noting that a small alteration of the imposed boundary condition will lead to a variation of the prediction at any point of the domain in the solving process.(Kuijpers & Nielsen 2016)

In fluid mechanics, Dirichlet boundary conditions, Neumann boundary conditions and Robin boundary conditions are three well-known types boundary conditions.

**Dirichlet boundary conditions:**

Specify the exact value of the dependent variable that needs to take on along the boundary of the domain (Cheng & Cheng 2005). In computational fluid mechanics, the classical Dirichlet boundary condition concludes the value of velocity and/or pressure.

**Neumann boundary conditions:**

Prescribe the value in which the derivative of a solution is applied within the boundary of domain (Cheng & Cheng 2005). Normally, the constraints on the gradient of velocity or pressure are referred as the application of Neuman boundary condition in CFD analysis.

**Robin boundary conditions:**

Robin boundary condition is a linear combination of the Dirichlet and Neumann condition.

The initial values and boundary conditions related to the RANS equations are required to be specified into boundaries at patches of different types. These are further presented in the following subsections.

## 4.2.1 Inlet

The inlet velocity is a logarithmic profile. The horizontal velocity profile adopted in the present case needs to be identical to the experimental set up reported by Liu et al. (2008) for further validation study. The velocity profile employed in the present simulation can be expressed as:

$$u = \min\left\{u^* \cdot \left(c_1 \cdot log\left(\frac{y}{\delta}\right) + c_2\right), U_\infty\right\}$$

(4.1)

where $u^*$ denotes the friction velocity near the bottom wall; $c_1$ and $c_2$ are the constants from the velocity profile adaption, with the value of 0.1006 and 0.9656, respectively. The initial value of velocity in vertical direction is set to be zero and the values of $k$ and $\omega$ are calculated as

follows:

$$k(y) = max\left\{C_\mu^{-\frac{1}{2}}\left(1 - \frac{y}{\delta}\right) \times \left|1 - \frac{y}{\delta}\right| u^{*2}, 0.0001U_\infty^2\right\}$$ (4.2)

$$\omega = \frac{k^{0.5}}{C_\mu^{0.5} l}$$ (4.3)

$$l = min\left\{ky(1 + 3.5\frac{y}{\delta})^{-1}, C_\mu\delta\right\}$$ (4.4)

where $C_\mu = 0.09$ denotes the turbulent viscosity; $\kappa$ is the von Kármán constant with the value of 0.41. $l$ is the turbulence length scale (Brørs 1999; Ong et al. 2010).

## 4.2.2 Wall

Dirichlet boundary conditions are adopted on the wall patches, including the bottom wall and the surface of the structure. According to the no-slip condition, $u_1$ and $u_2$ are constraint to be zero at wall boundaries. Additionally, the standard near-wall function is employed to bridge the near wall region and the turbulence fully developed region. The dimensionless wall distance from the wall is denoted as $y^+$ and can be calculated by Eq. (4.5):

$$y^+ = \frac{\Delta y u_t}{v}$$ (4.5)

where $\Delta y$ denotes the absolute distance from the wall, $v$ is the kinematic viscosity, and $u_t$ is the friction velocity. In order to use the wall function approach for solve the turbulence flow at highly viscosity-affected region, the value of $y^+$ is curtailed within a certain range $30 < y^+ < 300$.

## 4.2.3 Outlet

Both Neumann boundary conditions and Dirichlet boundary conditions are implemented on the

patch of outlet and top. In this study, $u_1$, $u_2$, $k$ and $\omega$ are assigned with zero gradient at the outlet. The gradient of pressure is continuously restricted with zero through the whole domain. However, a reference value of pressure is required in OpenFOAM; thus, a Dirichlet boundary condition with the fixed pressure p=0 is specified at the outlet. At the top, $k$, $\omega$ and pressure are specified as the zero gradient; Dirichlet boundary conditions with $u_1 = u_\infty$, $u_2=0$ are implied. The 'front and back' patches are specified as empty since the problem is two-dimensional.

## 4.3   Computational Mesh

As mentioned in Chapter 3.1.1, the computational mesh is basically used to discretize the domain into finite cells, on which a set of the governing equations are solved. The accuracy of a solution is highly dependent on the density of the mesh as well as the shape of individual cell. Meshes can be classified as: Structured mesh, Unstructured mesh and Hybrid mesh containing a mixture of two former types.

The computational meshes applied in the present simulation are structured mesh. This type of meshes has typically quadrilateral cells in 2D and hexahedra in 3D (Cencel & Cimbala 2006). A structured mesh is characterized by regular connectivity. Generally, the structured mesh is favorable over the unstructured mesh due to its finer grid resolution and convergence advantages.

In this work, the mesh is generated in GMSH. The whole domain is separated into several blocks as shown in Figure 4.3,
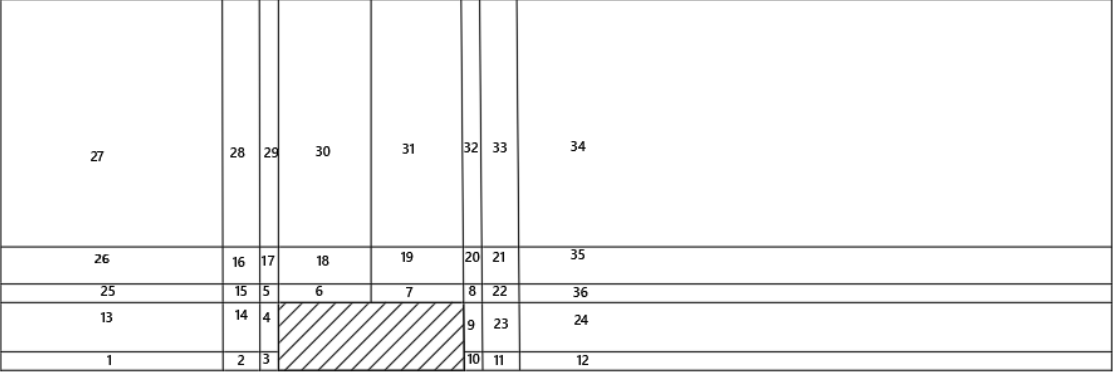


Figure 4.3: The block-topology for simulation of the structure.

The primary interest in this study is to capture the flow behaviors of the vortices occurring after the flow attacked the target body. In order to achieve better alignment with flow patterns, the mesh grid should be condensed in the near-wall region and gradually expanded away to the far-field with enlarging cells. Three sets of meshes have been generated, here is an example shown in Figure 4.4:



(a)                                                      (b)
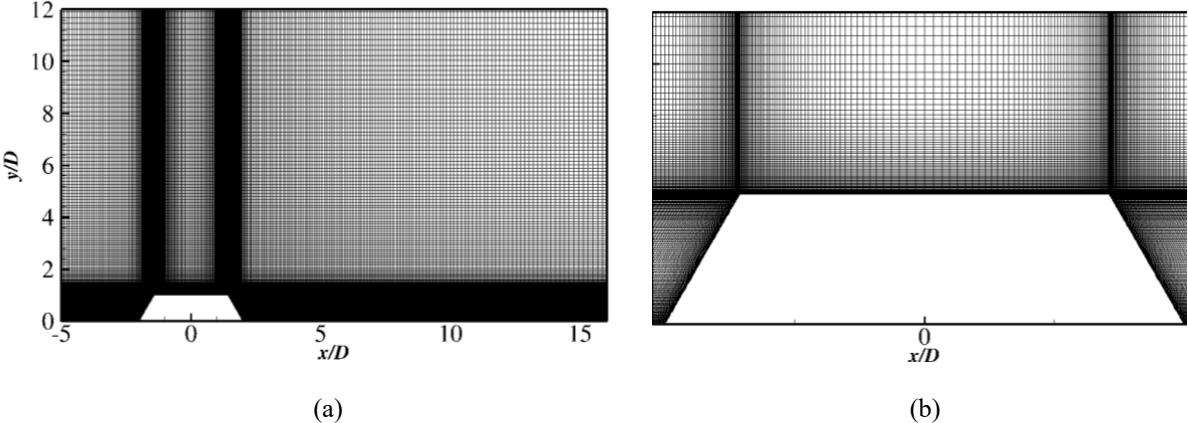
Figure 4.4: Global mesh (a) and local mesh (b) of trapezoid geometry for $\delta/D = 0.73$, $\mathrm{Re} = 1.0 \times 10^6$.

# 5 Results and Discussion

This chapter gives a presentation of the numerical results of simulations for flow over target structures. Further discussion and description of the numerical findings are outlined in this chapter with a focus on high-Reynolds number flow. Thus, the simulation results of flow at $Re = 0.5 \times 10^6$ are only involved in the validation study. For sake of clarity, all other results are exhibited in Appendix A.

## 5.1 Convergence study

A convergence test is essential for any CFD simulation to assess whether the results obtained are independent on the mesh resolutions. CFD simulations are performed with three different continually refining meshes for each case. In this study, a steady state solver is implemented and two examples of the variations of $C_d$ and $C_l$ with the iteration number for the case ($\alpha = 0°$ and $45°$ with $\delta/D = 0.73$ at $Re = 1.0 \times 10^6$ ) are shown in

Figure 5.1. It is shown that the values of $C_d$ and $C_l$ fluctuate with the iteration number. However, the fluctuations are small around mean values, which indicates that the simulation is steady and the values of $C_d$ and $C_l$ are obtained as the averaged value over a number of iterations within the steady state.
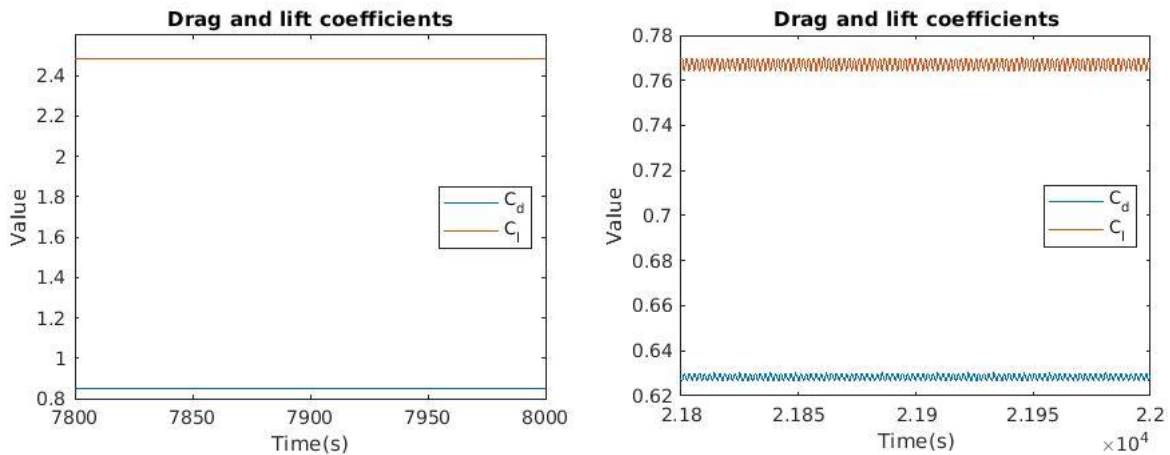


Figure 5.1: Time history of $C_d$ and $C_l$ shows the steady of simulation.

The drag coefficient $C_d$ as well as the lift coefficient $C_l$ at high Reynolds number flows are of primary interest in the further study. Thus, the cases of $Re = 1.0 \times 10^6$ and $Re = 2.0 \times 10^6$, are presented in the following tables. Since the wall functions are applied for all the simulations, the log-law layer has a region of $y^+>30$. In the present study, $y^+$ varies between 30 and 42 for

the square and trapezoidal structures in all cases.

| Case | Mesh | α | $C_d$ | Difference | $C_l$ | Difference | $y^+$ wall | $y^+$ bed | $x_R/D$ | Difference |
|------|------|---|-------|-----------|-------|-----------|-----------|----------|---------|-----------|
| A1 | 57280 | 0 | 0.8477 | | 0.6131 | | 33.5536 | 38.0027 | 15.6600 | |
| A2 | 79840 | 0 | 0.8393 | -0.99% | 0.6123 | -0.13% | 34.8382 | 40.4367 | 15.5700 | -0.57% |
| A3 | 125972 | 0 | 0.8313 | -0.95% | 0.6126 | 0.05% | 35.5669 | 39.1845 | 15.3480 | -1.43% |
| B1 | 57280 | 30 | 0.8055 | | 0.4344 | | 32.2598 | 30.3071 | 15.8700 | |
| B2 | 79840 | 30 | 0.7996 | -0.74% | 0.4322 | -0.50% | 33.7753 | 32.3192 | 15.9060 | 0.23% |
| B3 | 125972 | 30 | 0.7878 | -1.47% | 0.4347 | 0.58% | 34.6963 | 31.0468 | 15.6240 | -1.77% |
| C1 | 57280 | 45 | 0.7317 | | 0.3307 | | 30.5001 | 33.5814 | 15.3780 | |
| C2 | 79840 | 45 | 0.7292 | -0.34% | 0.3278 | -0.88% | 30.6796 | 39.0339 | 15.4800 | 0.66% |
| C3 | 125972 | 45 | 0.7150 | -1.95% | 0.3385 | 3.28% | 34.6440 | 34.6949 | 14.8500 | -4.07% |
| D1 | 57280 | 60 | 0.6310 | | 0.1930 | | 31.7176 | 39.9577 | 14.7240 | |
| D2 | 79840 | 60 | 0.6284 | -0.41% | 0.1918 | -0.61% | 36.6747 | 41.2286 | 14.7420 | 0.12% |
| D3 | 125972 | 60 | 0.6224 | -0.95% | 0.1896 | -1.15% | 37.7500 | 40.6068 | 14.7540 | 0.08% |

Table 5.1: Hydrodynamic quantities for $\alpha = 0°, 30°, 45°, 60°$ at Re $= 1 \times 10^6$ with δ/D = 0.73.

| Case | Mesh | α | $C_d$ | Difference | $C_l$ | Difference | $y^+ wall$ | $y^+$ bed | $x_R/D$ | Difference |
|------|------|---|-------|-----------|-------|-----------|-----------|----------|---------|-----------|
| A4 | 72205 | 0 | 0.8552 | | 0.6186 | | 38.4778 | 37.8724 | 15.6540 | |
| A5 | 95410 | 0 | 0.8507 | -0.53% | 0.6204 | 0.31% | 38.5057 | 36.6605 | 15.4860 | -1.07% |
| A6 | 141117 | 0 | 0.8483 | -0.28% | 0.6269 | 1.04% | 38.5627 | 37.3879 | 15.2280 | -1.67% |
| B4 | 72205 | 30 | 0.8083 | | 0.4372 | | 37.6661 | 40.3768 | 15.8700 | |
| B5 | 95410 | 30 | 0.8034 | -0.61% | 0.4392 | 0.46% | 37.7717 | 39.1643 | 15.7260 | -0.91% |
| B6 | 141117 | 30 | 0.7990 | -0.55% | 0.4406 | 0.31% | 30.9994 | 32.9971 | 15.6780 | -0.31% |
| C4 | 72205 | 45 | 0.7319 | | 0.3326 | | 34.5555 | 42.1917 | 15.3780 | |
| C5 | 95410 | 45 | 0.7252 | -0.92% | 0.3336 | 0.31% | 34.9865 | 40.9650 | 15.2760 | -0.66% |
| C6 | 141117 | 45 | 0.7190 | -0.85% | 0.3337 | 0.03% | 35.3154 | 41.3092 | 15.3000 | 0.16% |
| D4 | 72205 | 60 | 0.6285 | | 0.0485 | | 32.0002 | 39.0478 | 14.7240 | |
| D5 | 95410 | 60 | 0.6256 | -0.45% | 0.0483 | -0.37% | 33.8713 | 40.1299 | 14.7240 | 0.00% |
| D6 | 141117 | 60 | 0.6227 | -0.46% | 0.0487 | 0.84% | 32.6059 | 35.2102 | 14.7060 | -0.12% |

Table 5.2: Hydrodynamic quantities for $\alpha = 0°, 30°, 45°, 60°$ at Re $= 2 \times 10^6$ with δ/D = 0.73.

| Case | Mesh | α | $C_d$ | Difference | $C_l$ | Difference | $y^+$wall | $y^+$ bed | $x_R/D$ | Difference |
|------|------|---|-------|-----------|-------|-----------|-----------|-----------|---------|-----------|
| A10 | 57280 | 0 | 0.7478 | | 0.5523 | | 36.6521 | 31.4216 | 15.7800 | |
| A11 | 79840 | 0 | 0.7396 | -1.10% | 0.5500 | -0.42% | 32.9154 | 37.2428 | 15.6600 | -0.76 % |
| A12 | 125972 | 0 | 0.7332 | -0.86% | 0.5495 | -0.09% | 38.9124 | 32.3845 | 15.4200 | -1.53 % |
| B10 | 57280 | 30 | 0.7044 | | 0.3930 | | 32.2355 | 32.4969 | 15.8880 | |
| B11 | 79840 | 30 | 0.6991 | -0.76% | 0.3901 | -0.75% | 33.8555 | 34.6895 | 15.8820 | -0.04 % |
| B12 | 125972 | 30 | 0.6877 | -1.62% | 0.3919 | 0.47% | 34.8059 | 33.2401 | 15.5460 | -2.12 % |
| C10 | 57280 | 45 | 0.6404 | | 0.3054 | | 34.6817 | 32.2254 | 15.1620 | |
| C11 | 79840 | 45 | 0.6344 | -0.93% | 0.2976 | -2.55% | 36.8158 | 31.1566 | 15.3660 | 1.35 % |
| C12 | 125972 | 45 | 0.6210 | -2.12% | 0.3081 | 3.51% | 39.6933 | 33.0693 | 14.6700 | -4.53 % |
| D10 | 57280 | 60 | 0.5519 | | 0.1789 | | 32.1451 | 31.1317 | 14.6160 | |
| D11 | 79840 | 60 | 0.5496 | -0.43% | 0.1768 | -1.18% | 35.8353 | 33.0906 | 14.6340 | 0.12 % |
| D12 | 125972 | 60 | 0.5436 | -1.09% | 0.1738 | -1.69% | 38.3686 | 37.6792 | 14.6460 | 0.08 % |

Table 5.3: Hydrodynamic quantities for $\alpha = 0^\circ, 30^\circ, 45^\circ, 60^\circ$ at Re $= 1 \times 10^6$ with δ/D = 1.96.

| Case | Mesh | α | $C_d$ | Difference | $C_l$ | Difference | $y^+$ wall | $y^+$ bed | $x_R/D$ | Difference |
|------|------|---|-------|-----------|-------|-----------|-----------|-----------|---------|-----------|
| A13 | 72205 | 0 | 0.7536 | | 0.5565 | | 36.2433 | 34.8225 | 15.7620 | |
| A14 | 95410 | 0 | 0.7496 | -0.53% | 0.5579 | 0.26% | 36.2357 | 33.7148 | 15.5760 | -1.18 % |
| A15 | 141117 | 0 | 0.7462 | -0.44% | 0.5594 | 0.27% | 36.1572 | 34.2562 | 15.4440 | -0.85 % |
| B13 | 72205 | 30 | 0.7060 | | 0.3957 | | 35.8604 | 37.3221 | 15.8460 | |
| B14 | 95410 | 30 | 0.7013 | -0.66% | 0.3972 | 0.38% | 35.9445 | 36.2114 | 15.6780 | -1.06 % |
| B15 | 141117 | 30 | 0.6971 | -0.60% | 0.3974 | 0.04% | 35.8981 | 36.6438 | 15.6240 | -0.34 % |
| C13 | 72205 | 45 | 0.6353 | | 0.3029 | | 33.0664 | 39.1488 | 15.2520 | |
| C14 | 95410 | 45 | 0.6292 | -0.97% | 0.3036 | 0.25% | 32.4215 | 33.1609 | 15.1260 | -0.83 % |
| C15 | 141117 | 45 | 0.6233 | -0.94% | 0.3030 | -0.20% | 33.8389 | 38.3989 | 15.1200 | -0.04 % |
| D13 | 72205 | 60 | 0.5487 | | 0.0449 | | 30.6921 | 36.3795 | 14.5980 | |
| D14 | 95410 | 60 | 0.5459 | -0.50% | 0.0447 | -0.58% | 31.8644 | 35.4413 | 14.5860 | -0.08 % |
| D15 | 141117 | 60 | 0.5436 | -0.42% | 0.0451 | 0.87% | 30.1615 | 34.7096 | 14.5440 | -0.29 % |

Table 5.4: Hydrodynamic quantities for $\alpha = 0^\circ, 30^\circ, 45^\circ, 60^\circ$ at Re $= 2 \times 10^6$ with δ/D = 1.96.

A convergence study is conducted to ensure that the results of the analysis are not affected by changing the size of the mesh. The results of the convergence test are displayed in Figure 5.1

to Figure 5.3. As observed from

Table 5.1 and Figure 5.2 (a), for the case of $Re = 1.0 \times 10^6$ and $\delta/D = 0.73$, three classes of meshes with 57280, 79840 and 125972 cells are arranged to perform the grid convergence study. It is observed that $C_d$ and $C_l$ varies slightly with a relative difference which is less than the threshold of 5 %. Here the relative difference is calculated by $(\varphi_{i+1} - \varphi_i)/(\varphi_i)(i = 1,2)$, where $\varphi$ denotes the quantities of different meshes. Hence, all three meshes with different grid density are considered to achieve sufficient numerical accuracy.



(a)



(b)

Figure 5.2: Mesh Convergence with respect to hydrodynamic coefficients $C_d$ (left) and $C_l$ (right) at $Re = 1.0 \times 10^6$ with (a) $\delta/D = 0.73$ and (b) $\delta/D = 1.96$.

The same set of meshes are adopted to carry out the convergence study for the flow condition at $Re = 1.0 \times 10^6$ with $\delta/D = 1.96$. As shown in

Table 5.3 and Figure 5.2(b), the maximum relative variation in $C_d$ and $C_l$ are 2.12% and 3.51 %, respectively, between meshes with 79840 cells and 125972 cells for the structure with

the slope angle of $45°$.

Similarly, for the case at $\text{Re} = 2.0 \times 10^6$ with $\delta/D = 0.73$ and the case at $\text{Re} = 2.0 \times 10^6$ with $\delta/D = 1.96$, the convergence studies have been conducted by using the same set meshes with 72205, 95140 and 141117 elements. The relative variations are within the threshold of $5\%$. Thus, it can be concluded that the sufficient grid resolution has been achieved among all cases in present study.
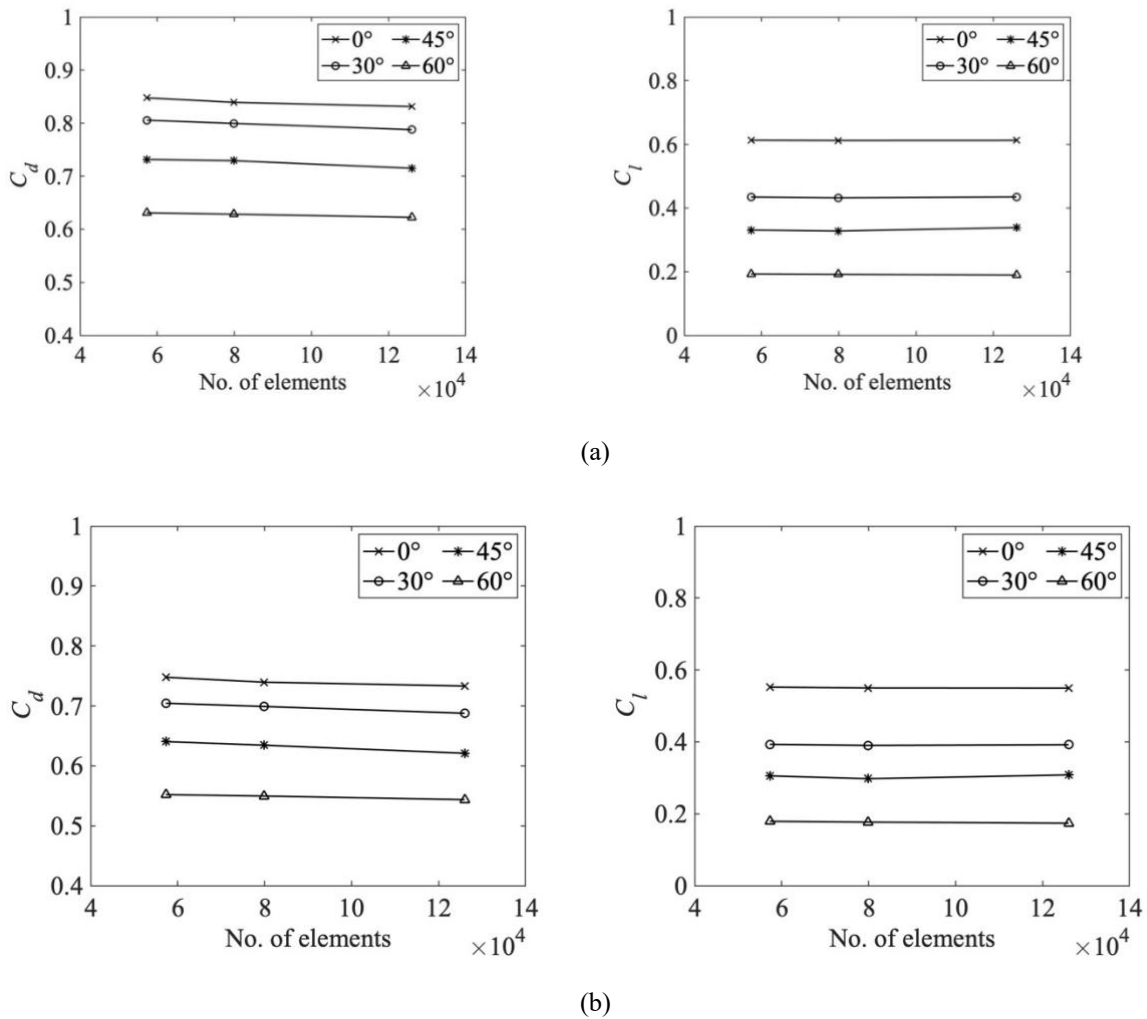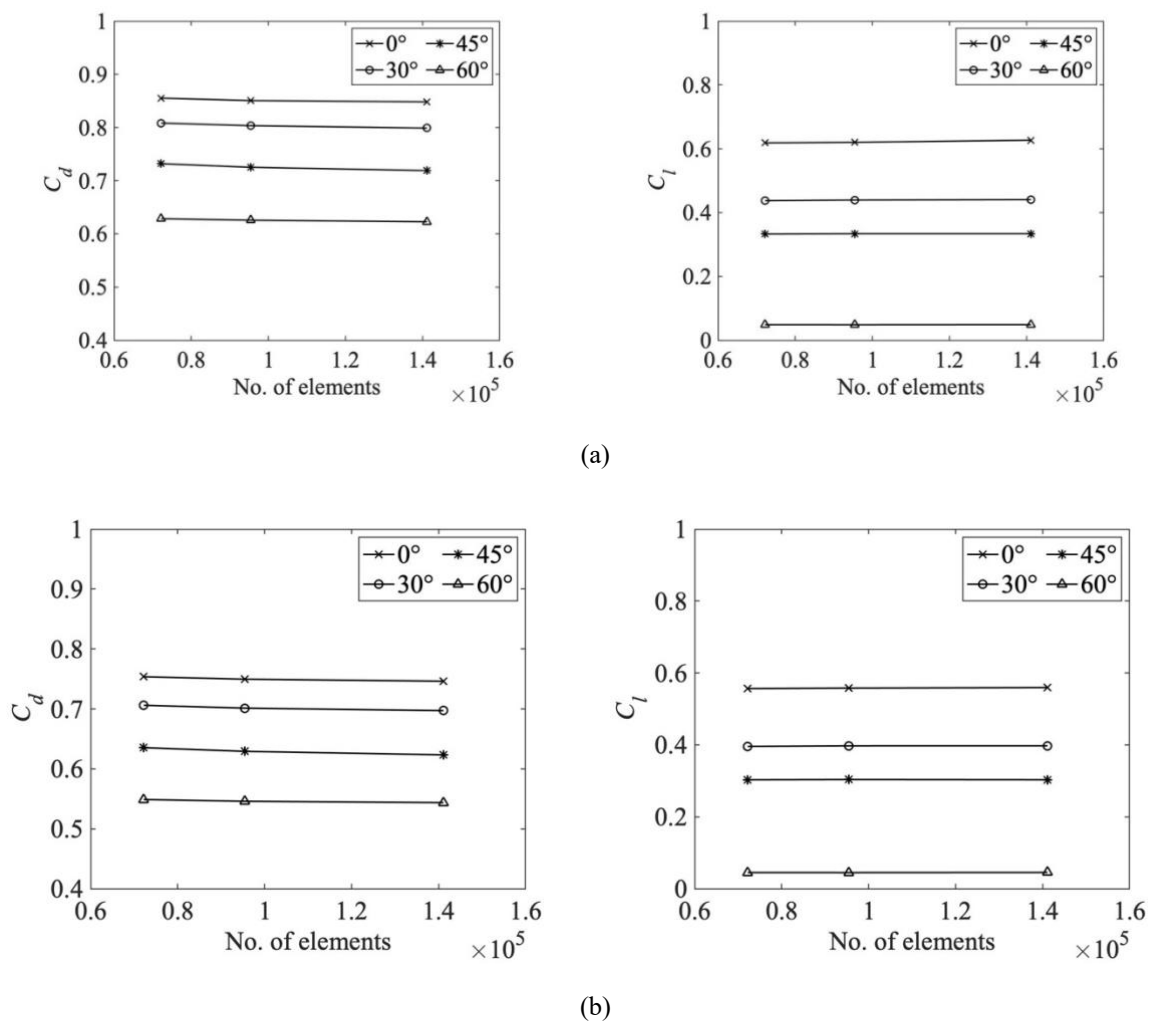


(a)



(b)

Figure 5.3: Mesh Convergence with respect to hydrodynamic coefficients $C_d$ (left) and $C_l$ (right) at (a) $\text{Re} = 1.0 \times 10^6$ and (b) $\text{Re} = 2.0 \times 10^6$ with $\delta/D = 1.96$.

## 5.2  Validation Study

In order to examine the validity of the present 2D RANS method combined with $k - \omega\ SST$ turbulence model, a simulation of flow over a wall-mounted square cover has been carried out. A validation study has been conducted by comparing this simulation with the experimental measurements performed by Liu et al. (Liu et al. 2008). The present simulation is performed at $Re = 0.5 \times 10^6$ with $\delta/D = 0.73$ while the experiments were carried out at $Re = 3.41 \times 10\verb|^|4$ with $\delta/D = 0.75$. The finest set of meshes are applied in validation study and the numerical results are displayed in Table 5.5:

| Case | Mesh | α | $C_d$ | Difference | $C_l$ | Difference | $y^+$ wall | $y^+$ bed |
|------|------|---|-------|-----------|-------|-----------|-----------|-----------|
| S1 | 72205 | 0 | 0.9351 | | 0.1444 | | 35.6982 | 36.5489 |
| S2 | 95410 | 0 | 0.9274 | -0.82% | 0.1432 | -0.87% | 35.8951 | 38.7611 |
| S3 | 141117 | 0 | 0.9284 | 0.11% | 0.1421 | -0.77% | 35.1796 | 37.8548 |

Table 5.5: Hydrodynamic quantities for square case.

The validation is performed by comparing the predicted horizontal velocity profiles with experimental data reported by Liu et al. (Liu et al. 2008) as shown in **Error! Reference source not found.**. The horizontal velocity profiles are selected at eight different locations along the x-axis in the computational domain. Two of them are the velocity profiles at the upstream of the structure, located at $x/D = -4$ and $x/D = -2$, respectively. Three of them are on the square structure and the other three are located in the downstream of the structure. It can be observed that the numerical results are generally consistent with the experimental data, especially in the upstream of the structure. However, a gradually increasing deviation from the experimental profile occurs in the downstream of the structure from location at $x/D = 0.75$. Additionally, a significant negative deviation is generated at the region close to the wall, suggesting that the recirculation zone appears behind the square structure.
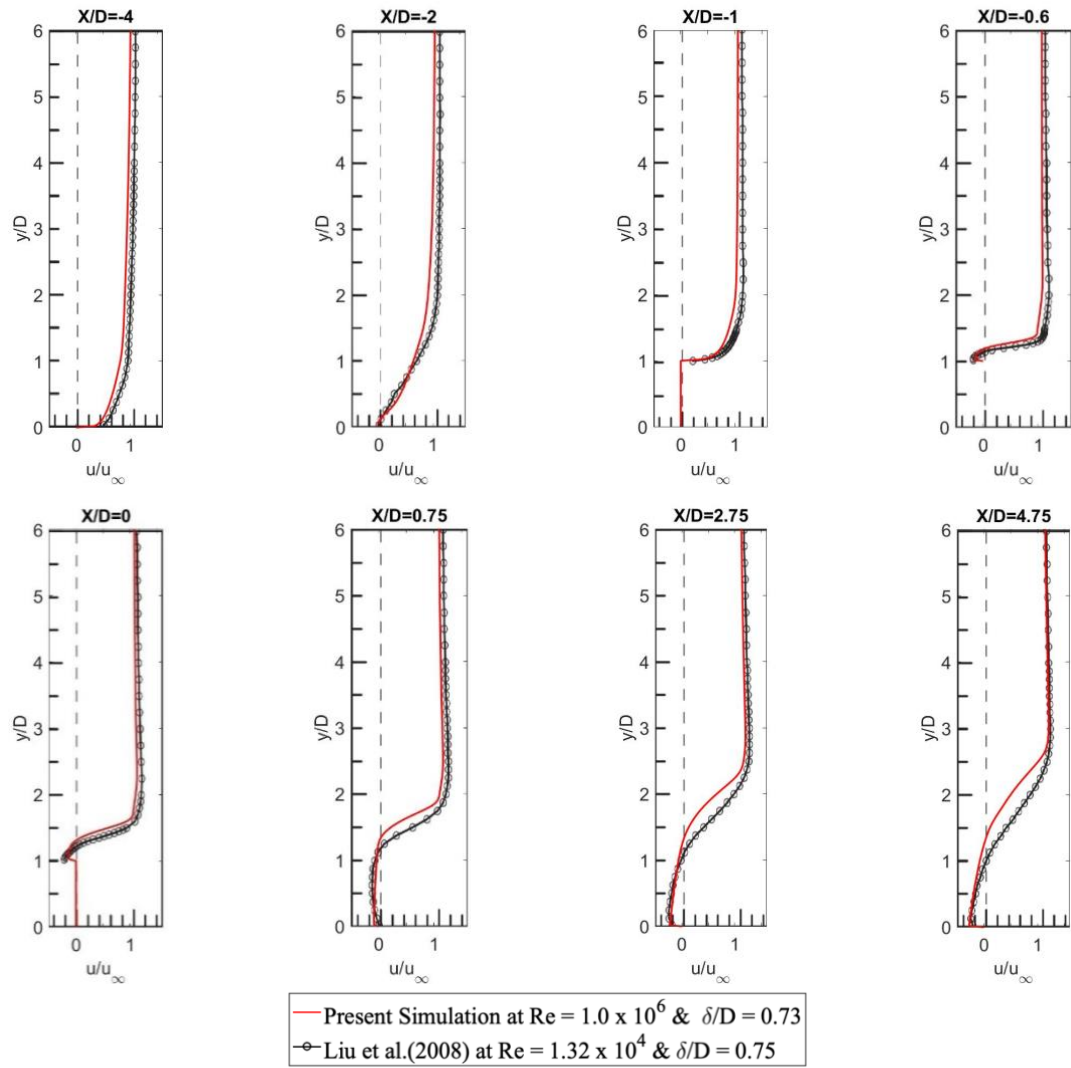
Figure 5.4: Comparisons of horizontal velocity profiles of the present simulation and the experimental data from Liu et al.(2008).

## 5.3  Effect of α on hydrodynamic coefficients

The effect of the slope angle  α  on the hydrodynamic quantities has been studied at  $Re = 1.0 \times 10^6$  and  $Re = 2.0 \times 10^6$  with boundary layer thickness  $\delta/D = 0.73 - 2.52$ . The variations of  $C_d$  and  $C_l$  with respect to the slope angle  $\alpha = 0°, 30°, 45°, 60°$  are exihibited in Figure 5.5.
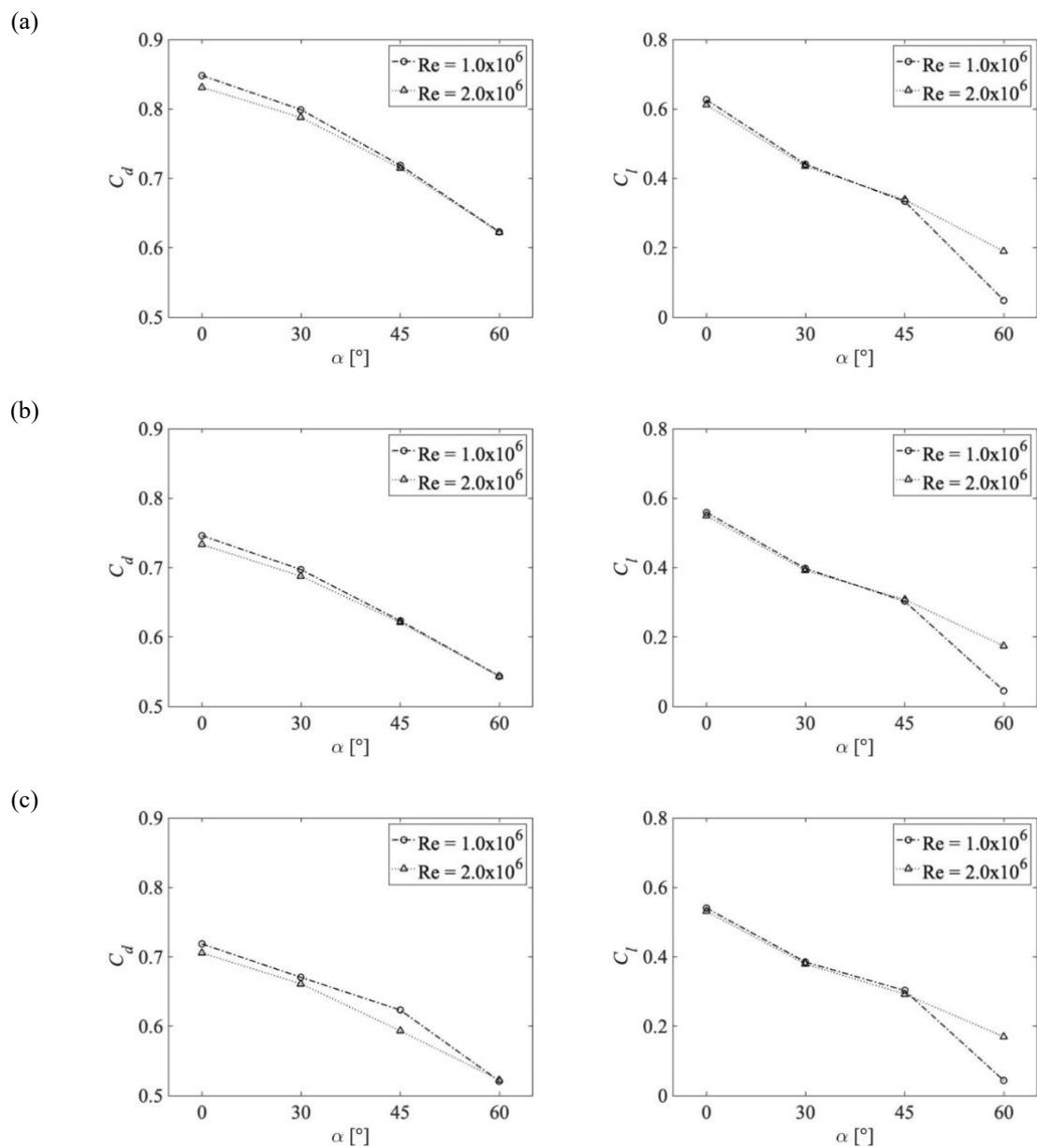


Figure 5.5: Variation of hydrodynamic coefficients versus  α  with different boundary layer thicknesses: (a) $\delta/D = 0.73$, (b)  $\delta/D = 1.96$ and (c) $\delta/D = 2.52$.

At both Reynolds numbers , the lift and the drag coefficients are monotonically declining as the slope angle rises. For the values of the drag coefficient $C_d$, as the slope angle increases, the block effect of the structure to the flow declines. The pressure difference between the front face and back face also declines. As a result, the drag force falls. For the value of $C_l$, it is noted that the projected areas for all structures are the same, so the declining $C_l$ is due to the decreasing lift force. The reason for the falling lift force can be explained as follows: with the increasing $\alpha$, the flow velocity above the structure drops, resulting in an growing negative pressure above the structure and the lift force reduces. It should be also noted that from $\alpha = 45°$ to $\alpha = 60°$, the decreasing of $C_l$ is stronger than other $\alpha$.

## 5.4  Effect of Reynolds number on hydrodynamic coefficients

A further study about the effect of Reynolds numbers on hydrodynamic quantities $C_d$, $C_l$ has been carried out for the structures with all $\alpha$ at $Re = 1.0 \times 10^6$ to $Re = 2.0 \times 10^6$. As demonstrated in Figure 5.6, the variation of the drag coefficient is almost independent of the slope angle $\alpha$. In general, the drag coefficient would increase as Reynolds number increases. However, with $\alpha = 60°$, the effect from change of the Reynolds number is barely visible. This can be attributed to the reason that with $\alpha = 60°$, the structure tends to be flat and the two slopes are close to be horizontal. The resulting contribution of pressure difference to the drag decreases while the contribution of the viscous effect increases. The reason is that at high Reynolds number, the viscous effect tends to be smaller; then, a decreasing value of $C_d$ is caused.

Apart from rising $C_d$ with increasing Reynolds number, it is also found that the lift coefficient $C_l$ slightly increases as the slope angle $\alpha$ varies from $0°$ to $30°$. Nevertheless, an adverse effect on $C_l$ is noted as Reynolds number increases for the case with $\alpha = 60°$.

(a)



(b)



(c)



(d)
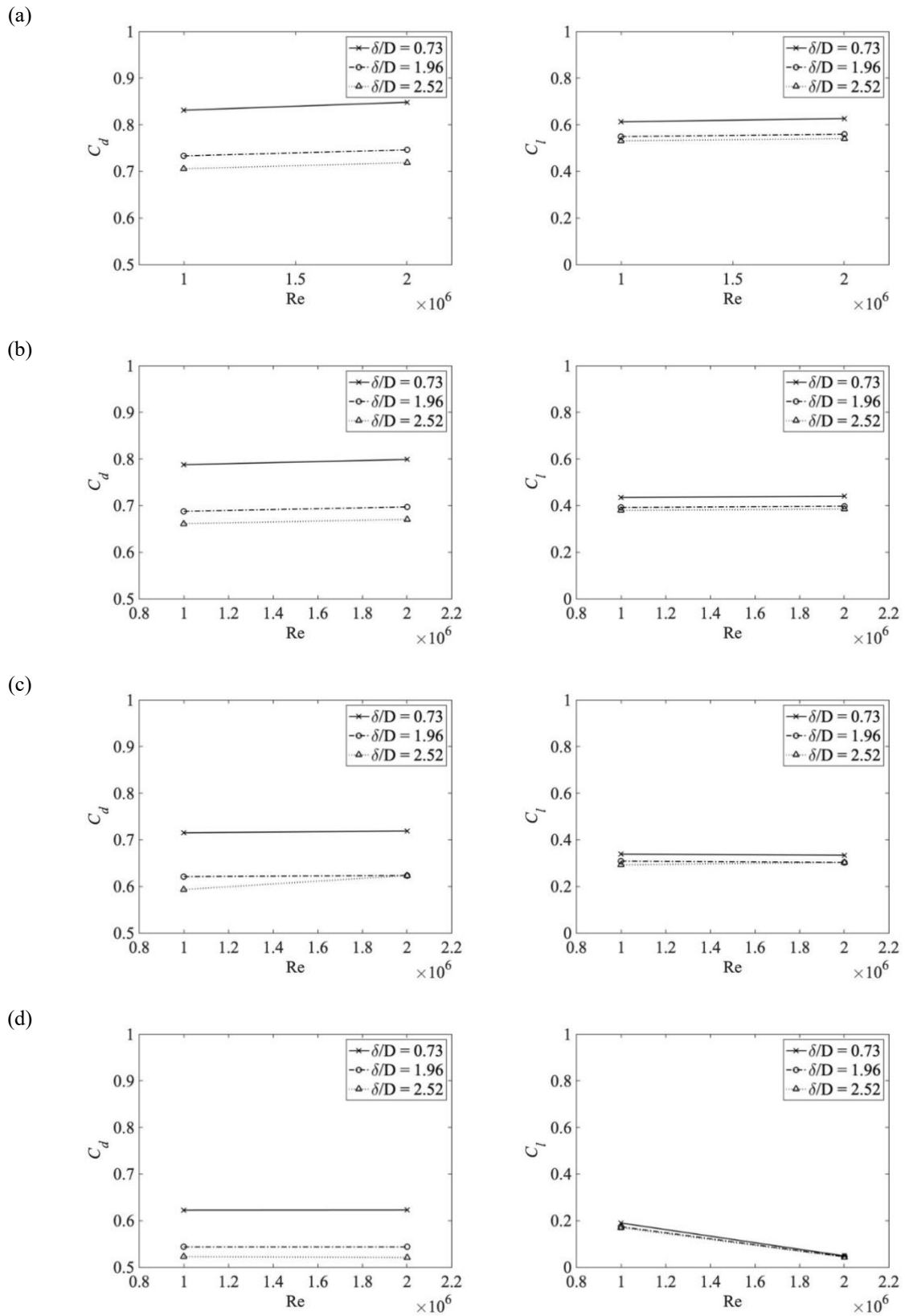


Figure 5.6: Variation of Hydrodynamic coefficients with respect to different Reynolds numbers at different angles of slope: (a) $\alpha = 0\degree$, (b) $\alpha = 30\degree$ and (c) $\alpha = 45\degree$, (d) $\alpha = 60\degree$.

## 5.5 Effect of δ/D on hydrodynamic quantities

The effect of normalized thickness $\delta/D$ on the hydrodynamic quantities is investigated at the nodimensional boundary layer thickness of 0.73, 1.96 and 2.52, as exhibited in **Error! Reference source not found.**.
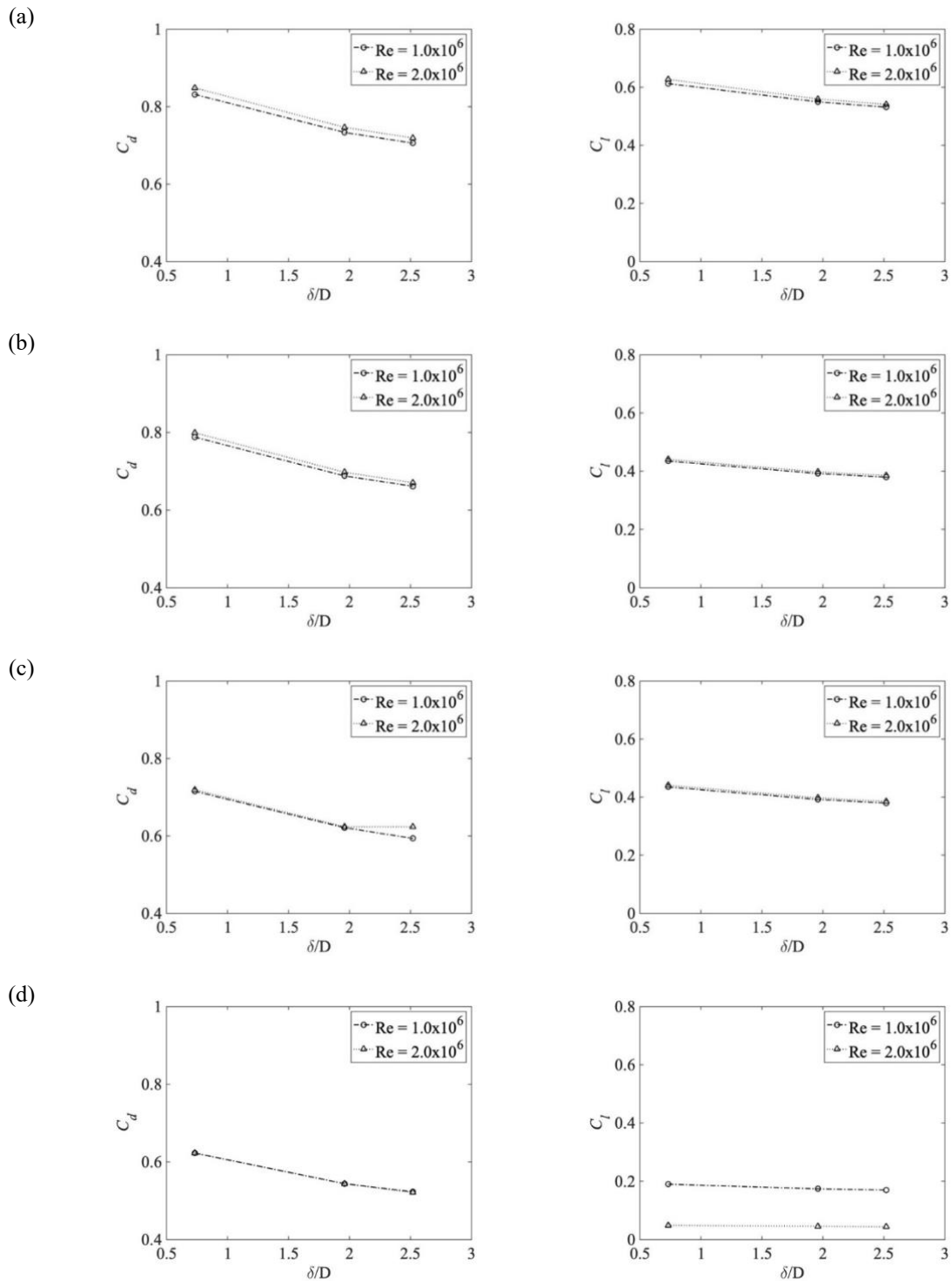
(a)



(b)



(c)



(d)



Figure 5.7: Variation of Hydrodynamic coefficients with respect to different boundary layer thicknesses at

different angles of slope: (a) α = 0˚, (b) α = 30˚and (c) α = 45˚, (d) α = 60˚.

It is clear that both $C_d$ and $C_l$ decreases as δ/D increases. This is due to the fact that the increase in δ/D causes a drop in averaged velocity of the boundary layer flow that the structure is subjected to. Consequently, the pressure around the structure declines, resulting in a decreasing force on the structure.

## 5.6  Pressure distribution

The drag and lift forces are generally dominated by the pressure difference around the structure. Therefore, it is necessary to investigate the pressure distributions in the flow field. The pressure distributions throughout the near-wake region around the rectangular and trapezoidal structures are presented in this section.
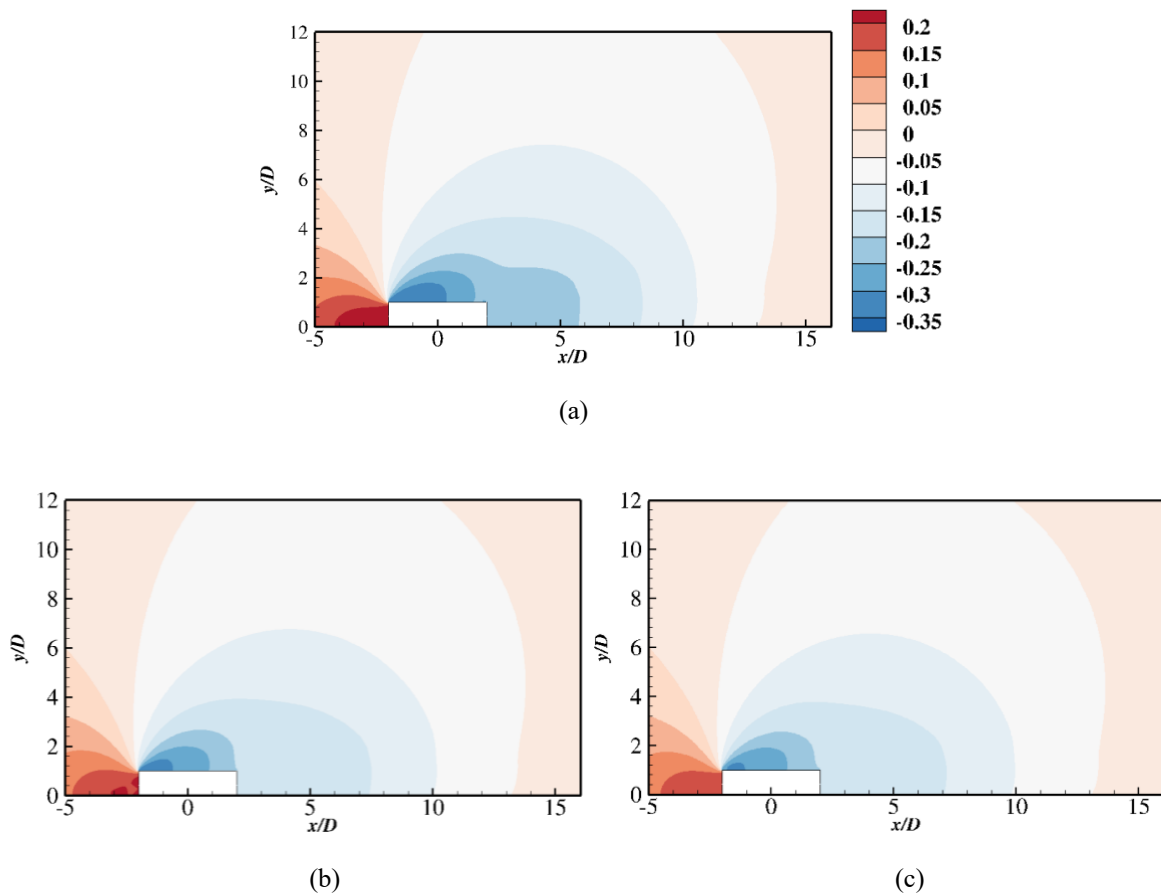


(a)

(b)                              (c)

Figure 5.8: Pressure distribution for the rectangular cylinder with α=0° at Re $= 1 \times 10^6$ with various boundary layer thicknesses (a) δ/D=0.73, (b) δ/D =1.96 and (c) δ/D=2.52.

43

he contours of the pressure distributions around for $\alpha = 0°, 30°, 45°$ and $60°$at $Re = 1 \times 10^6$ with all $\delta/D$ are presented in Figure 5.8 to Figure 5.11. A high-pressure region is yielded in front of the structure due to the block effect of the structure acting on the flow. Additionally, two low-pressure regions are visible by counters for $\alpha = 0°$ in Figure 5.8. The first one is located above the rectangular structure after the separation point at the leading corner due to the flow separation. The other one is formed behind the structure. The reason behind this can be associated with the effect of the recirculation. Moreover, according to the mass conservation law, an increase in velocity is caused due to the flow separation. Hence, this increment in velocity leads to a decrement in the pressure according to the Bernoulli's equation. With the increasing $\delta/D$, the velocity of flow decreases, and the amplitude of the pressure decreases as illustrated in Figure 5.8 (b) and (c).



(a)



(b)



(c)

Figure 5.9: Pressure field for trapezoidal cylinder with α=30° immersed at $Re = 1 \times 10^6$ with various boundary layer thicknesses (a) δ/D=0.73, (b) δ/D=1.96 and (c) δ/D=2.52.

A similar phenomenon can be observed in **Error! Reference source not found.**, **Error!**

**Reference source not found.** and **Error! Reference source not found.**, which present the pressure fields around trapezoidal structures with different slope angles. It can be observed that due to the weakened block effect with the increasing α, the pressure amplitude decreases, which is in consistence with the variation of $C_d$ and $C_l$ in section 0. It is also worth noting that from α = 45° to α = 60°, with the increasing δ/D, the center of the low-pressure region behind the structure is detached from the back face of the structure and moves further downstream.



Figure 5.10: Pressure field for trapezoidal cylinder with α=45° immersed at Re = $1 \times 10^6$ with various boundary layer thicknesses (a) δ/D=0.73, (b) δ/D=1.96 and (c) δ/D =2.52.
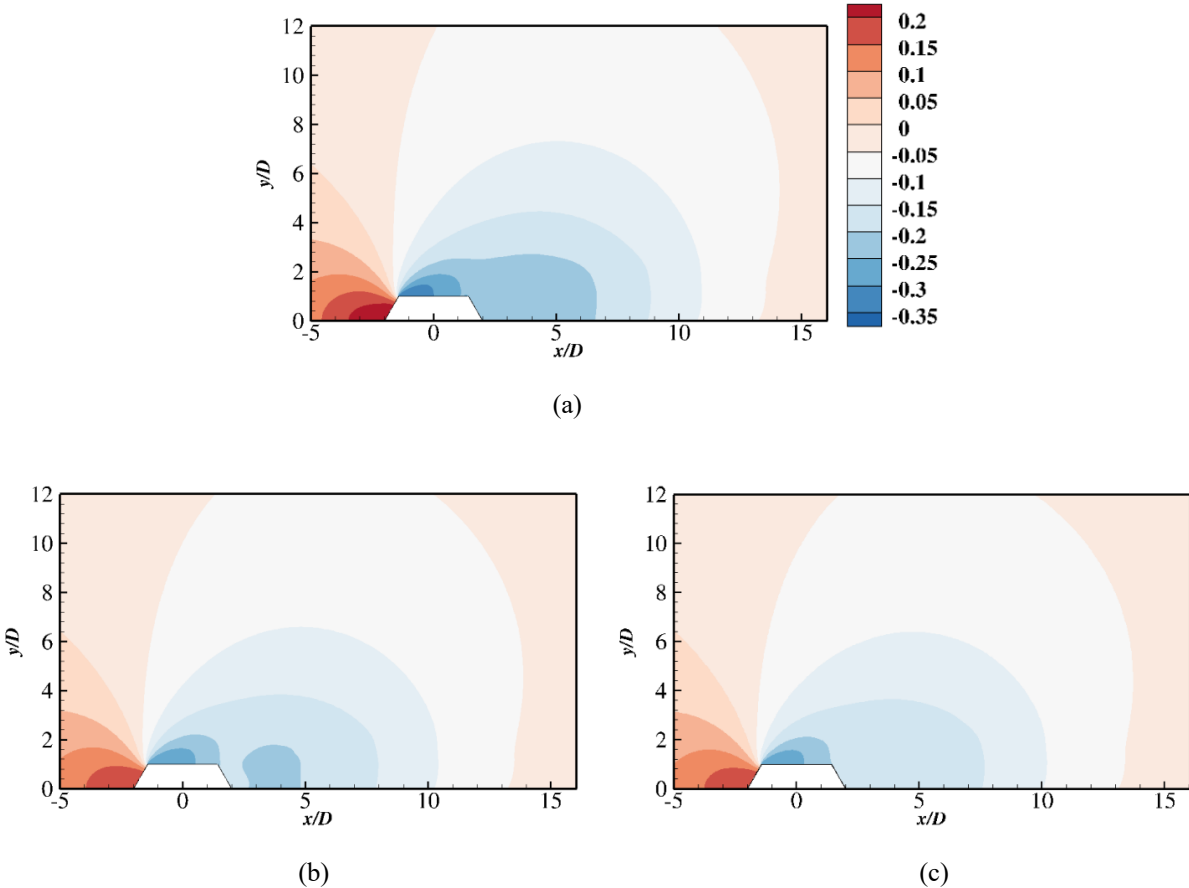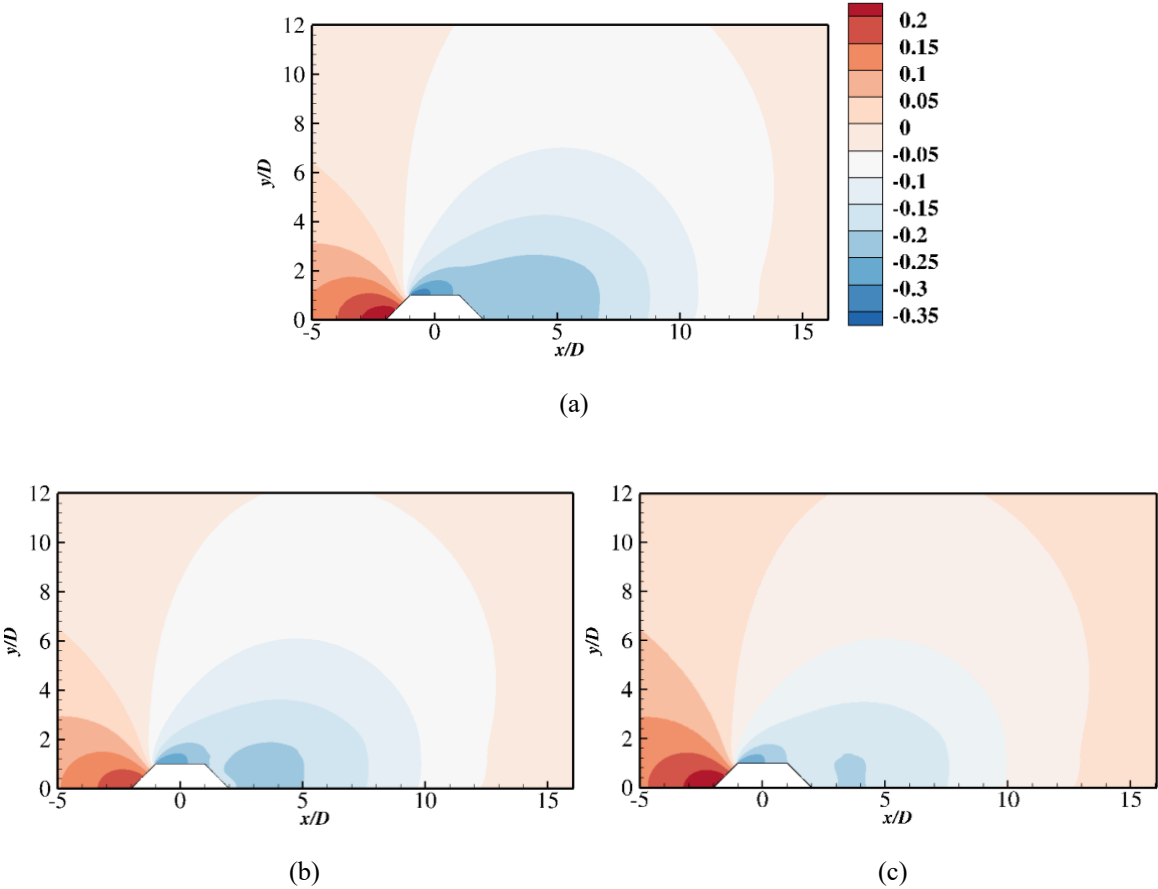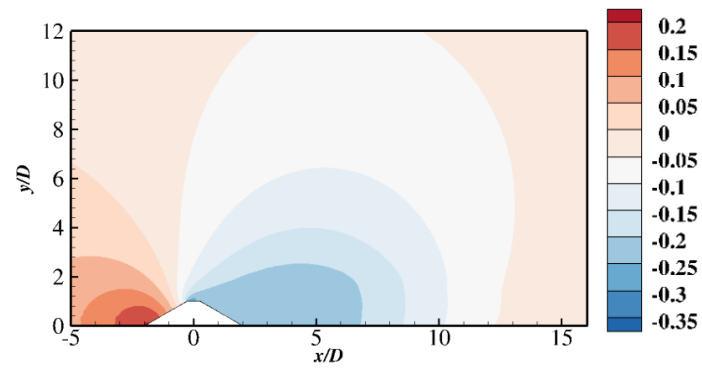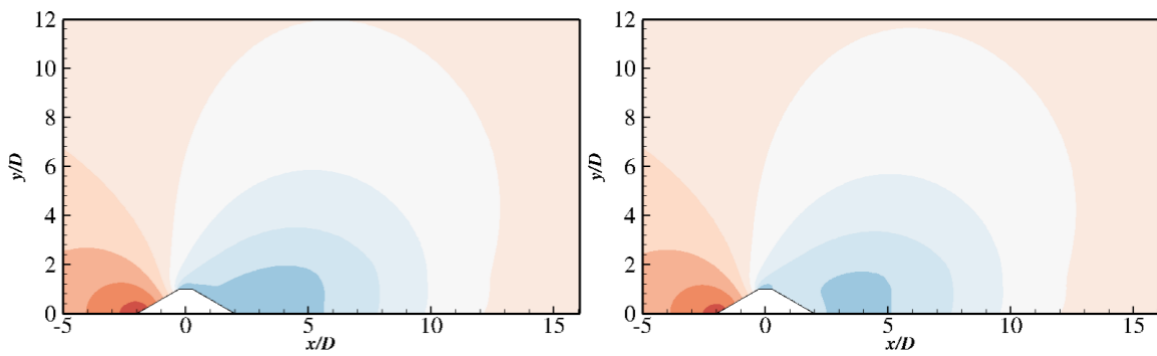
Figure 5.11: Pressure field for trapezoidal cylinder with α=60° immersed at $Re = 1 \times 10^6$ with various boundary layer thicknesses (a) δ/D=0.73, (b) δ/D=1.96 and (c) δ/D=2.52.

## 5.7 Velocity distribution

The contour plots of the horizontal velocity of the flow near the structure are presented in this section. As illustrated in

Figure 5.16, the velocity distribution of the stream past the rectangular cylinder is located within the range of $-0.2$ m/s to $1.1$ m/s. The horizontal velocity at inlet boundary and far free stream region is specified as $1$ m/s. The blocking effect of the structure on the flow is observed as there is a negative region in front of the structure. The horizontal velocity at the front face of the structure is approximately equal to zero. According to the conservation laws, the mass above and past the structure is accelerated to maintain conservation of energy. A large recirculation region behind the structure is indicated by a large negative velocity region. A high velocity region with $u/U_\infty > 1$ is formed above the structure. It should be noted that this high-speed region reduces as $\delta/D$ increases. A similar phenomenon can be observed in Figure 5.13 to Figure 5.16, but the area of the negative velocity region in front of the structure gradually reduces with increasing $\alpha$, which is consistent with the pressure distributions.



(a)

(b)                                    (c)

Figure 5.12: Velocity contour for rectangular cylinder with $\alpha = 0°$ immersed at $Re = 1 \times 10^6$ with various boundary layer thicknesses (a) $\delta/D = 0.73$, (b) $\delta/D = 1.96$ and (c) $\delta/D = 2.52$.
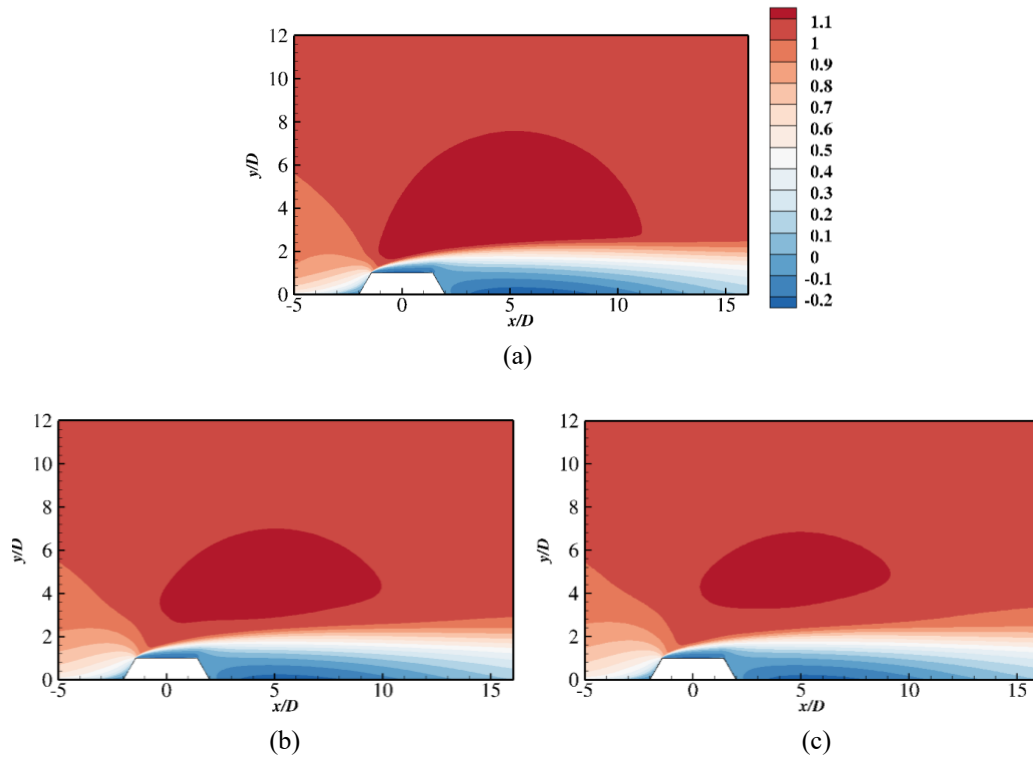
Figure 5.13: Velocity contour for trapezoidal cylinder with α=30° immersed at $Re = 1 \times 10^6$ with various boundary layer thicknesses (a) δ/D=0.73, (b) δ/D=1.96 and (c) δ/D=2.52.
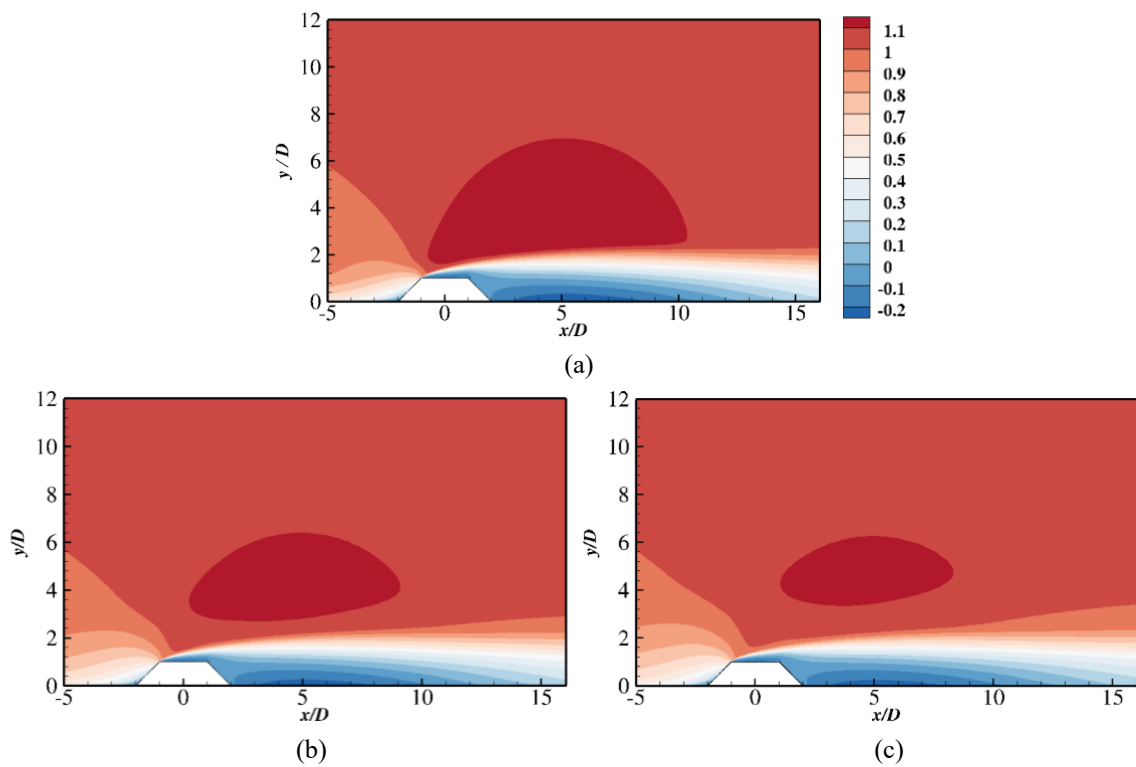


Figure 5.14: Velocity contour for trapezoidal cylinder with α=45° immersed at $Re = 1 \times 10^6$ with various boundary layer thicknesses (a) δ/D=0.73, (b) δ/D=1.96 and (c) δ/D=2.52.

Figure 5.15: Velocity contour for trapezoidal cylinder with $\alpha = 45°$ immersed at $Re = 1 \times 10^6$ with various boundary layer thicknesses (a) $\delta/D = 0.73$, (b) $\delta/D = 1.96$ and (c) $\delta/D = 2.52$.
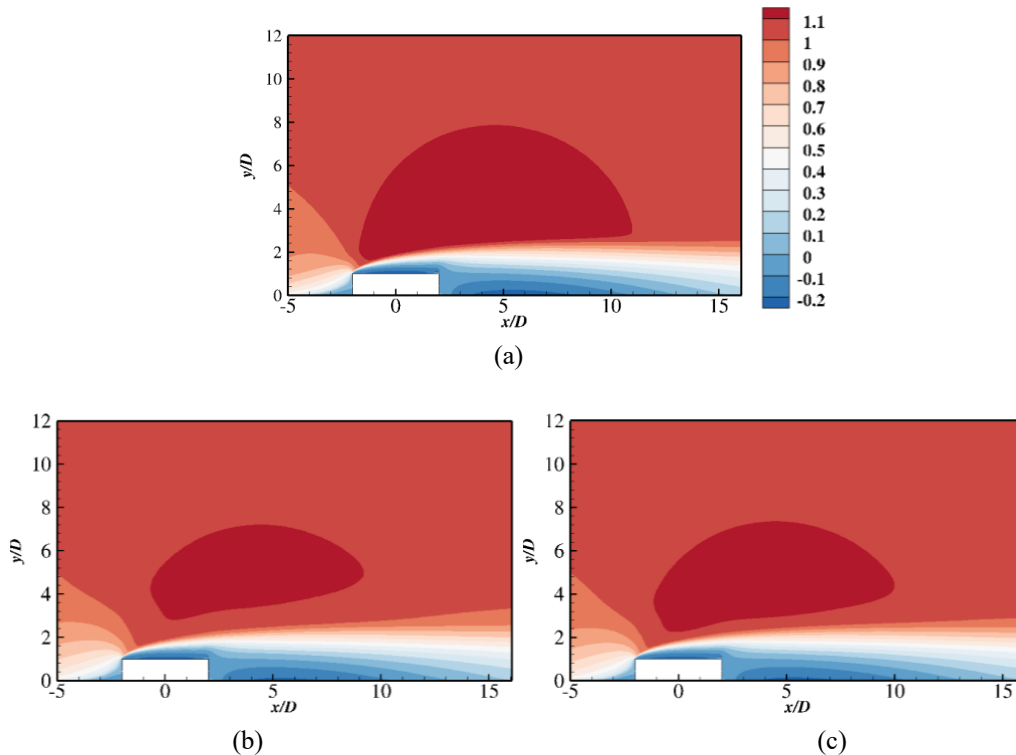


Figure 5.16: Velocity contour for trapezoidal cylinder with $\alpha = 60°$ immersed at $Re = 1 \times 10^6$ with various boundary layer thicknesses (a) $\delta/D = 0.73$, (b) $\delta/D = 1.96$ and (c) $\delta/D = 2.52$.

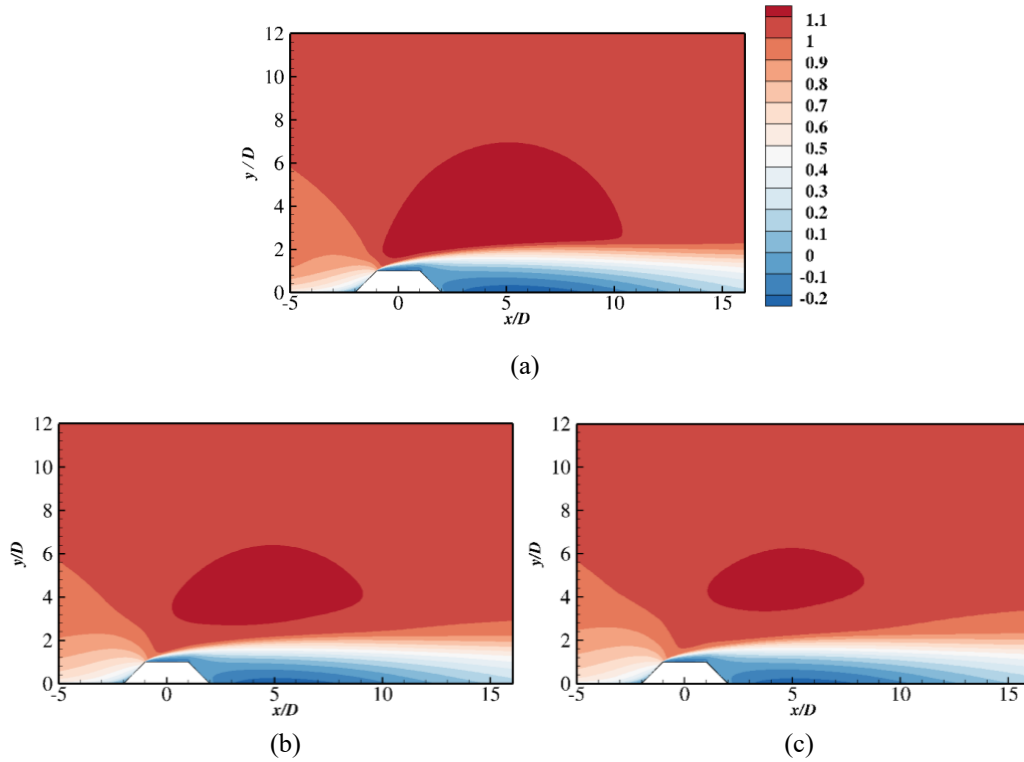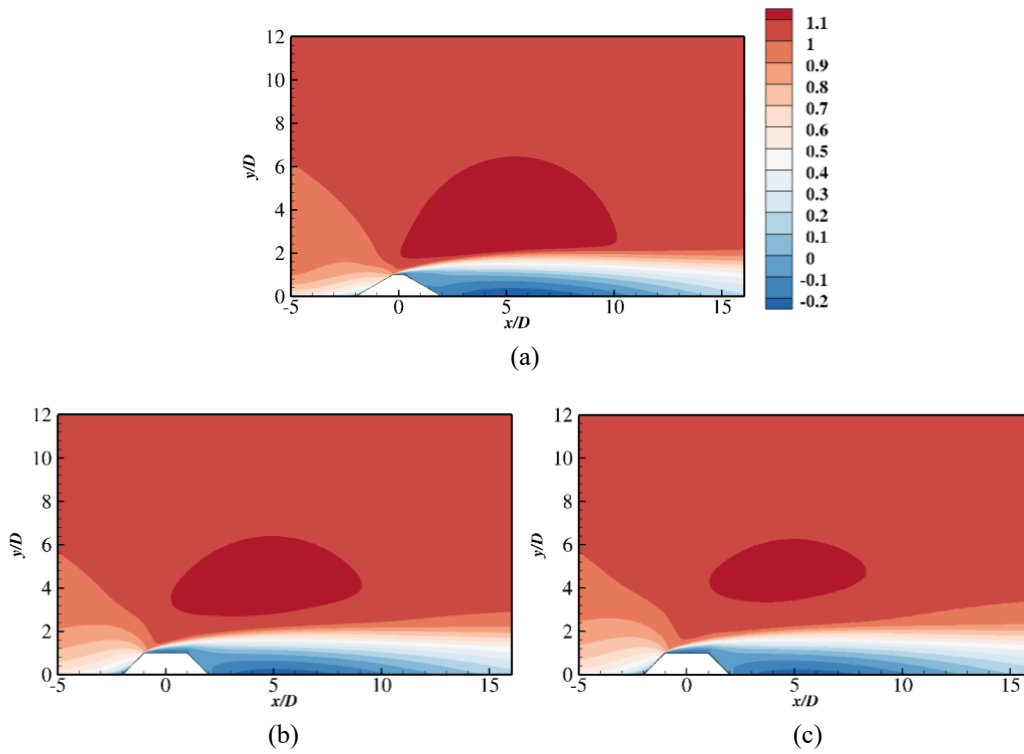## 5.8  Bed shear stress

Bed shear stress is an important quantity influencing the scour process in the real subsea environment. The scouring process is a main cause for subsea operations failures. Therefore, it is significant to study the bed shear stress induced by the wall-mounted structures in this study in order to evaluate the scour risk of the subsea cover with different geometries.

Figure 5.17 (a) shows the non-dimensional bed shear stress $\tau/\rho U_\infty^2$ along the bottom wall surface. The formulation for $\tau$ is given by:

$$\tau = \mu(\frac{\partial u}{\partial y})_{y=0} \tag{5.1}$$

Figure 5.17 (b) presents the zoom-in plots around the front face of the structures. It can be seen that $\tau/\rho U_\infty^2$ stagnates towards 0 to the front faces of all the structures. There are small negative $\tau/\rho U_\infty^2$ regions in front of the structures caused by the small recirculation motions. Furthermore, with the increase in $\alpha$, the negative $\tau/\rho U_\infty^2$ region is becoming smaller and the positive value of $\tau/\rho U_\infty^2$ becomes lower. Behind the structures, a large area of negative $\tau/\rho U_\infty^2$ is formed, indicating the large recirculation motion. The absolute minimal value of the bed shear stress increases with the increasing $\alpha$ even though the length of the negative $\tau/\rho U_\infty^2$ region is slightly decreasing. This phenomenon may be that flow energy containing in the large recirculation motions behind the structure is reduced by the small recirculation motion above the structure after the separation at the leading edge, which can be further shown in the following section about the streamlines.


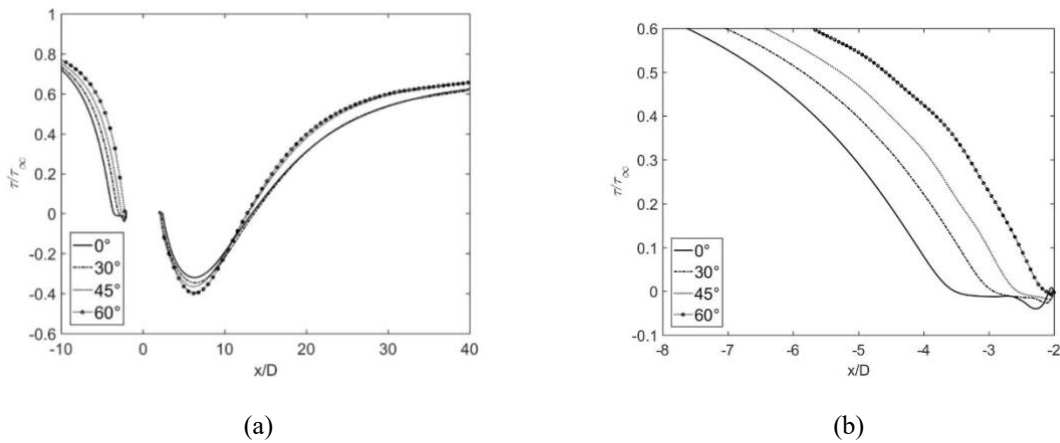
(a)                                    (b)

Figure 5.17: Bed shear stress along the bottom wall.

## 5.9 Streamlines

The streamlines of the flow over various structure geometries at $Re = 1.0 \times 10^6$ are presented in Figure 5.18. **Error! Reference source not found.**. (a) displays the flow patterns around the rectangular cylinder. It can be observed that an upstream vortex is formed, along with primary and secondary recirculation regions adjacent to the surface of the structure. The first vortex appears at the bottom corner in front of the structure, where the incoming stream is blocked by the structure. It is observed a boundary layer encounters the structure attached to the front surface, thereby causing an adverse pressure gradient in the boundary layer flow. Furthermore, the reversed flow leads to a recirculation bubble at its bottom. Such boundary layer separation from the sharp leading edge of the structure further generates a shear layer which rolls into a core of rotating vortex. The second vortex above the structure is formed due to the separation of the shear layer. While the attack angle is sufficiently large, this can be further expanded to a vortex in wake form, as shown in Figure 5.17.

Figure 5.18 (b) to Figure 5.18(d) presents the streamlines over the trapezoidal structure. It can be observed as the slope angle increase, the vortex in front of the structure is gradually eliminated. This verifies that with an increasing slope angle $\alpha$, the structure is becoming better aligned with flow patterns. Thus, the trapezoidal structure behaves in a streamwise manner in the boundary layer flow.
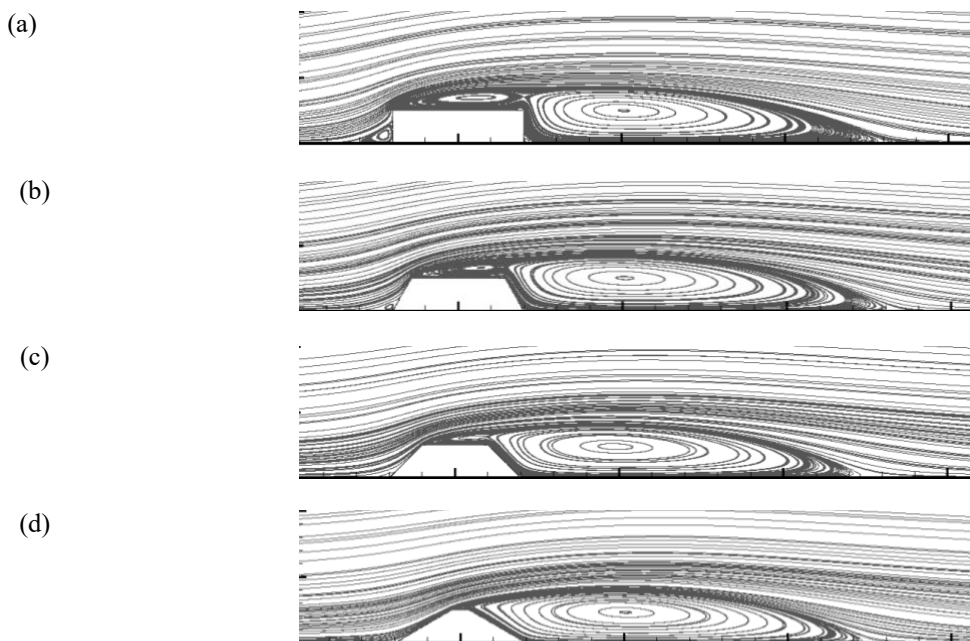
(a)



(b)



(c)



(d)



Figure 5.18: Stream lines for rectangular cylinder with $\alpha = 0°$ at $Re = 1 \times 10^6$ with various boundary layer thicknesses: (a) $\alpha = 0°$ (b) $\alpha = 30°$ and (c) $\alpha = 45°$ (d) $\alpha = 60°$.

# 6 Conclusions and Future works

## 6.1 Conclusion

Numerical studies of the turbulent boundary layer on surface-mounted subsea covers of different geometries have been performed. Two-dimensional RANS equations are solved by $k - \omega\ SST$ turbulence model combining with a wall function

In order to ensure the numerical results are sufficiently independent on the mesh quality, a mesh convergence study has been conducted. The relative difference of drag coefficient $C_d$ and lift coefficient $C_l$ between course, medium and fine mesh are all within a reasonable range. The tests have proved that all solutions achieved sufficient grid resolution.

Furthermore, the validation study is conducted by comparing the horizontal velocity profile obtained in the present study with the experimental data published by Liu et al. The validation study shows a good agreement between the simulation results and the experimental data. This reflects that the RANS $k - \omega\ SST$ model can give an accurate prediction for the hydrodynamic quantities over a wall-mounted structure subjected to a boundary layer flow at high Reynolds number.

Results from simulation have been further discussed. Based on this study and the analysis of results, the following conclusions can be drawn:

1. For trapezoidal structures, the hydrodynamic quantities including both $C_d$ and $C_l$ decrease monotonically as $\alpha$ increases. The viscous effect becomes more significant while the turbulent effect still dominates along as $\alpha$ increases.

2. For a trapezoidal configuration with a smaller angle ranging from $0^\circ$ to $45^\circ$, the drag coefficient increases as the Reynolds number increases. The pressure drag force provides a major contribution to drag force at extremely high Reynolds numbers. However, the frictional drag is still accounted for the total drag force. For geometry with $\alpha = 60^\circ$, the viscous effect is barely visible.

3. The hydrodynamic quantities decrease as the boundary layer thickness increases due to the drop in averaged velocity of flow.

4. The small vortex is generated by block effect from structure, and the large vortex in a wake-form is generated after the flow separation takes place at the sharp front edge of the structure.

## 6.2 Future works

Flows over wall-mounted subsea GRP covers are generally under-investigated. Possible directions for further researches could be considered:

In the present study, various Reynolds numbers and boundary layer thicknesses have been taken into account. However, the focus is limited to a steady-state turbulent flow with the constant free stream velocity. The effect of the wave is negligible in such cases. A further study on flow at the unsteady state can be carried out.

The two-dimensional RANS method with $k - \omega$ SST turbulence model is applied in the simulations. A further study of the 3D vorticity phenomena by other method as URANS or LES may provide a simulation which is closer to the real flow conditions. However, the computational cost would increase dramatically.

Other possibility in the long term include performing an on-bottom stability analysis.

# Reference

Absi R. (2009). A simple eddy viscosity formulation for turbulent boundary layers near smooth walls. *Comptes Rendus Mecanique,* 337: 158-165.

Adams E, Johnston J P. (1988). Effects of the separating shear layer on the reattachment flow structure part 2: Reattachment length and wall shear stress. *Experiments in Fluids,* 6: 493-499.

Akan C. (2012). Surface Mass Transfer in Large Eddy Simulation (LES) of Langmuir Turbulence.

Akoz M S, Kirkgoz M S. (2009). Numerical and Experimental Analyses of the Flow around a Horizontal Wall-Mounted Circular Cylinder. *Transactions of the Canadian Society for Mechanical Engineering,* 33: 29-55.

ARIE M, KIYA M, TAMURA H, KOSUGI M, TAKAOKA K. (1975). Flow over rectangular cylinders immersed in a turbulent boundary layer: Part 2 flow patterns and pressure distributions. *Bulletin of JSME,* 18: 1269-1276.

Brørs B. (1999). Numerical modeling of flow and scour at pipelines. *Journal of hydraulic Engineering,* 125: 511-523.

Cencel Y, Cimbala J. (2006). *Fluid mechanics–fundamentals and applications*.

Cheng A H D, Cheng D T. (2005). Heritage and early history of the boundary element method. *Engineering Analysis with Boundary Elements,* 29: 268-302.

Crabb D, Durao D, Whitelaw J. (1977). *Velocity characteristics in the vicinity of a two-dimensional rib*.

Dai Y, Wang H, Tian C. (2017). *Numerical Simulations of Turbulent Flow Over Two Surface-Mounted Tandem Square Cylinders*.

Fredsoe J, Sumer B. (1997). Hydrodynamics around cylindrical structures. In: World scientific.

Kuijpers A, Nielsen T. (2016). Near-bottom current speed maxima in North Atlantic contourite environments inferred from current-induced bedforms and other seabed evidence. *Marine Geology,* 378: 230-236.

Liu Y, Ke F, Sung H J J J o F, Structures. (2008). Unsteady separated and reattaching turbulent flow over a two-dimensional square rib. 24: 366-381.

McDonald P. (1971). *The computation of transonic flow through two-dimensional gas turbine cascades*. Paper presented at the ASME 1971 International Gas Turbine Conference and Products Show.

Moukalled F, Mangani L, Darwish M. (2016). The finite volume method in computational fluid dynamics. *An advanced introduction with OpenFoam*.

Ong M C, Utnes T, Holmedal L E, Myrhaug D, Pettersen B. (2010). Numerical simulation of flow around a circular cylinder close to a flat seabed at high Reynolds numbers using a k–ε model. *Coastal Engineering,* 57: 931-947.

Patankar S V, Spalding D B. (1983). A calculation procedure for heat, mass and momentum transfer in three-dimensional parabolic flows. In *Numerical Prediction of Flow, Heat Transfer, Turbulence and Combustion* (pp. 54-73): Elsevier.

Pattenden R J, Bressloff N W, Turnock S R, Zhang X. (2007). Unsteady simulations of the flow around a short surface-mounted cylinder. *International journal for numerical methods in fluids,* 53: 895-914.

Pegonen R. (2012). Investigation of thermal mixing using openfoam. In.

Sunden B. (2011). Vortex shedding. *Guide to Thermodynamics*.

Tauqeer M A, Li Z, Ong M C. (2017). Numerical simulation of flow around different wall-mounted structures. *Ships and Offshore Structures,* 12: 1109-1116.

Tritton D J. (1959). Experiments on the flow past a circular cylinder at low Reynolds numbers. *Fluid Mechanics,* 6: 547-567.

Versteeg H, Malalasekera W. (1995). *Computational fluid dynamics*.

Yu H, Wang G, Ma W, Zhang G, Zhao Z. (2019). Research on flow characteristics of aerostatic circular thrust bearing. *Journal of Engineering-Joe,* 2019: 114-118.

# Appendix A  Results

## Appendix A Hydrodynamic Quantities for Various α

| Case | Mesh | α | $C_d$ | Difference | $C_l$ | Difference | $y^+$ wall | $y^+$ bed | $x_R/D$ | Difference |
|------|------|---|-------|------------|-------|------------|-----------|-----------|---------|------------|
| A1 | 57280 | 0 | 0.8477 | | 0.6131 | | 33.5536 | 38.0027 | 15.6600 | |
| A2 | 79840 | 0 | 0.8393 | -0.99% | 0.6123 | -0.13% | 34.8382 | 40.4367 | 15.5700 | -0.57% |
| A3 | 125972 | 0 | 0.8313 | -0.95% | 0.6126 | 0.05% | 35.5669 | 39.1845 | 15.348\0 | -1.43% |
| B1 | 57280 | 30 | 0.8055 | | 0.4344 | | 32.2598 | 30.3071 | 15.8700 | |
| B2 | 79840 | 30 | 0.7996 | -0.74% | 0.4322 | -0.50% | 33.7753 | 32.3192 | 15.9060 | 0.23% |
| B3 | 125972 | 30 | 0.7878 | -1.47% | 0.4347 | 0.58% | 34.6963 | 31.0468 | 15.6240 | -1.77% |
| C1 | 57280 | 45 | 0.7317 | | 0.3307 | | 30.5001 | 33.5814 | 15.3780 | |
| C2 | 79840 | 45 | 0.7292 | -0.34% | 0.3278 | -0.88% | 30.6796 | 39.0339 | 15.4800 | 0.66% |
| C3 | 125972 | 45 | 0.7150 | -1.95% | 0.3385 | 3.28% | 34.6440 | 34.6949 | 14.8500 | -4.07% |
| D1 | 57280 | 60 | 0.6310 | | 0.1930 | | 31.7176 | 39.9577 | 14.7240 | |
| D2 | 79840 | 60 | 0.6284 | -0.41% | 0.1918 | -0.61% | 36.6747 | 41.2286 | 14.7420 | 0.12% |
| D3 | 125972 | 60 | 0.6224 | -0.95% | 0.1896 | -1.15% | 37.7500 | 40.6068 | 14.7540 | 0.08% |

Table A.1: Hydrodynamic quantities for $\alpha = 0°, 30°, 45°, 60°$ at $Re = 1.0 \times 10^6$ with $\delta/D = 0.73$.

| Case | Mesh | α | $C_d$ | Difference | $C_l$ | Difference | $y^+$ $wall$ | $y^+$ $bed$ | $x_R/D$ | Difference |
|------|------|---|-------|------------|-------|------------|-----------|-----------|---------|------------|
| A4 | 72205 | 0 | 0.8552 | | 0.6186 | | 38.4778 | 37.8724 | 15.6540 | |
| A5 | 95410 | 0 | 0.8507 | -0.53% | 0.6204 | 0.31% | 38.5057 | 36.6605 | 15.4860 | -1.07% |
| A6 | 141117 | 0 | 0.8483 | -0.28% | 0.6269 | 1.04% | 38.5627 | 37.3879 | 15.2280 | -1.67% |
| B4 | 72205 | 30 | 0.8083 | | 0.4372 | | 37.6661 | 40.3768 | 15.8700 | |
| B5 | 95410 | 30 | 0.8034 | -0.61% | 0.4392 | 0.46% | 37.7717 | 39.1643 | 15.7260 | -0.91% |
| B6 | 141117 | 30 | 0.7990 | -0.55% | 0.4406 | 0.31% | 30.9994 | 32.9971 | 15.6780 | -0.31% |
| C4 | 72205 | 45 | 0.7319 | | 0.3326 | | 34.5555 | 42.1917 | 15.3780 | |
| C5 | 95410 | 45 | 0.7252 | -0.92% | 0.3336 | 0.31% | 34.9865 | 40.9650 | 15.2760 | -0.66% |
| C6 | 141117 | 45 | 0.7190 | -0.85% | 0.3337 | 0.03% | 35.3154 | 41.3092 | 15.3000 | 0.16% |
| D4 | 72205 | 60 | 0.6285 | | 0.0485 | | 32.0002 | 39.0478 | 14.7240 | |
| D5 | 95410 | 60 | 0.6256 | -0.45% | 0.0483 | -0.37% | 33.8713 | 40.1299 | 14.7240 | 0.00% |
| D6 | 141117 | 60 | 0.6227 | -0.46% | 0.0487 | 0.84% | 32.6059 | 35.2102 | 14.7060 | -0.12% |

Table A.2: Hydrodynamic quantities for $\alpha = 0°, 30°, 45°, 60°$ at $Re = 2.0 \times 10^6$ with $\delta/D = 0.73$.

| Case | Mesh | α | $C_d$ | Difference | $C_l$ | Difference | $y^+$ wall | $y^+$ bed | $x_R/D$ | Difference |
|------|------|---|-------|-----------|-------|-----------|-----------|-----------|---------|-----------|
| A7 | 72205 | 0 | 0.8256 | | 0.6144 | | 35.7539 | 33.0207 | 15.3180 | |
| A8 | 95410 | 0 | 0.8207 | -0.59% | 0.6167 | 0.37% | 35.9554 | 32.0333 | 15.1380 | -1.18 % |
| A9 | 141117 | 0 | 0.8150 | -0.70% | 0.6175 | 0.13% | 41.2839 | 37.3789 | 15.0600 | -0.52 % |
| B7 | 72205 | 30 | 0.7888 | | 0.4365 | | 33.6826 | 34.9675 | 15.6660 | |
| B8 | 95410 | 30 | 0.7835 | -0.68% | 0.4383 | 0.42% | 33.9468 | 33.9243 | 15.5220 | -0.92 % |
| B9 | 141117 | 30 | 0.7798 | -0.47% | 0.4419 | 0.82% | 34.1504 | 34.2924 | 15.3900 | -0.85 % |
| C7 | 72205 | 45 | 0.7199 | | 0.3326 | | 34.1165 | 36.3363 | 15.2760 | |
| C8 | 95410 | 45 | 0.7133 | -0.92% | 0.3337 | 0.32% | 34.6403 | 35.2910 | 15.1740 | -0.67 % |
| C9 | 141117 | 45 | 0.7100 | -0.46% | 0.3404 | 2.00% | 35.3507 | 35.8504 | 14.9220 | -1.66 % |
| D7 | 72205 | 60 | 0.6317 | | 0.0489 | | 33.5603 | 38.6523 | 14.6940 | |
| D8 | 95410 | 60 | 0.6272 | -0.71% | 0.0479 | -1.90% | 34.2363 | 37.4906 | 14.8140 | 0.82 % |
| D9 | 141117 | 60 | 0.6232 | -0.64% | 0.0480 | 0.11% | 35.1653 | 37.7013 | 14.8680 | 0.36 % |

Table A.3: Hydrodynamic quantities for $\alpha = 0°, 30°, 45°, 60°$ at Re $= 0.5 \times 10^6$ with δ/D = 0.73.

| Case | Mesh | α | $C_d$ | Difference | $C_l$ | Difference | $y^+$ wall | $y^+$ bed | $x_R/D$ | Difference |
|------|------|---|-------|-----------|-------|-----------|-----------|-----------|---------|-----------|
| A10 | 57280 | 0 | 0.7478 | | 0.5523 | | 36.6521 | 31.4216 | 15.7800 | |
| A11 | 79840 | 0 | 0.7396 | -1.10% | 0.5500 | -0.42% | 32.9154 | 37.2428 | 15.6600 | -0.76 % |
| A12 | 125972 | 0 | 0.7332 | -0.86% | 0.5495 | -0.09% | 38.9124 | 32.3845 | 15.4200 | -1.53 % |
| B10 | 57280 | 30 | 0.7044 | | 0.3930 | | 32.2355 | 32.4969 | 15.8880 | |
| B11 | 79840 | 30 | 0.6991 | -0.76% | 0.3901 | -0.75% | 33.8555 | 34.6895 | 15.8820 | -0.04 % |
| B12 | 125972 | 30 | 0.6877 | -1.62% | 0.3919 | 0.47% | 34.8059 | 33.2401 | 15.5460 | -2.12 % |
| C10 | 57280 | 45 | 0.6404 | | 0.3054 | | 34.6817 | 32.2254 | 15.1620 | |
| C11 | 79840 | 45 | 0.6344 | -0.93% | 0.2976 | -2.55% | 36.8158 | 31.1566 | 15.3660 | 1.35 % |
| C12 | 125972 | 45 | 0.6210 | -2.12% | 0.3081 | 3.51% | 39.6933 | 33.0693 | 14.6700 | -4.53 % |
| D10 | 57280 | 60 | 0.5519 | | 0.1789 | | 32.1451 | 31.1317 | 14.6160 | |
| D11 | 79840 | 60 | 0.5496 | -0.43% | 0.1768 | -1.18% | 35.8353 | 33.0906 | 14.6340 | 0.12 % |
| D12 | 125972 | 60 | 0.5436 | -1.09% | 0.1738 | -1.69% | 38.3686 | 37.6792 | 14.6460 | 0.08 % |

Table A.4: Hydrodynamic quantities for $\alpha = 0°, 30°, 45°, 60°$ at Re $= 1.0 \times 10^6$ with δ/D = 1.96.

| Case | Mesh | α | $C_d$ | Difference | $C_l$ | Difference | $y^+$ wall | $y^+$ bed | $x_R/D$ | Difference |
|------|------|---|-------|-----------|-------|-----------|-----------|-----------|---------|-----------|
| A13 | 72205 | 0 | 0.7536 | | 0.5565 | | 36.2433 | 34.8225 | 15.7620 | |
| A14 | 95410 | 0 | 0.7496 | -0.53% | 0.5579 | 0.26% | 36.2357 | 33.7148 | 15.5760 | -1.18 % |
| A15 | 141117 | 0 | 0.7462 | -0.44% | 0.5594 | 0.27% | 36.1572 | 34.2562 | 15.4440 | -0.85 % |
| B13 | 72205 | 30 | 0.7060 | | 0.3957 | | 35.8604 | 37.3221 | 15.8460 | |
| B14 | 95410 | 30 | 0.7013 | -0.66% | 0.3972 | 0.38% | 35.9445 | 36.2114 | 15.6780 | -1.06 % |
| B15 | 141117 | 30 | 0.6971 | -0.60% | 0.3974 | 0.04% | 35.8981 | 36.6438 | 15.6240 | -0.34 % |
| C13 | 72205 | 45 | 0.6353 | | 0.3029 | | 33.0664 | 39.1488 | 15.2520 | |
| C14 | 95410 | 45 | 0.6292 | -0.97% | 0.3036 | 0.25% | 32.4215 | 33.1609 | 15.1260 | -0.83 % |
| C15 | 141117 | 45 | 0.6233 | -0.94% | 0.3030 | -0.20% | 33.8389 | 38.3989 | 15.1200 | -0.04 % |
| D13 | 72205 | 60 | 0.5487 | | 0.0449 | | 30.6921 | 36.3795 | 14.5980 | |
| D14 | 95410 | 60 | 0.5459 | -0.50% | 0.0447 | -0.58% | 31.8644 | 35.4413 | 14.5860 | -0.08 % |
| D15 | 141117 | 60 | 0.5436 | -0.42% | 0.0451 | 0.87% | 30.1615 | 34.7096 | 14.5440 | -0.29 % |

Table A.5: Hydrodynamic quantities for $\alpha = 0°, 30°, 45°, 60°$ at $\mathrm{Re} = 2.0 \times 10^6$ with $\delta/D = 1.96$.

| Case | Mesh | α | $C_d$ | Difference | $C_l$ | Difference | $y^+$ wall | $y^+$ bed | $x_R/D$ | Difference |
|------|------|---|-------|-----------|-------|-----------|-----------|-----------|---------|-----------|
| A16 | 72205 | 0 | 0.7253 | | 0.5527 | | 38.6800 | 39.9861 | 15.3900 | |
| A17 | 95410 | 0 | 0.7208 | -0.62% | 0.5541 | 0.25% | 38.8930 | 38.8342 | 15.1980 | -1.25 % |
| A18 | 141117 | 0 | 0.7186 | -0.30% | 0.5544 | 0.05% | 38.7971 | 34.4635 | 15.1440 | -0.36 % |
| B16 | 72205 | 30 | 0.6908 | | 0.3950 | | 36.3832 | 32.3449 | 15.6660 | |
| B17 | 95410 | 30 | 0.6851 | -0.83% | 0.3963 | 0.32% | 32.2081 | 31.3732 | 15.4980 | -1.07 % |
| B18 | 141117 | 30 | 0.6817 | -0.50% | 0.3975 | 0.32% | 36.8583 | 31.6856 | 15.4080 | -0.58 % |
| C16 | 72205 | 45 | 0.6262 | | 0.3028 | | 32.6167 | 33.7181 | 15.1680 | |
| C17 | 95410 | 45 | 0.6204 | -0.92% | 0.3048 | 0.65% | 33.1900 | 32.8346 | 14.9940 | -1.15 % |
| C18 | 141117 | 45 | 0.6150 | -0.88% | 0.3034 | -0.47% | 39.7236 | 33.0044 | 15.0240 | 0.20 % |
| D16 | 72205 | 60 | 0.5507 | | 0.0446 | | 32.0887 | 35.8461 | 14.7000 | |
| D17 | 95410 | 60 | 0.5485 | -0.40% | 0.0444 | -0.42% | 32.8944 | 34.9799 | 14.6880 | -0.08 % |
| D18 | 141117 | 60 | 0.5448 | -0.69% | 0.0442 | -0.37% | 33.7808 | 35.1746 | 14.7360 | 0.33 % |

Table A.6: Hydrodynamic quantities for $\alpha = 0°, 30°, 45°, 60°$ at $\mathrm{Re} = 0.5 \times 10^6$ with $\delta/D = 1.96$.

| Case | Mesh | α | $C_d$ | Difference | $C_l$ | Difference | $y^+$ wall | $y^+$ bed | $x_R/D$ | Difference |
|------|------|---|-------|-----------|-------|-----------|-----------|-----------|---------|-----------|
| A19 | 57280 | 0 | 0.7199 | | 0.5340 | | 39.4697 | 34.2352 | 15.7380 | |
| A20 | 79840 | 0 | 0.7124 | -1.04% | 0.5318 | -0.42% | 41.1044 | 36.5156 | 15.6240 | -0.72 % |
| A21 | 125972 | 0 | 0.7056 | -0.95% | 0.5311 | -0.13% | 33.0054 | 35.2501 | 15.3720 | -1.61 % |
| B19 | 57280 | 30 | 0.6777 | | 0.3804 | | 33.2851 | 33.6708 | 15.8400 | |
| B20 | 79840 | 30 | 0.6726 | -0.75% | 0.3774 | -0.77% | 36.5992 | 38.8337 | 15.8400 | 0.00 % |
| B21 | 125972 | 30 | 0.6611 | -1.71% | 0.3793 | 0.49% | 36.0059 | 34.4247 | 15.4800 | -2.27 % |
| C19 | 57280 | 45 | 0.6142 | | 0.2925 | | 33.9769 | 31.4435 | 15.2460 | |
| C20 | 79840 | 45 | 0.6092 | -0.81% | 0.2883 | -1.43% | 33.3542 | 36.4978 | 15.3000 | 0.35 % |
| C21 | 125972 | 45 | 0.5933 | -2.62% | 0.2925 | 1.45% | 38.8529 | 32.0809 | 14.8440 | -2.98 % |
| D19 | 57280 | 60 | 0.5300 | | 0.1739 | | 31.7341 | 36.4816 | 14.5620 | |
| D20 | 79840 | 60 | 0.5271 | -0.55% | 0.1721 | -1.04% | 30.8030 | 35.5916 | 14.5620 | 0.00 % |
| D21 | 125972 | 60 | 0.5226 | -0.86% | 0.1696 | -1.42% | 37.8794 | 37.0311 | 14.5500 | -0.08 % |

Table A.7: Hydrodynamic quantities for $\alpha = 0°, 30°, 45°, 60°$ at Re $= 1.0 \times 10^6$ with δ/D = 2.52.

| Case | Mesh | α | $C_d$ | Difference | $C_l$ | Difference | $y^+$ wall | $y^+$ bed | $x_R/D$ | Difference |
|------|------|---|-------|-----------|-------|-----------|-----------|-----------|---------|-----------|
| A22 | 72205 | 0 | 0.7259 | | 0.5382 | | 35.6785 | 34.1308 | 15.7260 | |
| A23 | 95410 | 0 | 0.7220 | -0.54% | 0.5397 | 0.28% | 35.6669 | 33.0527 | 15.5280 | -1.26 % |
| A24 | 141117 | 0 | 0.7187 | -0.46% | 0.5408 | 0.19% | 35.5632 | 33.5648 | 15.4200 | -0.70 % |
| B22 | 72205 | 30 | 0.6788 | | 0.3831 | | 35.3532 | 36.6166 | 15.7800 | |
| B23 | 95410 | 30 | 0.6743 | -0.68% | 0.3844 | 0.32% | 35.4262 | 35.5232 | 15.6240 | -0.99 % |
| B24 | 141117 | 30 | 0.6704 | -0.58% | 0.3851 | 0.18% | 35.3900 | 35.9793 | 15.5460 | -0.50 % |
| C22 | 72205 | 45 | 0.6353 | | 0.3029 | | 32.6111 | 38.4367 | 15.1800 | |
| C23 | 95410 | 45 | 0.6292 | -0.97% | 0.3036 | 0.25% | 33.0424 | 37.3592 | 15.0480 | -0.87 % |
| C24 | 141117 | 45 | 0.6233 | -0.94% | 0.3030 | -0.20% | 33.3776 | 37.7156 | 15.0420 | -0.04 % |
| D22 | 72205 | 60 | 0.5270 | | 0.0437 | | 30.2541 | 35.7310 | 14.5380 | |
| D23 | 95410 | 60 | 0.5244 | -0.49% | 0.0434 | -0.55% | 32.0436 | 36.8105 | 14.5320 | -0.04 % |
| D24 | 141117 | 60 | 0.5209 | -0.68% | 0.0433 | -0.39% | 32.8338 | 37.1497 | 14.5800 | 0.33 % |

Table A.8: Hydrodynamic quantities for $\alpha = 0°, 30°, 45°, 60°$ at Re $= 2.0 \times 10^6$ with δ/D = 2.52.

| Case | Mesh | α | $C_d$ | Difference | $C_l$ | Difference | $y^+$ wall | $y^+$ bed | $x_R/D$ | Difference |
|------|------|---|-------|-----------|-------|-----------|-----------|-----------|---------|-----------|
| A25 | 72205 | 0 | 0.6998 | | 0.5347 | | 37.9544 | 34.4679 | 15.3660 | |
| A26 | 95410 | 0 | 0.6956 | -0.61% | 0.5361 | 0.26% | 38.1524 | 33.4620 | 15.1740 | -1.25 % |
| A27 | 141117 | 0 | 0.6920 | -0.51% | 0.5365 | 0.08% | 38.1957 | 33.8165 | 15.0780 | -0.63 % |
| B25 | 72205 | 30 | 0.6643 | | 0.3824 | | 35.8545 | 31.7297 | 15.6120 | |
| B26 | 95410 | 30 | 0.6592 | -0.77% | 0.3836 | 0.33% | 36.1386 | 30.7900 | 15.4440 | -1.08 % |
| B27 | 141117 | 30 | 0.6554 | -0.57% | 0.3861 | 0.65% | 31.9058 | 31.1476 | 15.2760 | -1.09 % |
| C25 | 72205 | 45 | 0.6022 | | 0.2935 | | 38.0088 | 33.1034 | 15.1140 | |
| C26 | 95410 | 45 | 0.5962 | -1.01% | 0.2943 | 0.30% | 38.6356 | 32.1896 | 14.9760 | -0.91 % |
| C27 | 141117 | 45 | 0.5952 | -0.17% | 0.3015 | 2.45% | 40.0029 | 32.9979 | 14.4600 | -3.45 % |
| D25 | 72205 | 60 | 0.5294 | | 0.0434 | | 31.6626 | 35.2258 | 14.6220 | |
| D26 | 95410 | 60 | 0.5271 | -0.43% | 0.0432 | -0.54% | 32.4463 | 34.3697 | 14.6220 | 0.00 % |
| D27 | 141117 | 60 | 0.5234 | -0.70% | 0.0430 | -0.44% | 33.3156 | 34.5573 | 14.6700 | 0.33 % |

Table A.9: Hydrodynamic quantities for $\alpha = 0°, 30°, 45°, 60°$ at $Re = 0.5 \times 10^6$ with $\delta/D = 2.52$.

# Appendix B  Convergence
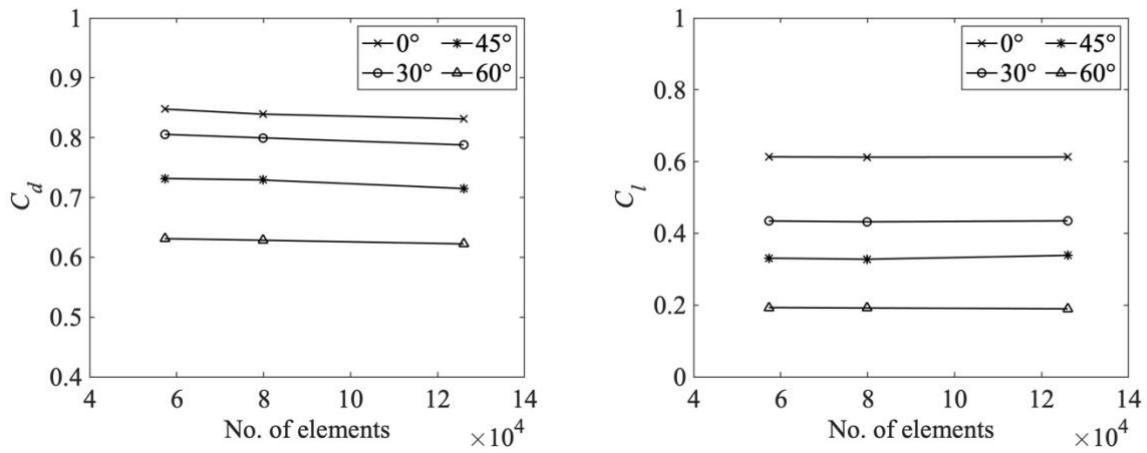


Figure A.1: Mesh Convergence with respect to hydrodynamic coefficients $C_d$ (left) and $C_l$ (right) at $Re = 1.0 \times 10^6$ with $\delta/D = 0.73$.
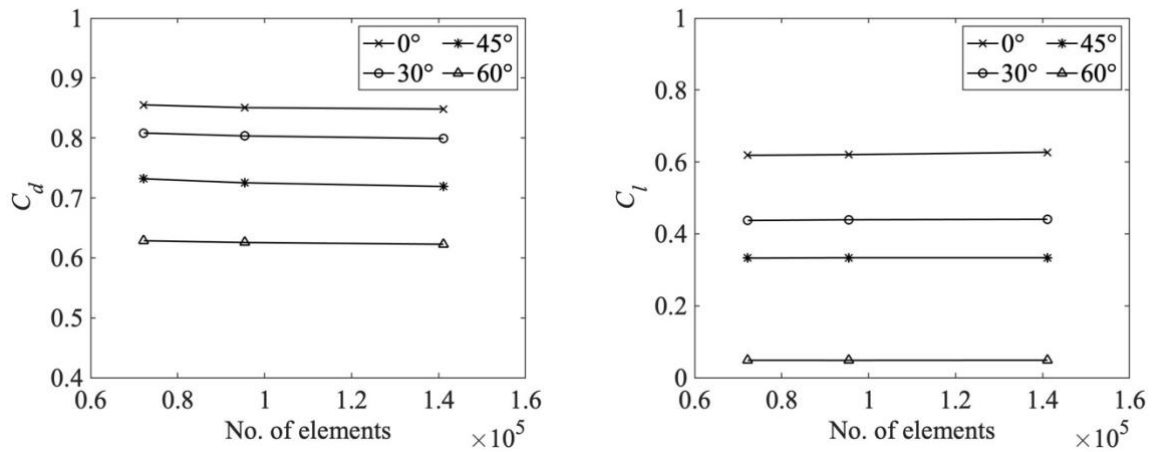


Figure A.2: Mesh Convergence with respect to hydrodynamic coefficients $C_d$ (left) and $C_l$ (right) at $Re = 2.0 \times 10^6$ with $\delta/D = 0.73$.
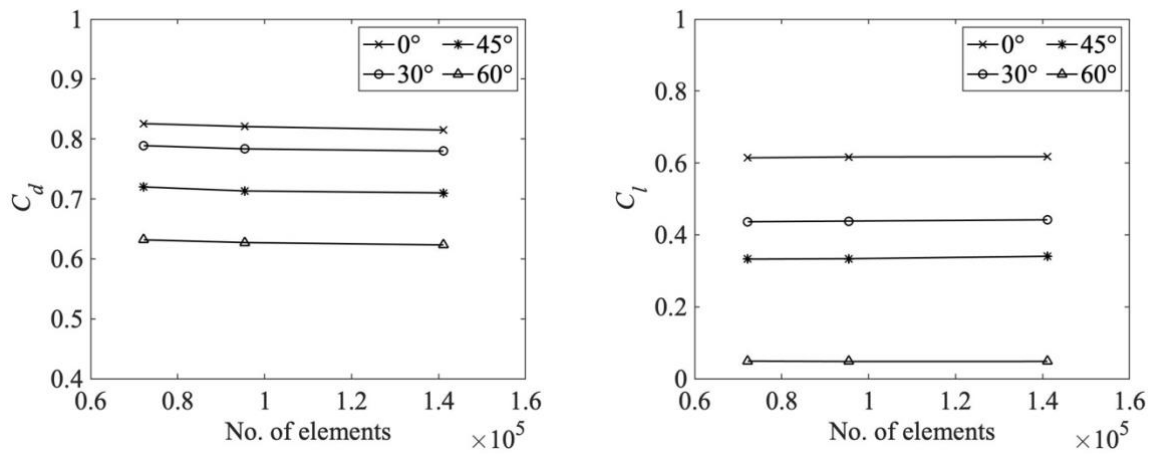
Figure A.3: Mesh Convergence with respect to hydrodynamic coefficients $C_d$ (left) and $C_l$ (right) at $\mathrm{Re} = 0.5 \times 10^6$ with $\delta/D = 0.73$.
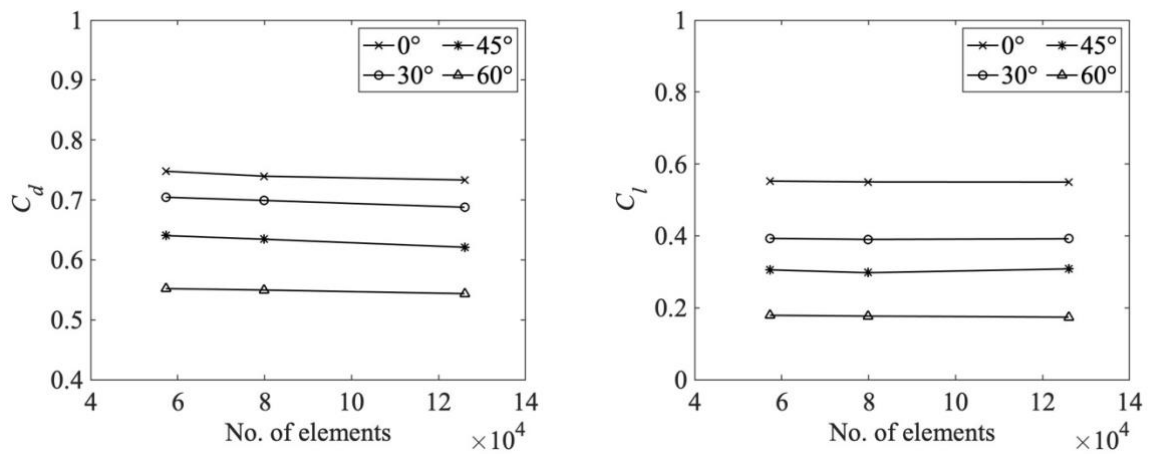


Figure A.4: Mesh Convergence with respect to hydrodynamic coefficients $C_d$ (left) and $C_l$ (right) at $\mathrm{Re} = 1.0 \times 10^6$ with $\delta/D = 1.96$.
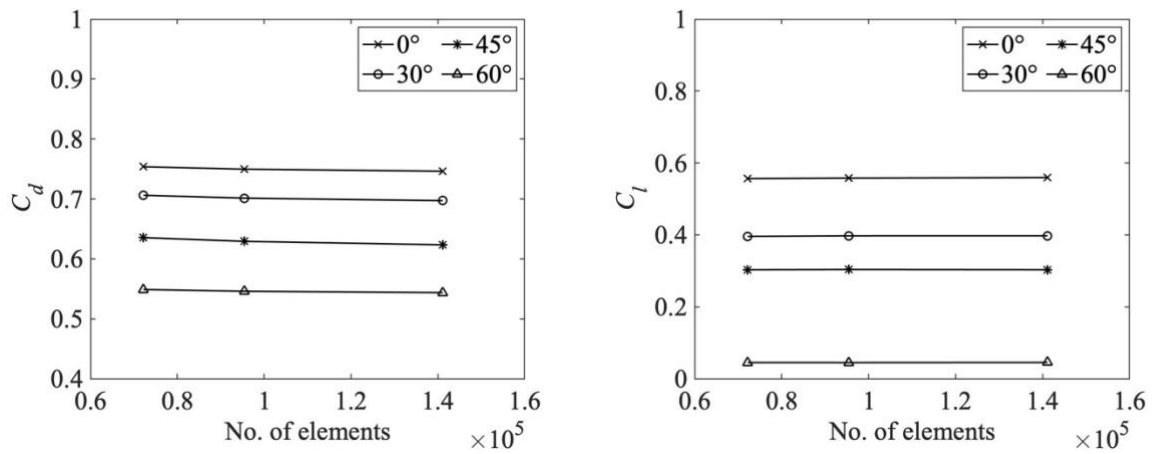
Figure A.5: Mesh Convergence with respect to hydrodynamic coefficients $C_d$ (left) and $C_l$ (right) at $\mathrm{Re} = 2.0 \times 10^6$ with $\delta/D = 1.96$.
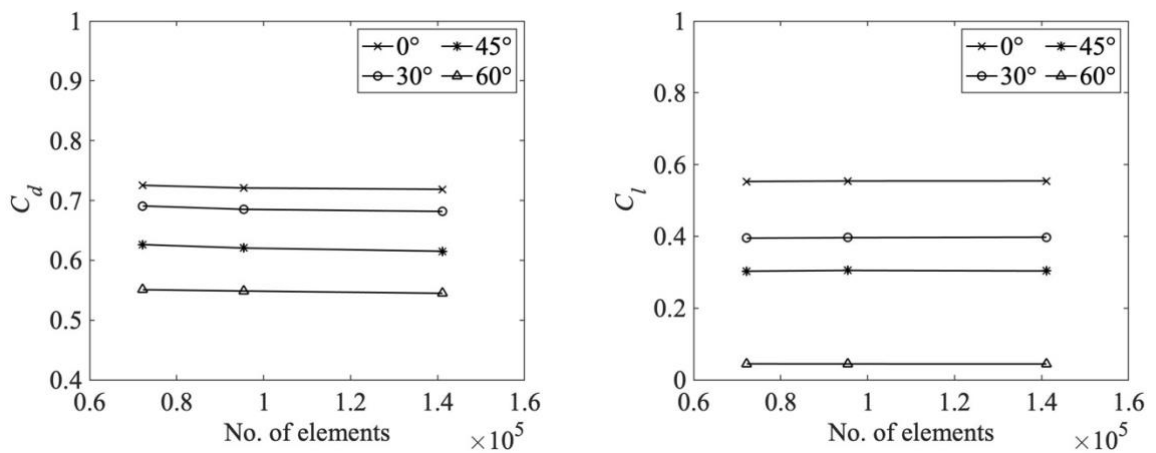


Figure A.6: Mesh Convergence with respect to hydrodynamic coefficients $C_d$ (left) and $C_l$ (right) at $\mathrm{Re} = 0.5 \times 10^6$ with $\delta/D = 1.96$.
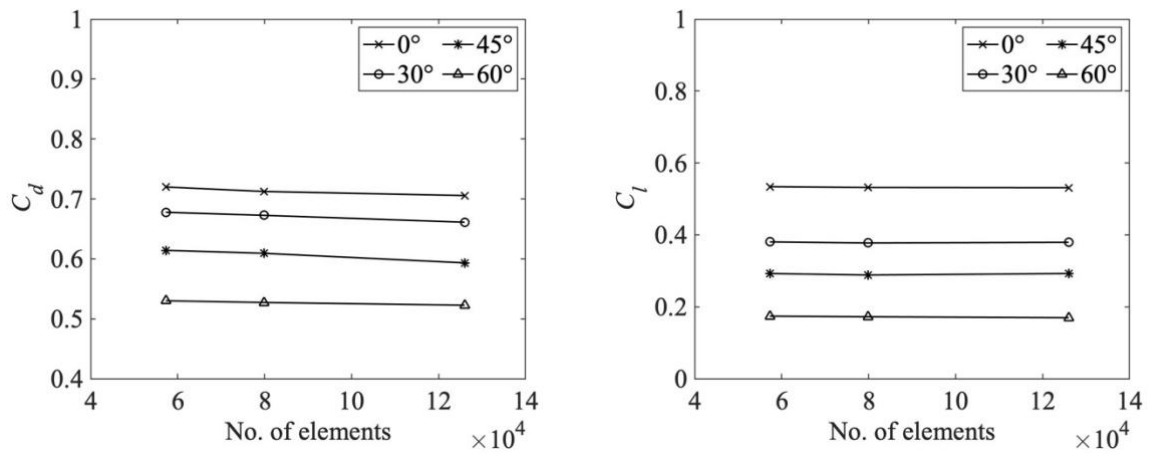
Figure A.7: Mesh Convergence with respect to hydrodynamic coefficients $C_d$ (left) and $C_l$ (right) at $\text{Re} = 1.0 \times 10^6$ with $\delta/D = 2.52$.
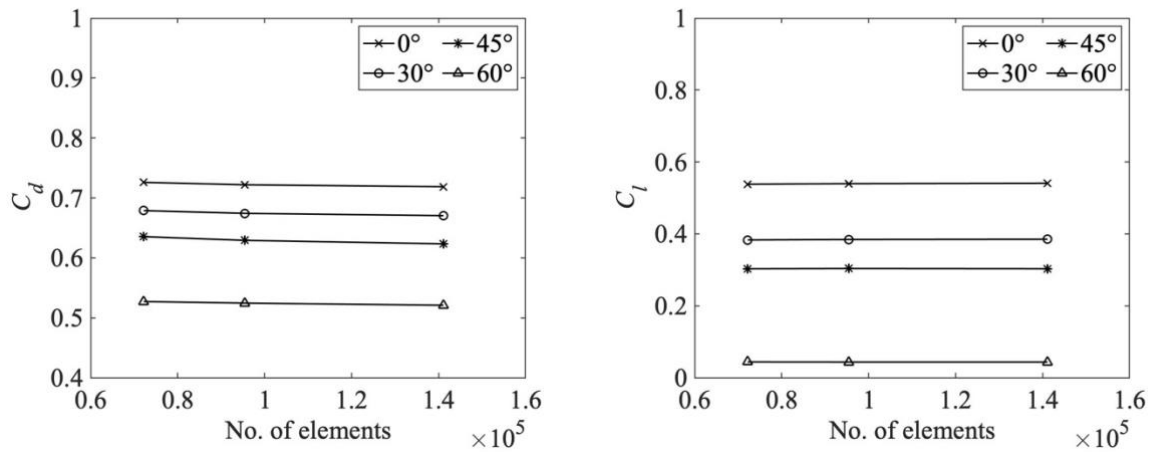


Figure A.8: Mesh Convergence with respect to hydrodynamic coefficients $C_d$ (left) and $C_l$ (right) at $\text{Re} = 2.0 \times 10^6$ with $\delta/D = 2.52$.
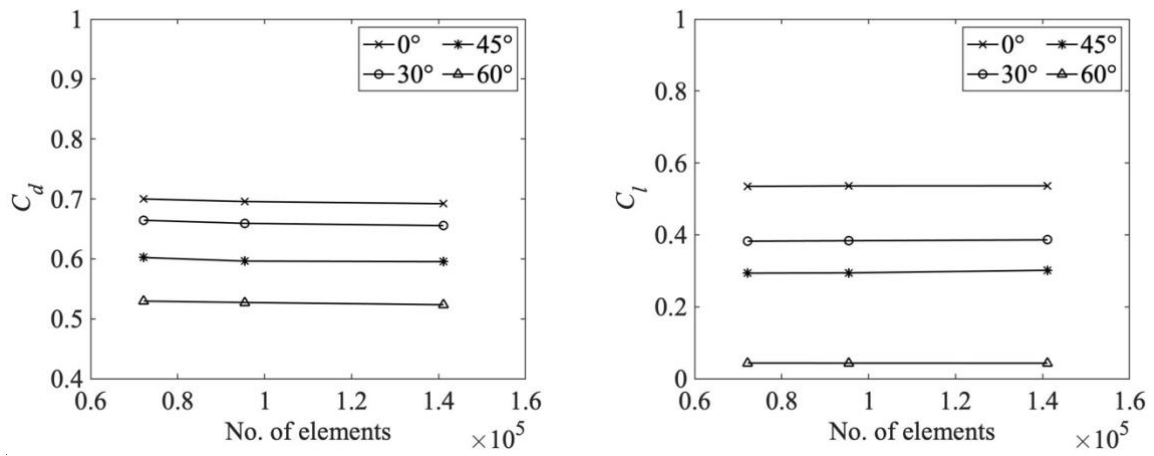
Figure A.9: Mesh Convergence with respect to hydrodynamic coefficients $C_d$ (left) and $C_l$ (right) at $\text{Re} = 0.5 \times 10^6$ with $\delta/D = 2.52$.

# Appendix C  Effect of α on hydrodynamic coefficient
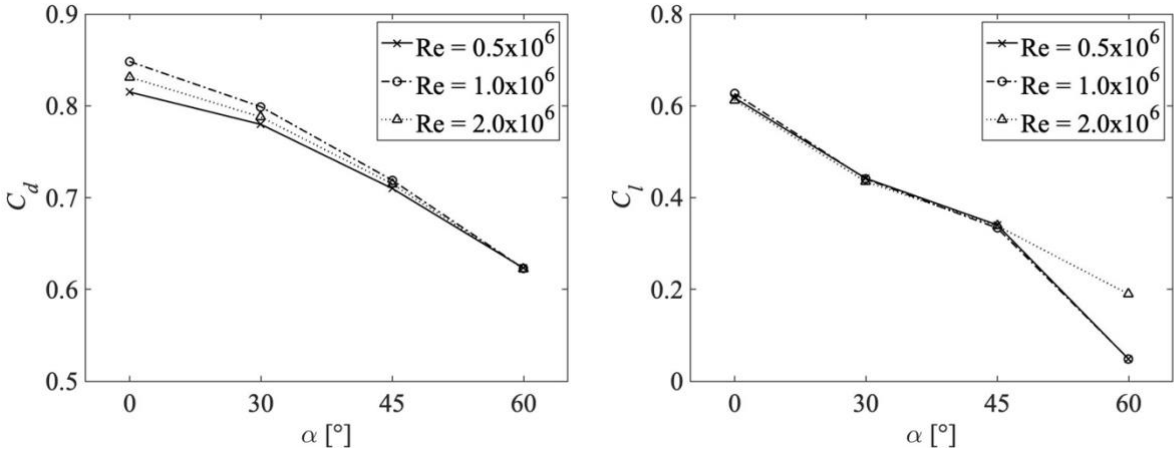


Figure A.10: Variation of Hydrodynamic coefficients with respect to different α with different boundary layer thickness $\delta/D = 0.73$.
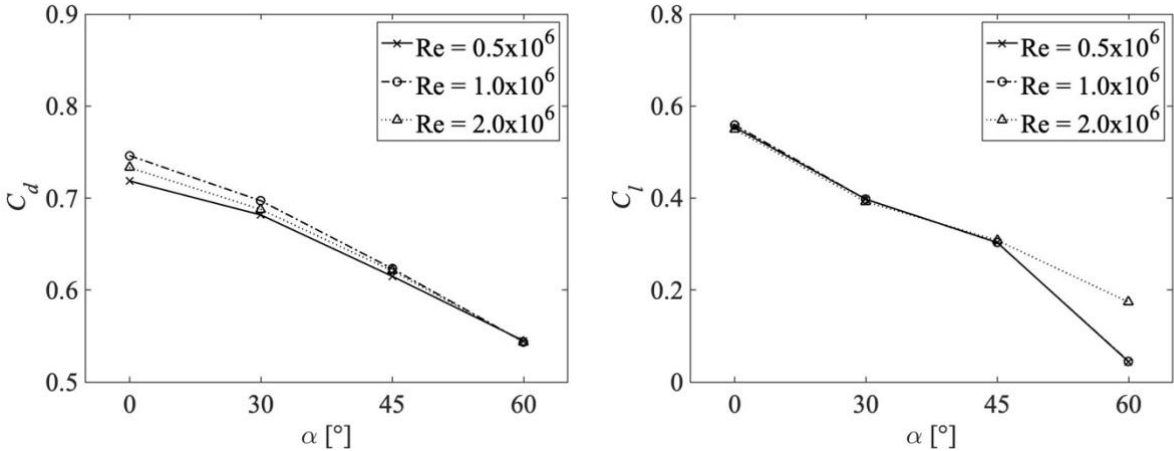


Figure A.11: Variation of Hydrodynamic coefficients with respect to different α with different boundary layer thickness $\delta/D = 1.96$.
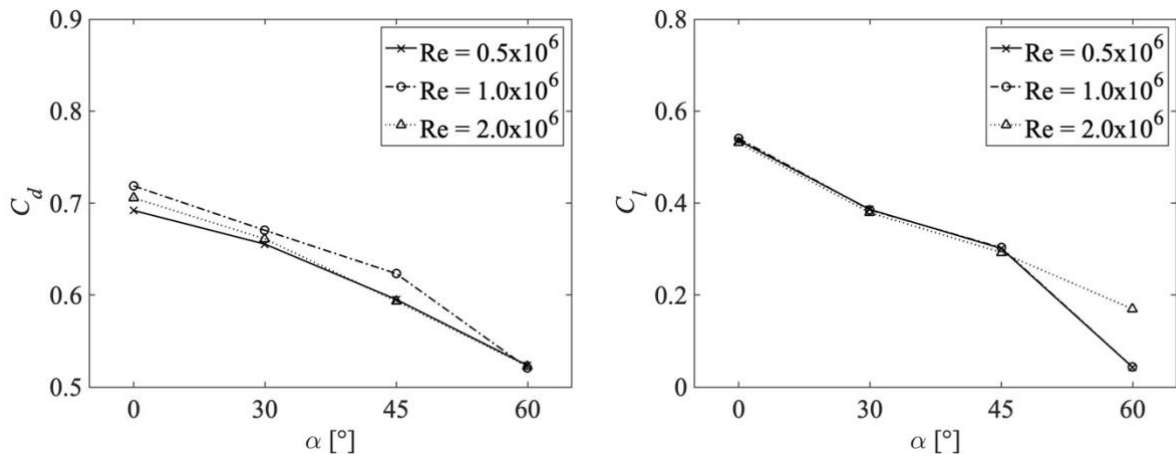
Figure A.12: Variation of Hydrodynamic coefficients with respect to different α with different boundary layer thickness δ/D = 2.52.

# Appendix D  Effect of $\delta/D$ on hydrodynamic coefficients
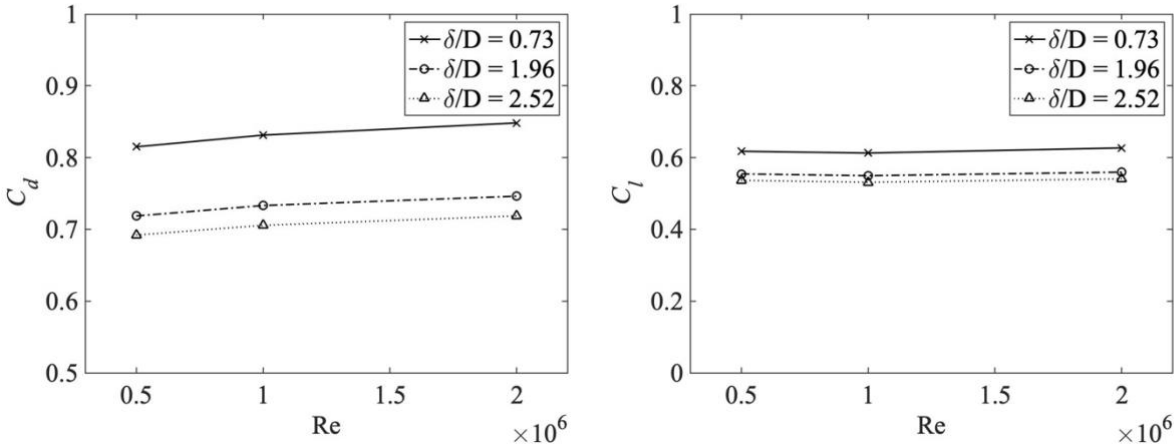


Figure A.13: Variation of Hydrodynamic coefficients with respect to different Reynolds numbers for angles of slope $\alpha = 0°$ with different boundary layer thicknesses $\delta/D = 0.73, \delta/D = 1.96$ and $\delta/D = 2.52$.
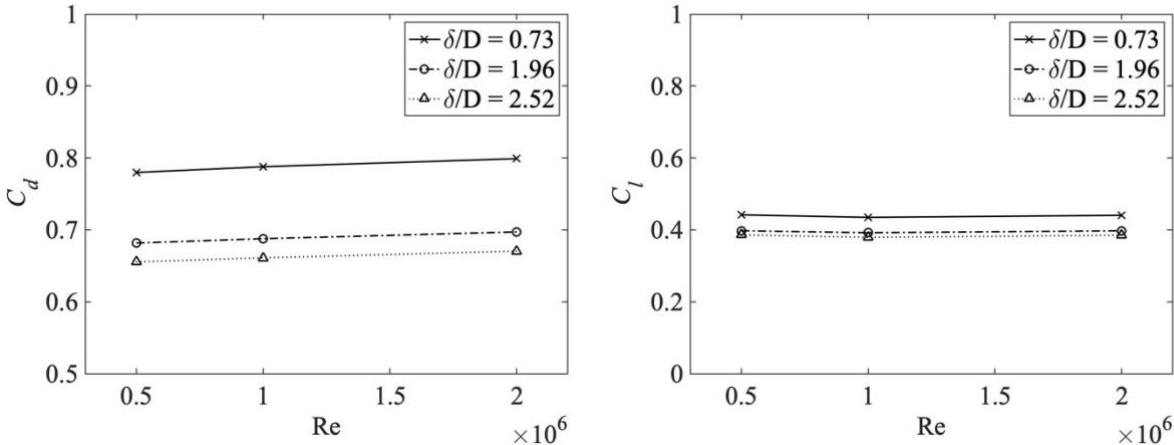


Figure A.14: Variation of Hydrodynamic coefficients with respect to different Reynolds numbers for angles of slope $\alpha = 30°$ with different boundary layer thicknesses $\delta/D = 0.73, \delta/D = 1.96$ and $\delta/D = 2.52$.
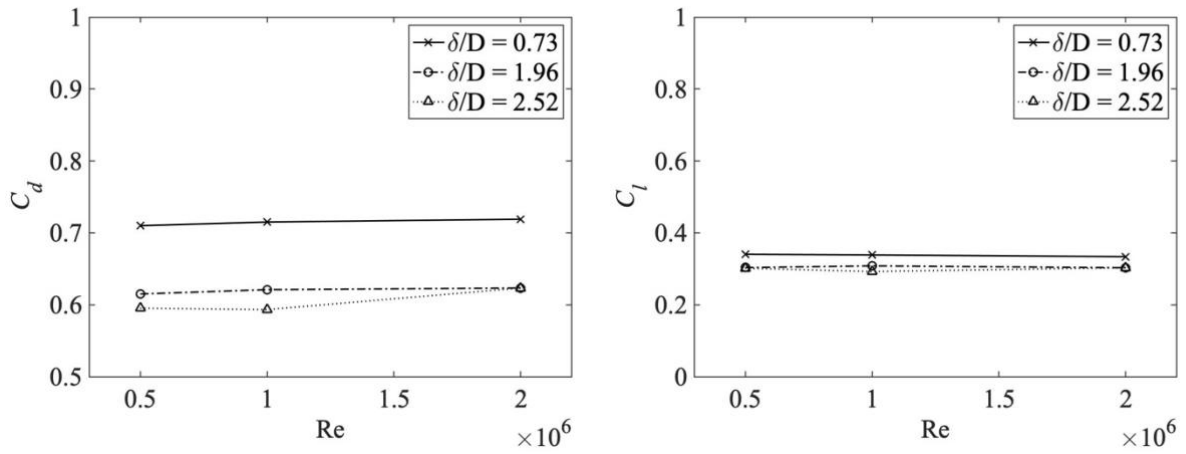
Figure A.15: Variation of Hydrodynamic coefficients with respect to different Reynolds numbers for angles of slope $\alpha = 45°$ with different boundary layer thicknesses $\delta/D = 0.73$, $\delta/D = 1.96$ and $\delta/D = 2.52$.
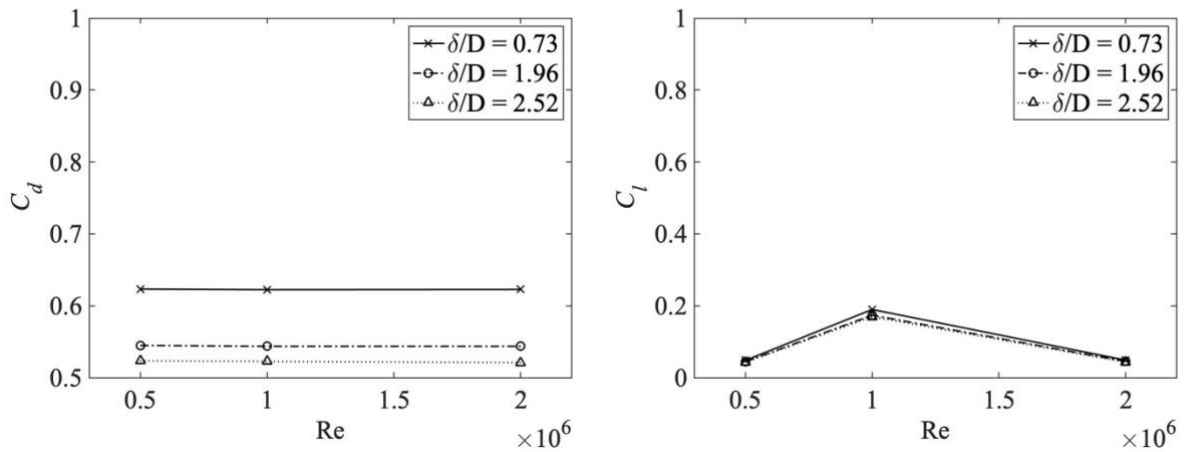


Figure A.16: Variation of Hydrodynamic coefficients with respect to different Reynolds numbers for angles of slope $\alpha = 60°$ with different boundary layer thicknesses $\delta/D = 0.73$, $\delta/D = 1.96$ and $\delta/D = 2.52$.

# Appendix E  Velocity Field
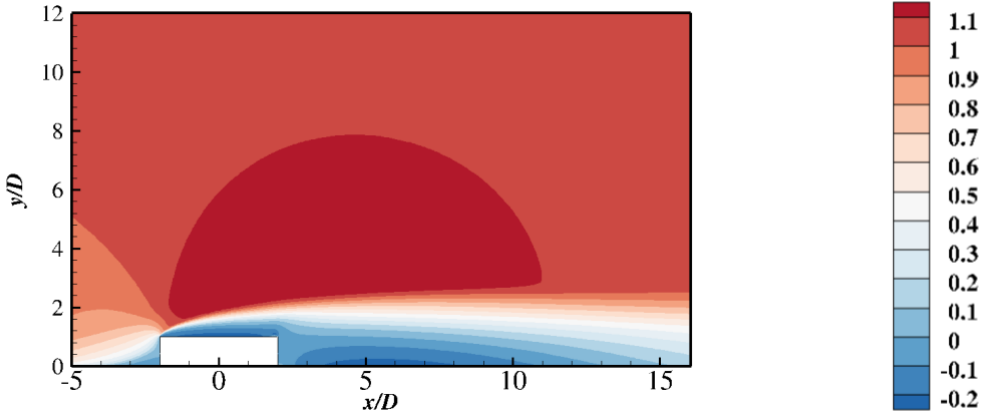


(a)
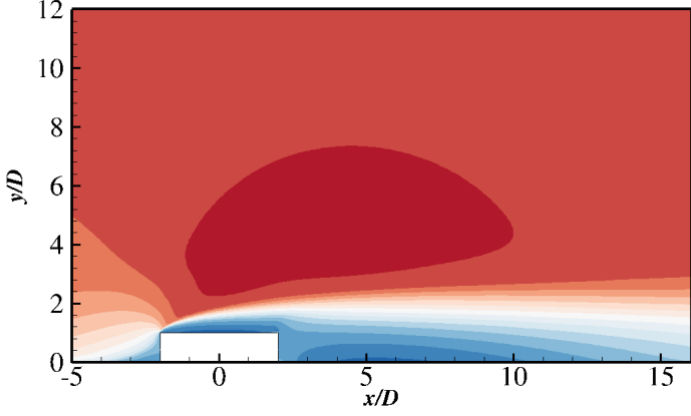


(b)
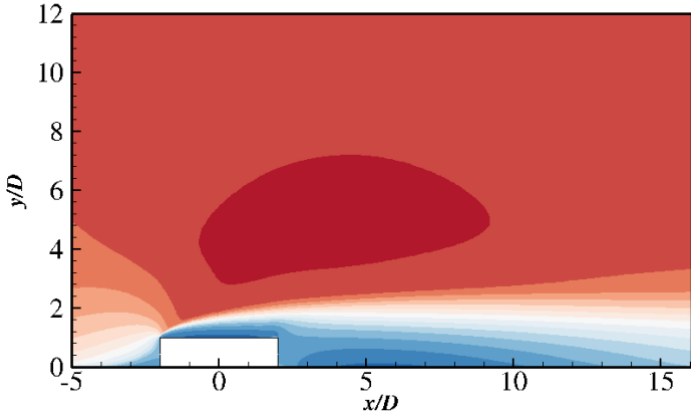


(c)

Figure A.17: Velocity contour for rectangular cylinder with $\alpha = 0^\circ$ immersed at $Re = 1 \times 10^6$ with various boundary layer thicknesses (a) $\delta/D = 0.73$, (b) $\delta/D = 1.96$ and (c) $\delta/D = 2.52$.
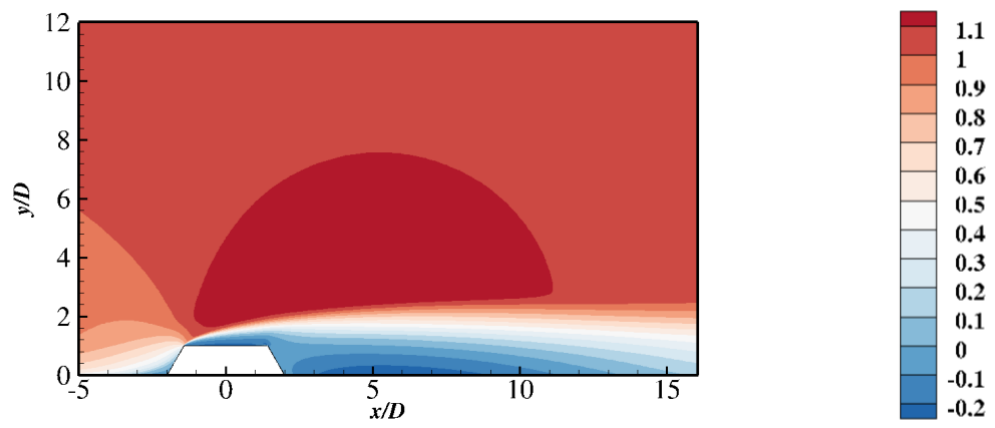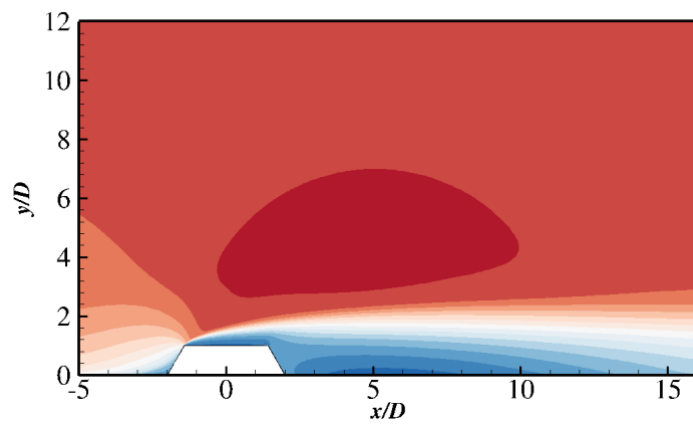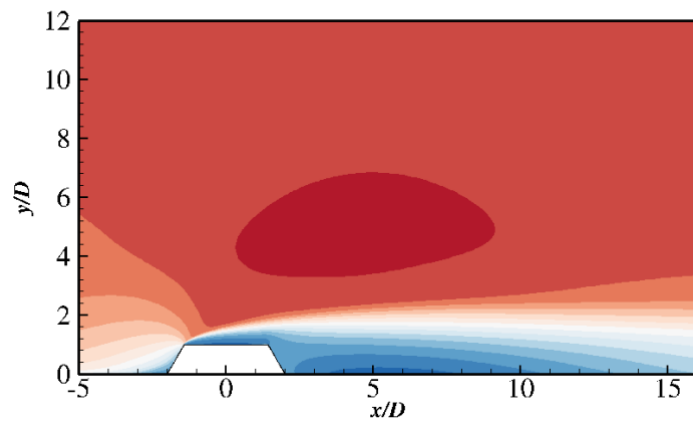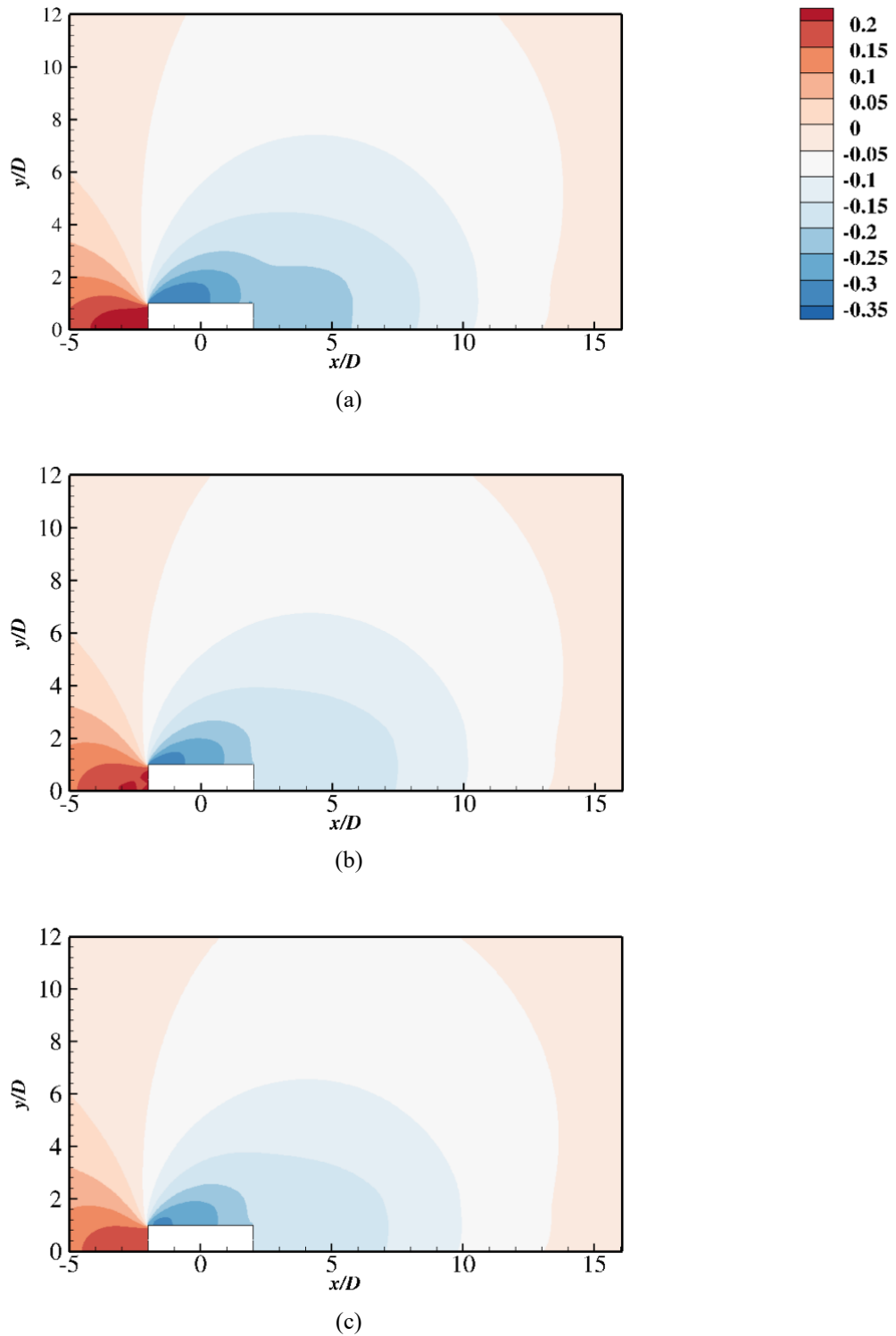
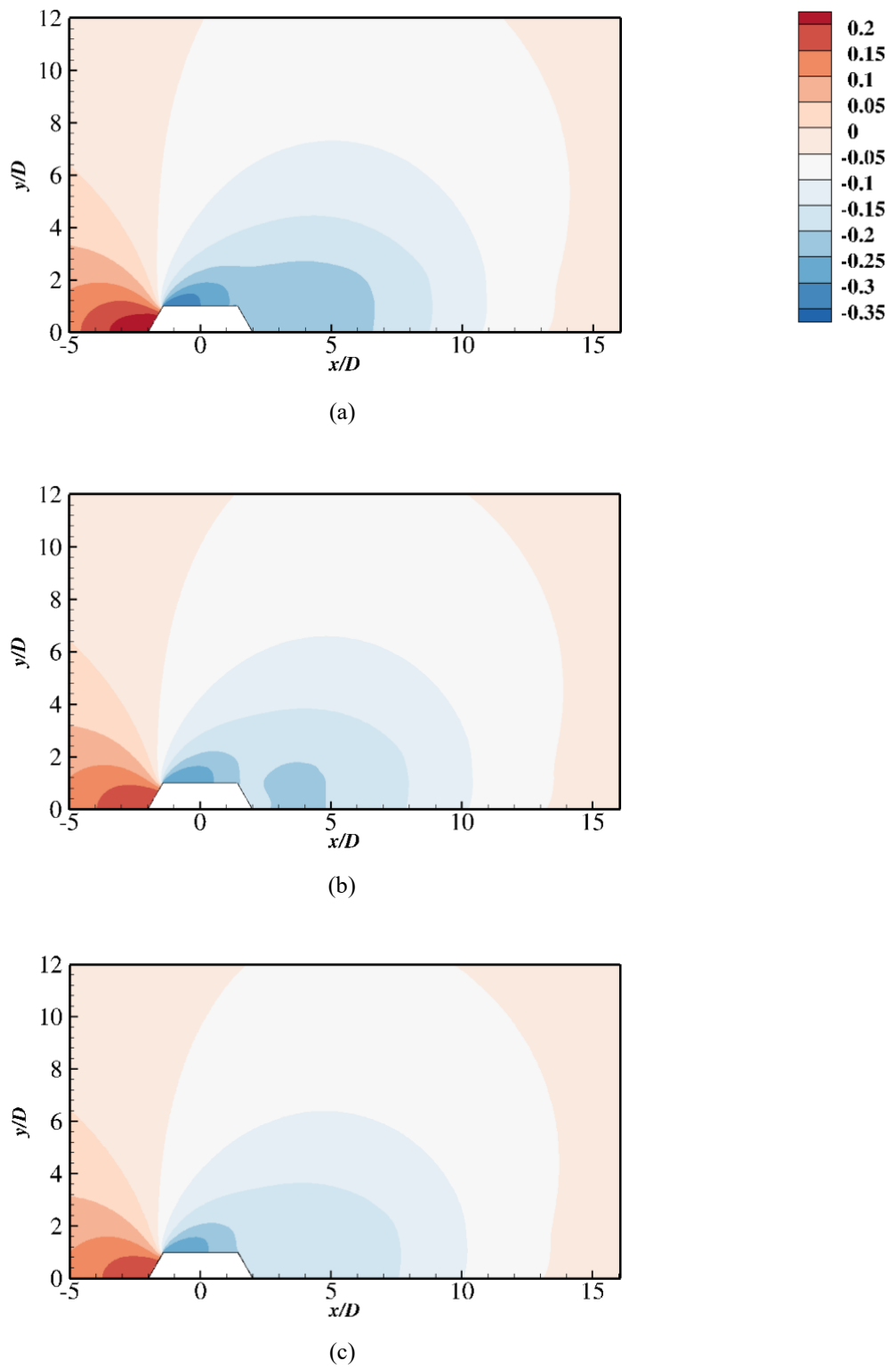Figure A.18: Velocity contour for trapezoidal cylinder with $\alpha = 30°$ immersed at $\mathrm{Re} = 1.0 \times 10^6$ with various boundary layer thicknesses (a) $\delta/D = 0.73$, (b) $\delta/D = 1.96$ and (c) $\delta/D = 2.52$.
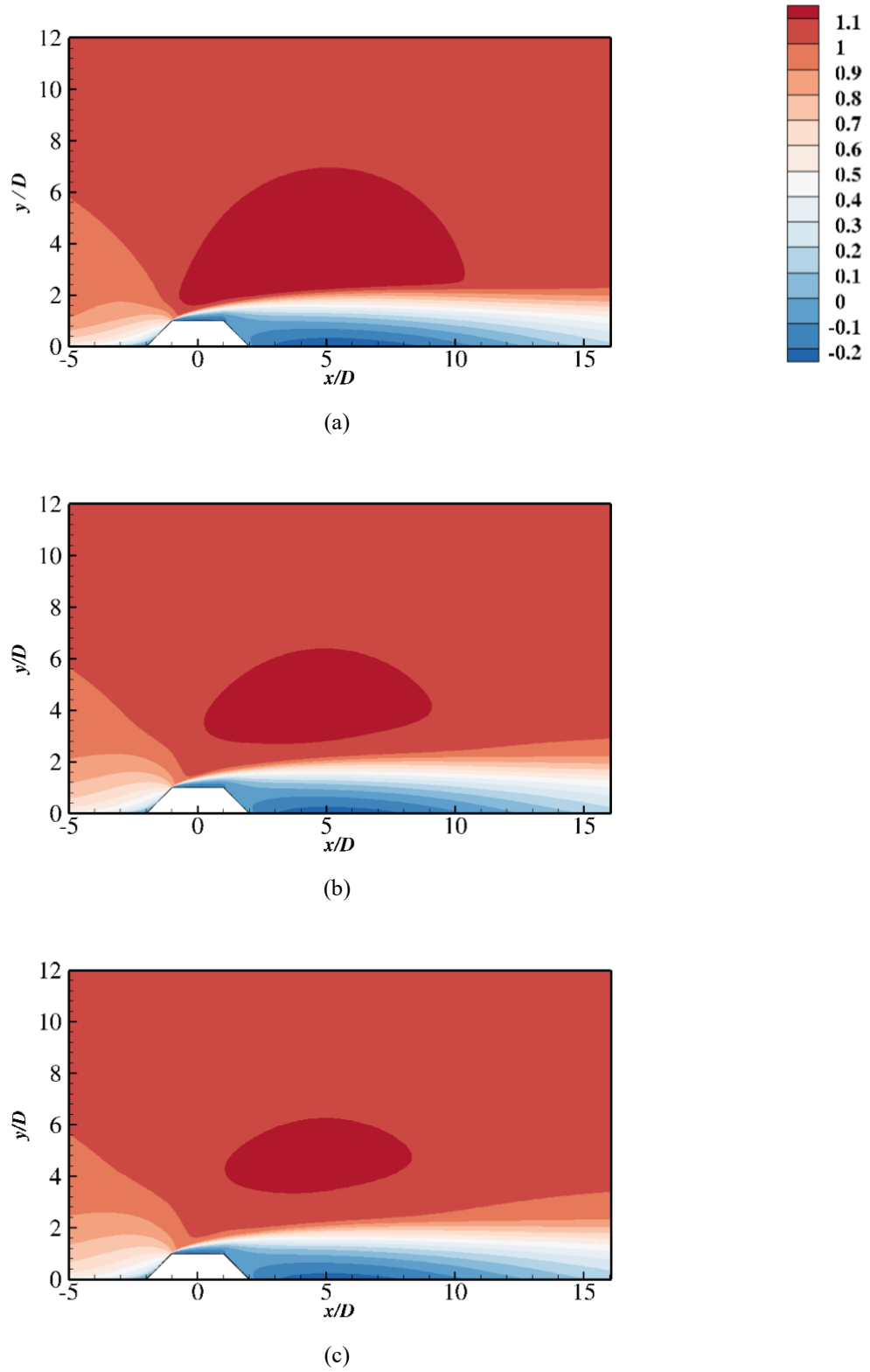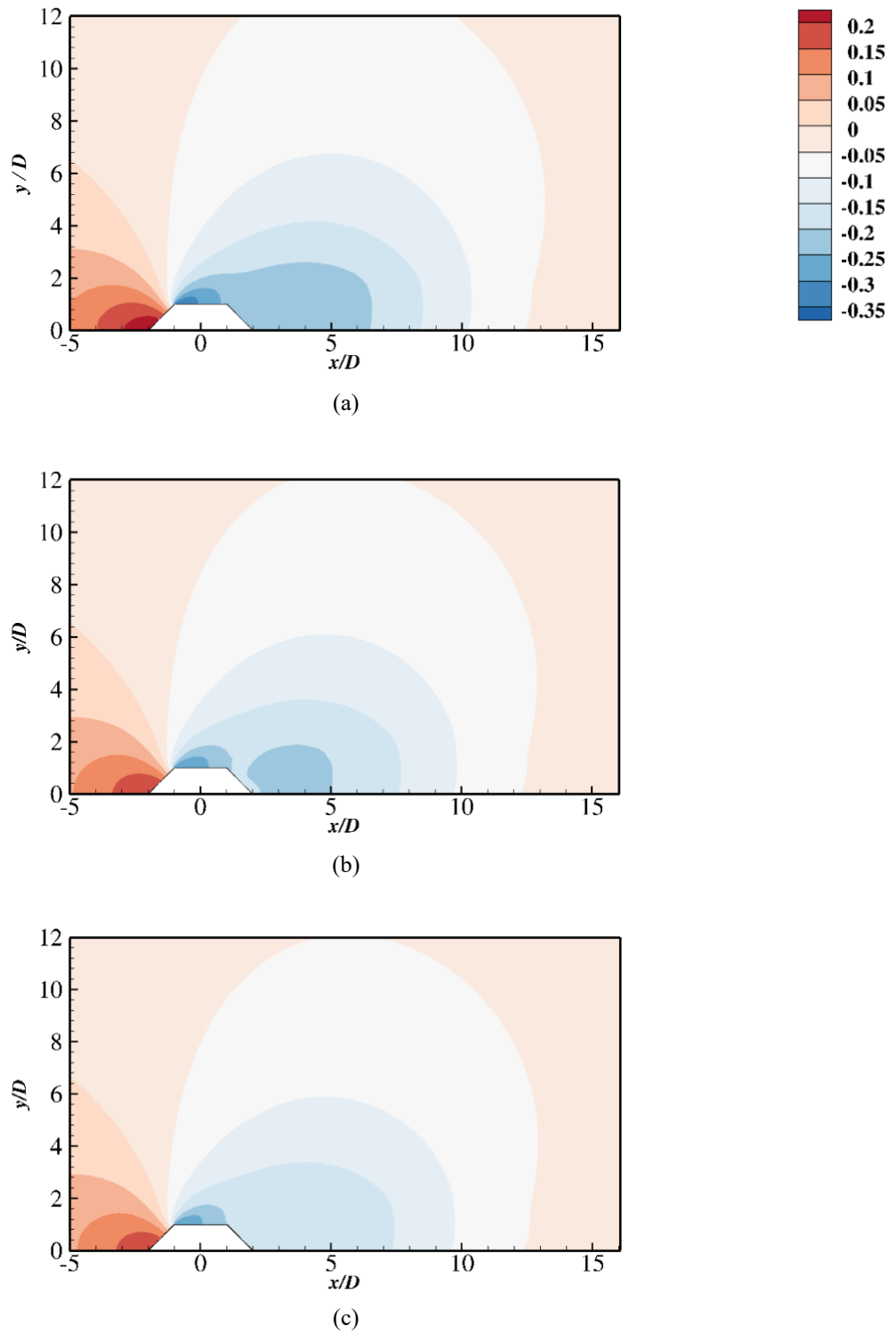
Figure A.19: Velocity contour for trapezoidal cylinder with $\alpha = 45^\circ$ immersed at Re $= 1.0 \times 10^6$ with various boundary layer thicknesses (a) $\delta/D = 0.73$, (b) $\delta/D = 1.96$ and (c) $\delta/D = 2.52$.

(a)



(b)



(c)
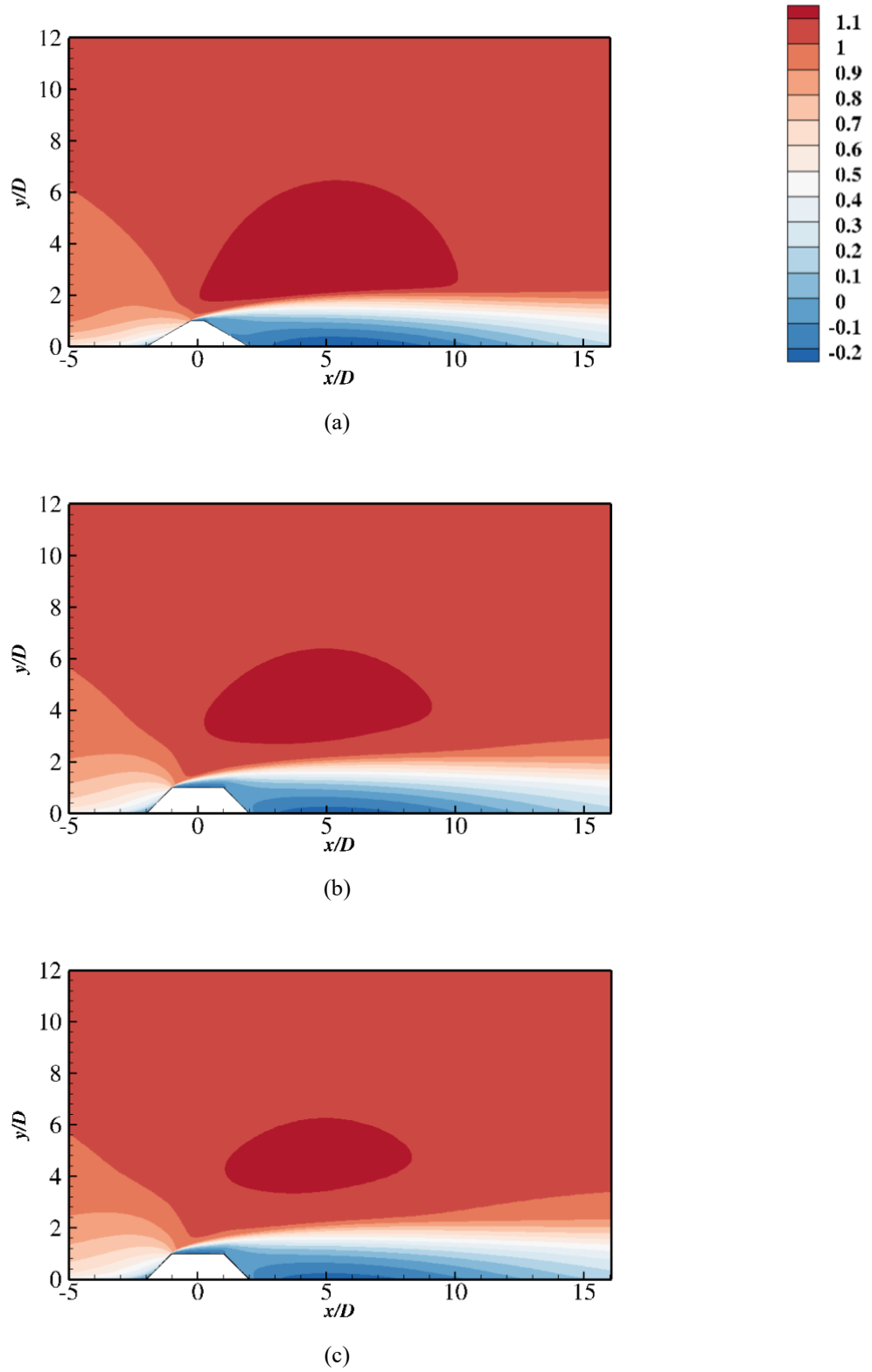
Figure A.20: Velocity contour for trapezoidal cylinder with $\alpha = 60°$ immersed at $Re = 1.0 \times 10^6$ with various boudary layer thicknesses (a) $\delta/D = 0.73$, (b) $\delta/D = 1.96$ and (c) $\delta/D = 2.52$.
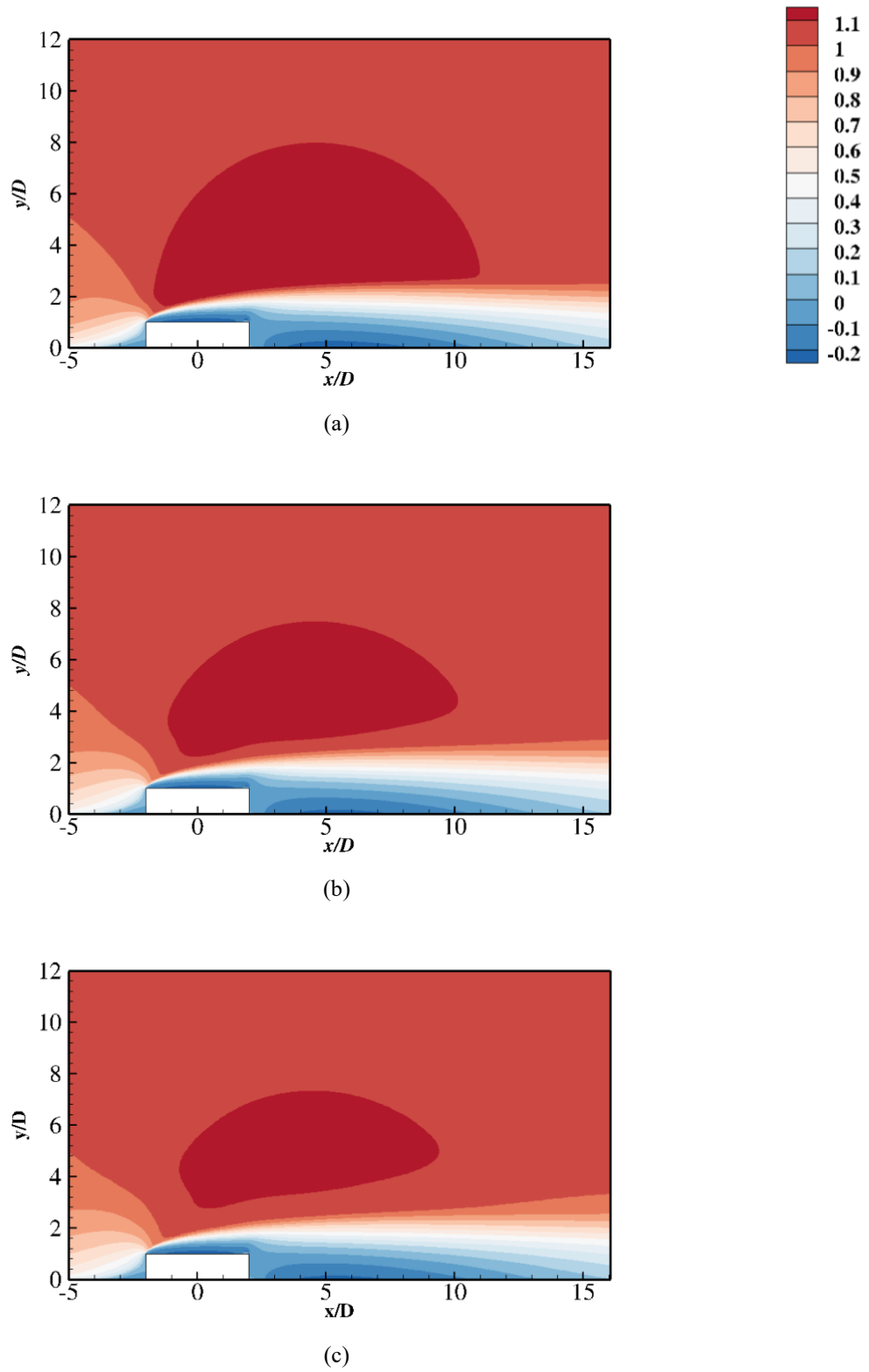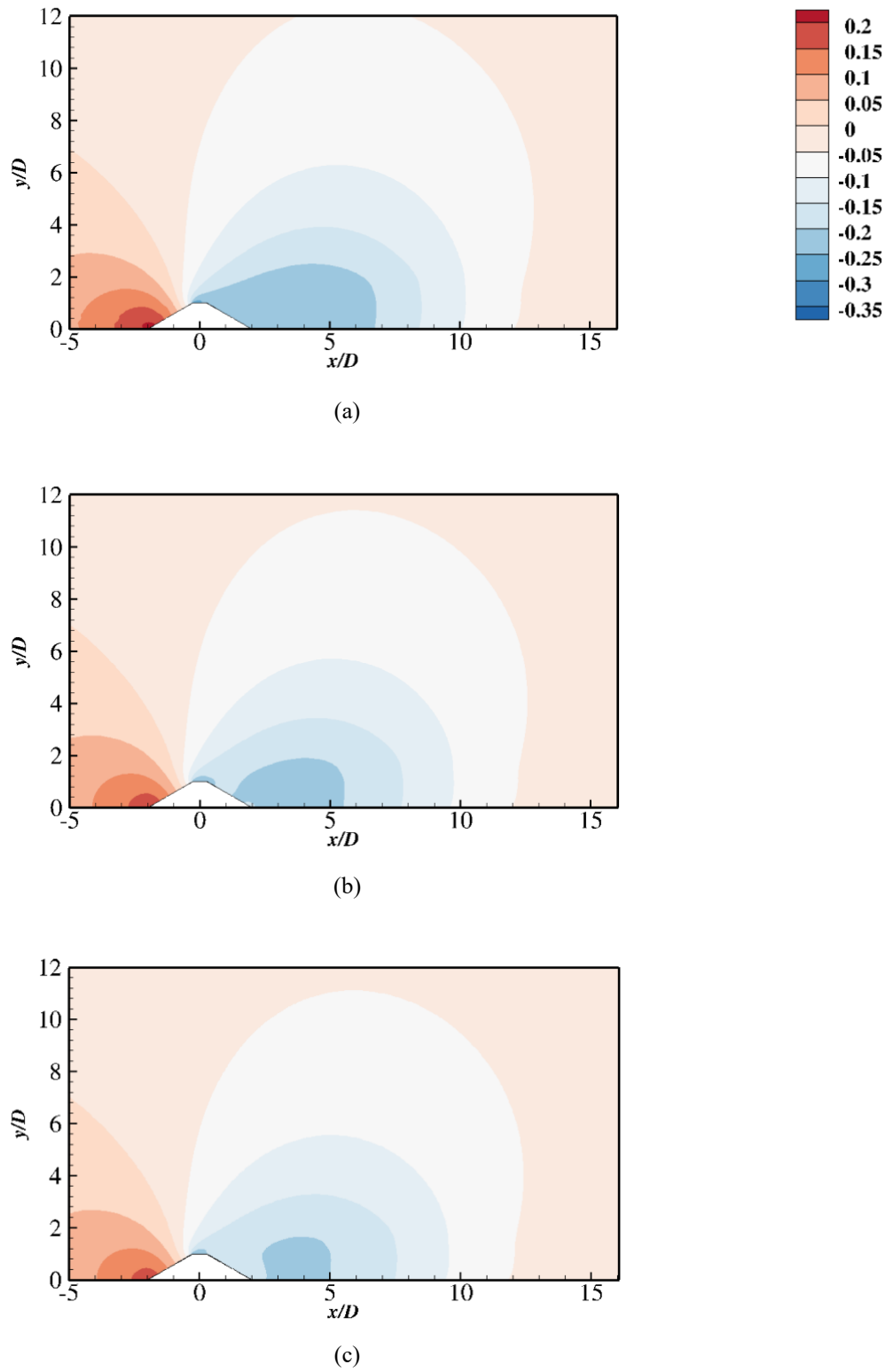
Figure A.21: Velocity contour for rectangular cylinder with $\alpha = 0^{\circ}$ immersed at $Re = 2.0 \times 10^{6}$ with various boundary layer thicknesses (a) $\delta/D = 0.73$, (b) $\delta/D = 1.96$ and (c) $\delta/D = 2.52$.
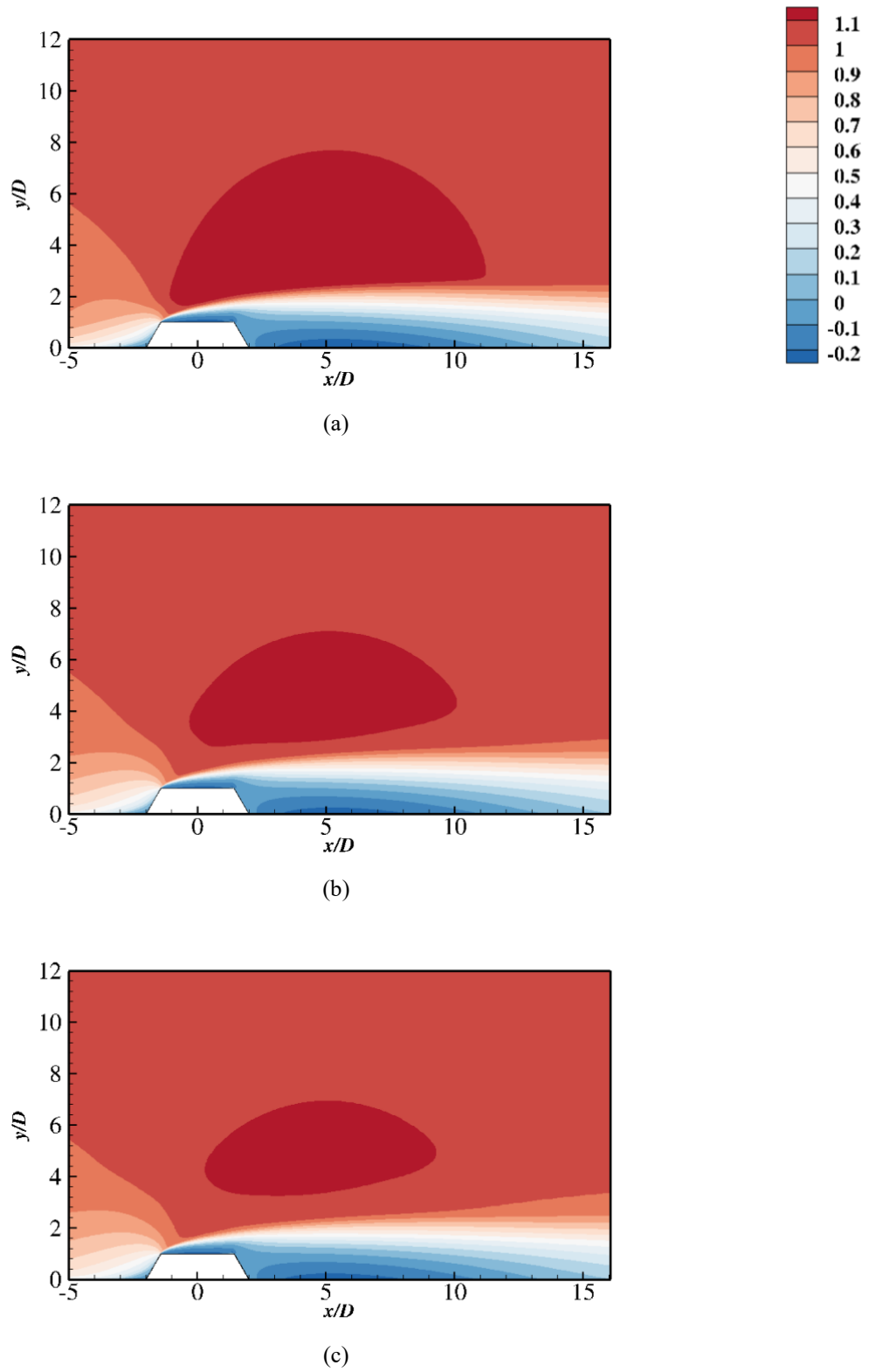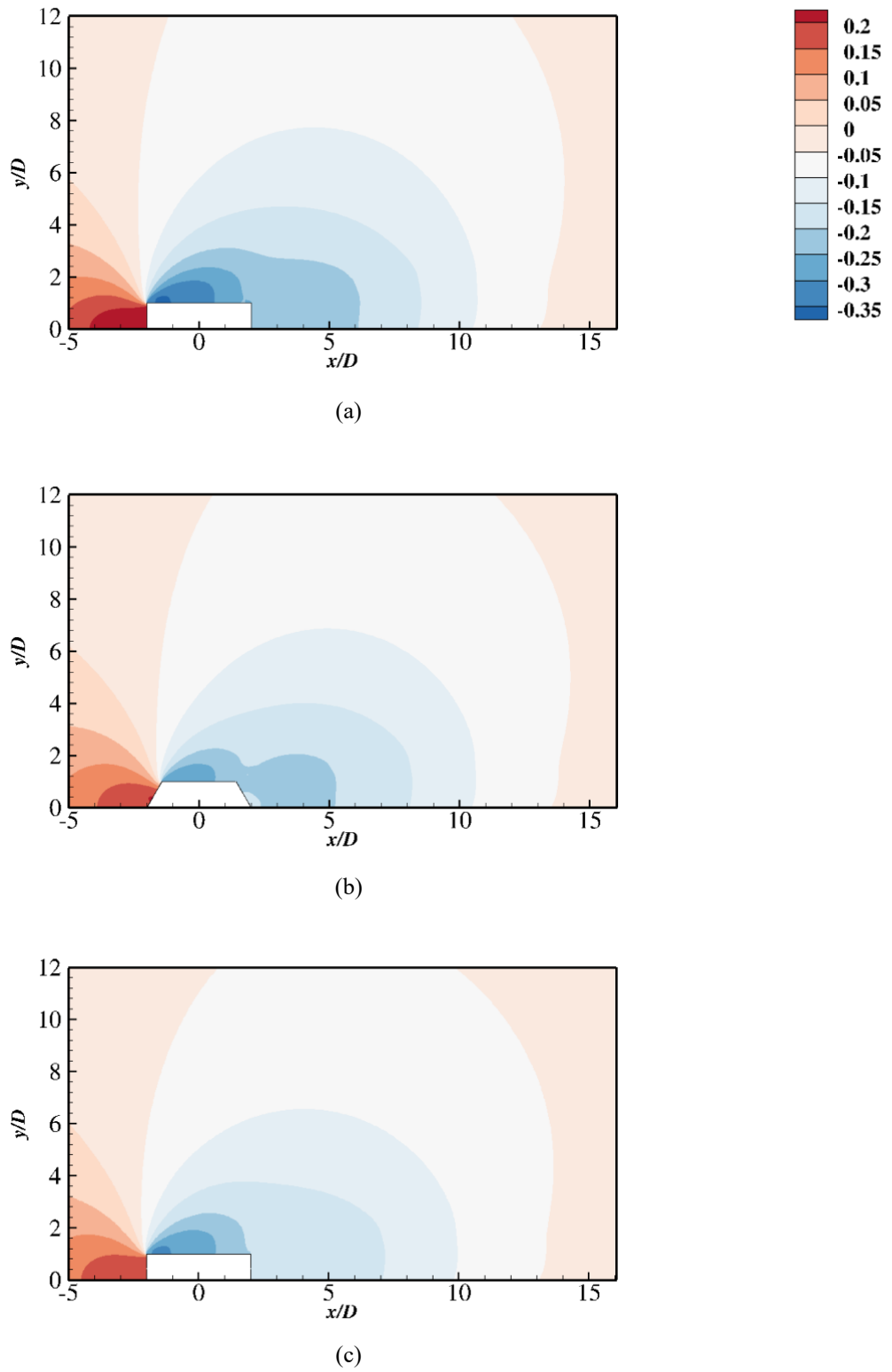
Figure A.22: Velocity contour for trapezoidal cylinder with $\alpha = 30°$ immersed at $Re = 2.0 \times 10^6$ with various boundary layer thicknesses (a) $\delta/D = 0.73$, (b) $\delta/D = 1.96$ and (c) $\delta/D = 2.52$.
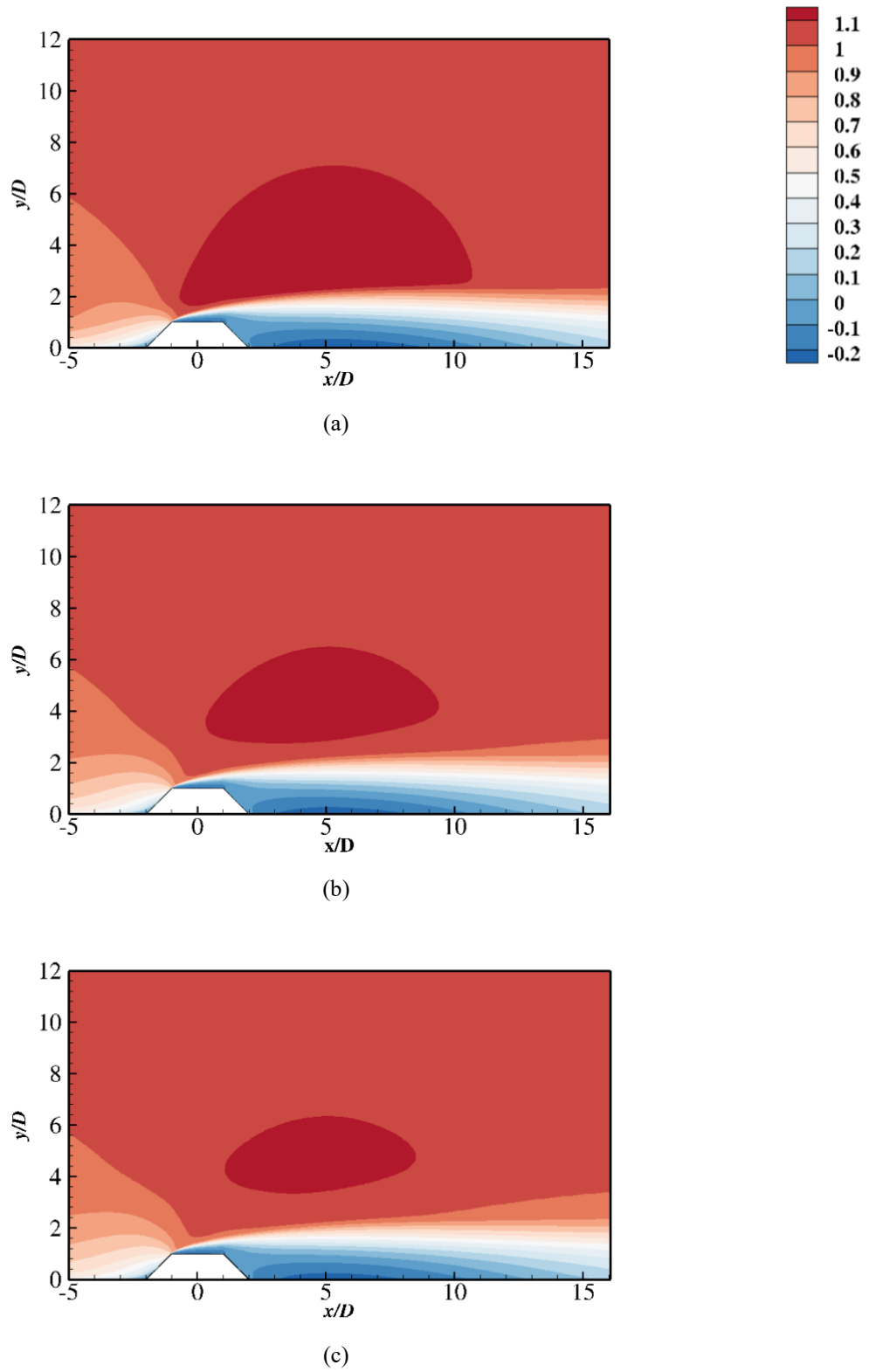
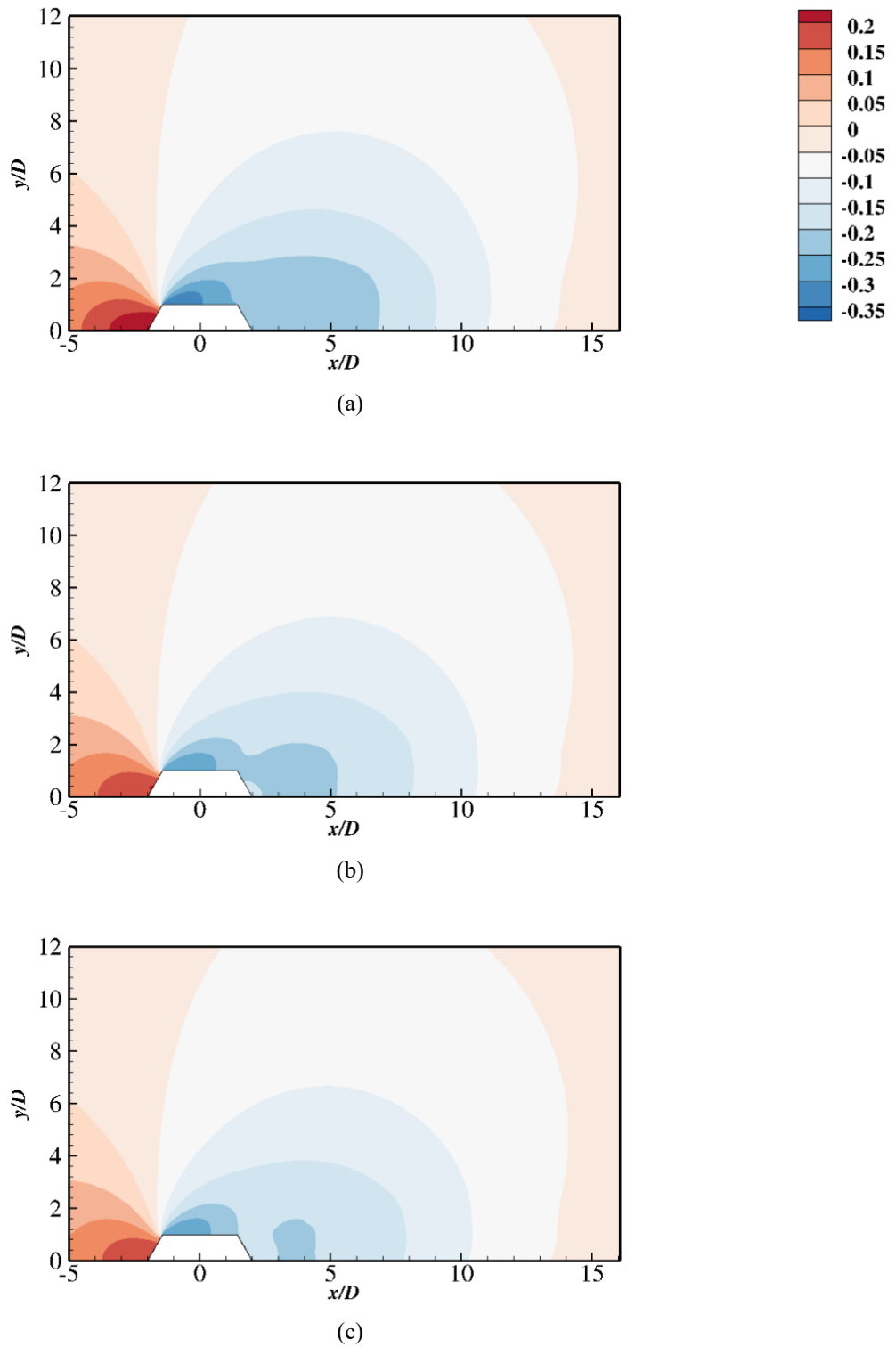Figure A.23: Velocity contour for trapezoidal cylinder with $\alpha = 45°$ immersed at $Re = 2.0 \times 10^6$ with various boundary layer thicknesses (a) $\delta/D = 0.73$, (b) $\delta/D = 1.96$ and (c) $\delta/D = 2.52$.

(a)



(b)



(c)
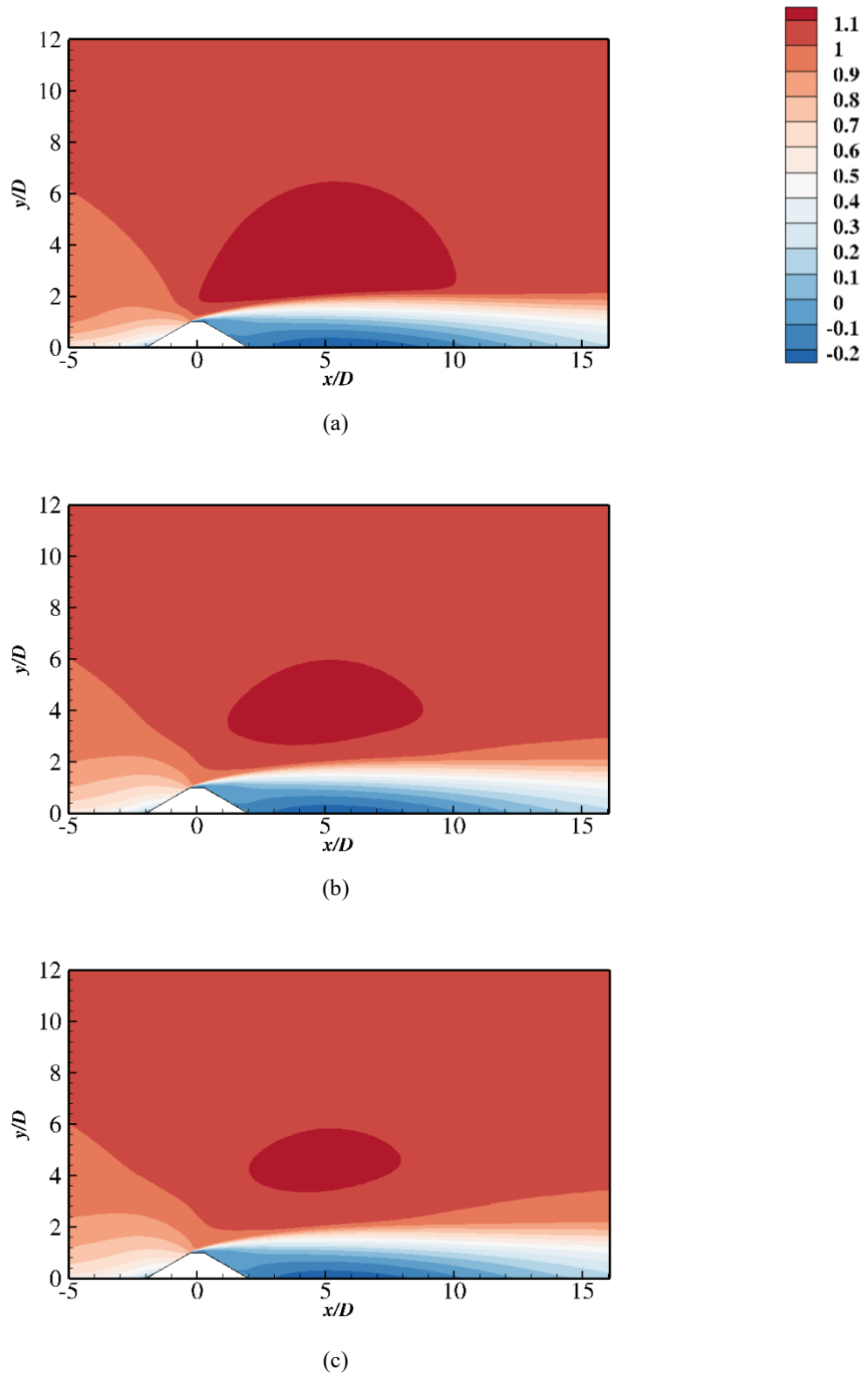
Figure A.24: Velocity contour for trapezoidal cylinder with $\alpha = 60°$ immersed at $Re = 2.0 \times 10^6$ with various boundary layer thicknesses (a) $\delta/D = 0.73$, (b) $\delta/D = 1.96$ and (c) $\delta/D = 2.52$.
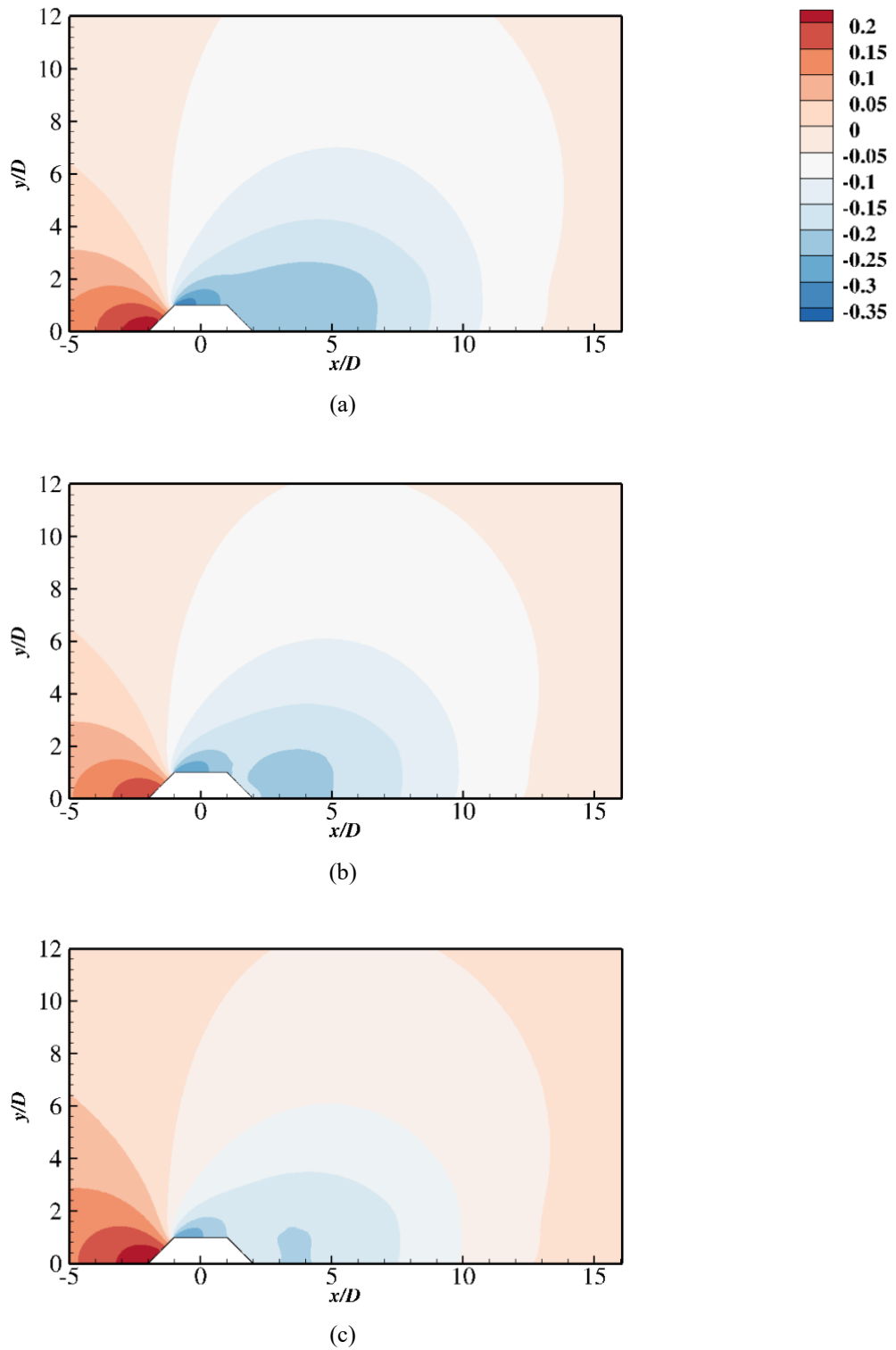
(a)



(b)



(c)
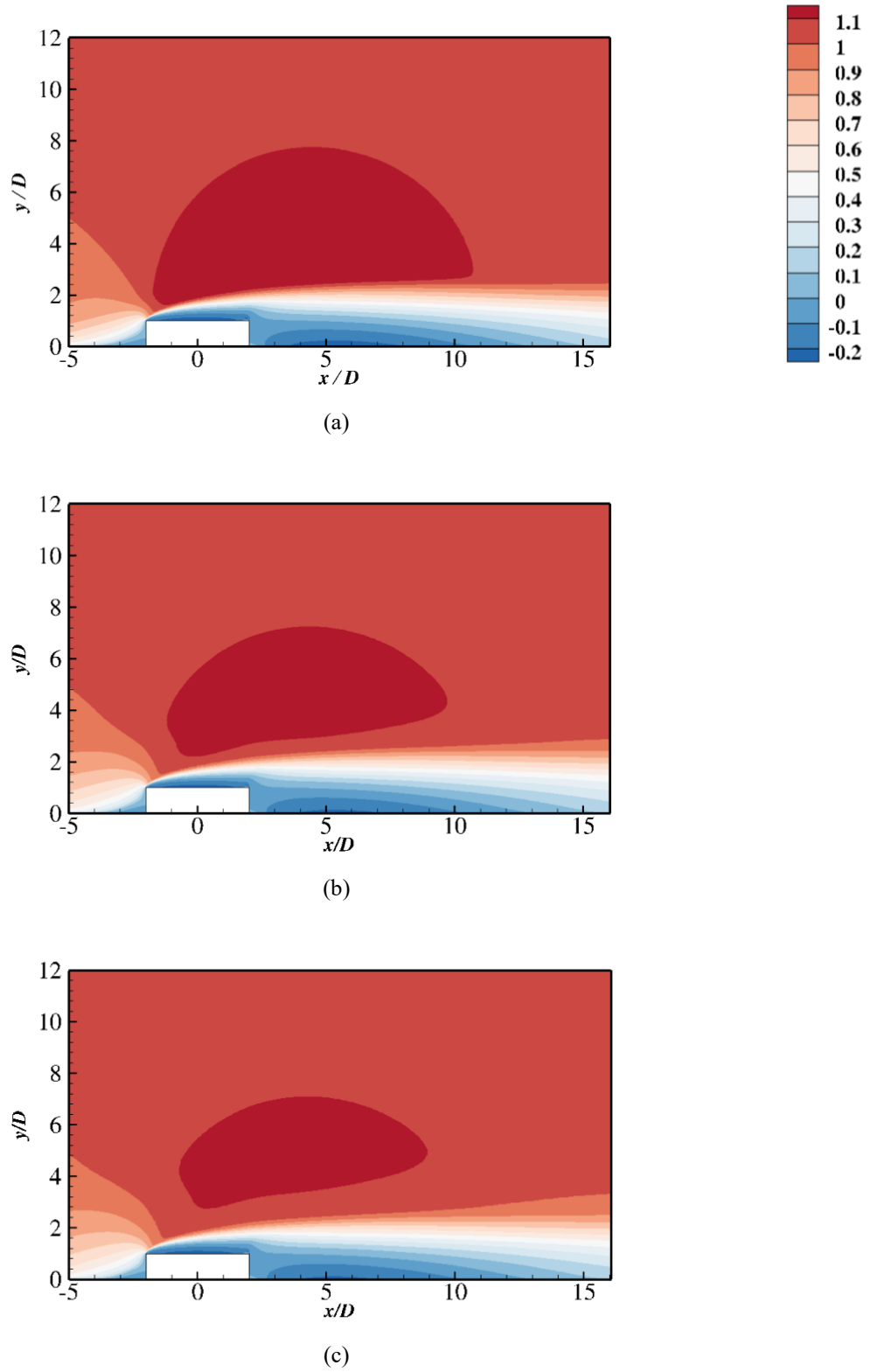
Figure A.25: Velocity contour for rectangular cylinder with $\alpha = 0°$ immersed at $Re = 0.5 \times 10^6$ with various boundary layer thicknesses (a) $\delta/D = 0.73$, (b) $\delta/D = 1.96$ and (c) $\delta/D = 2.52$.
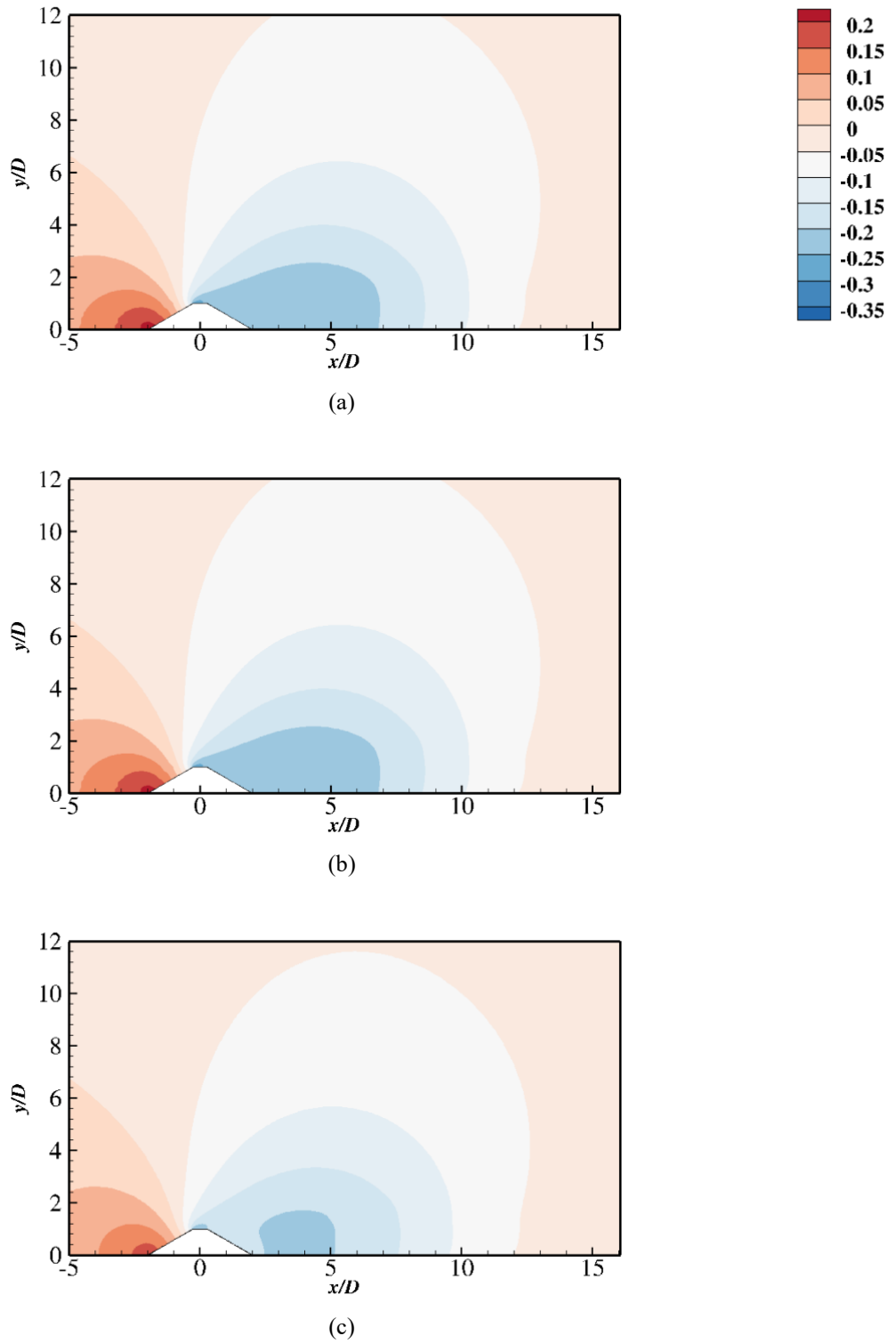
(a)



(b)



(c)
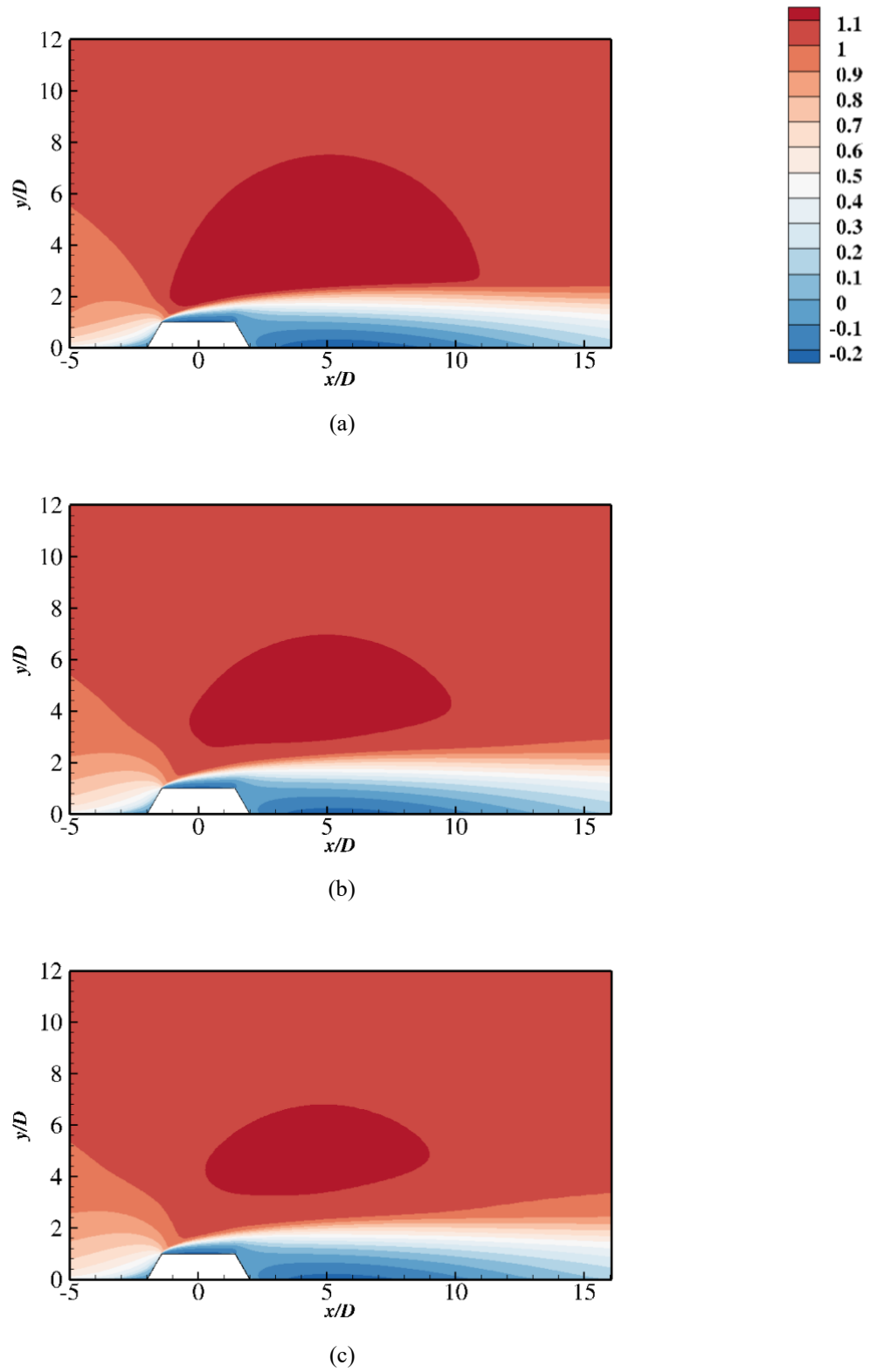
Figure A.26: Velocity contour for trapezoidal cylinder with $\alpha = 30°$ immersed at $Re = 0.5 \times 10^6$ with various boundary layer thicknesses (a) $\delta/D = 0.73$, (b) $\delta/D = 1.96$ and (c) $\delta/D = 2.52$.
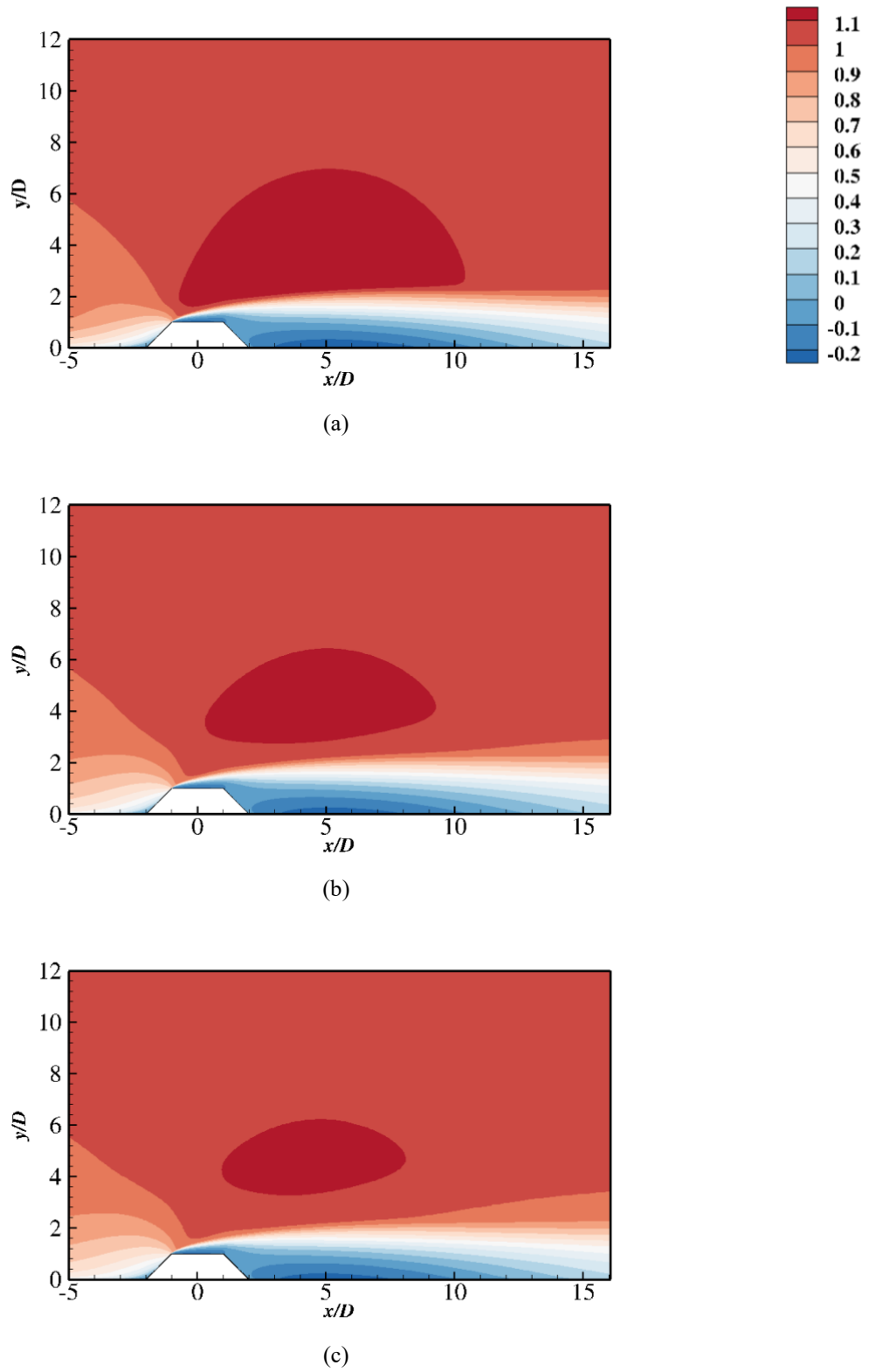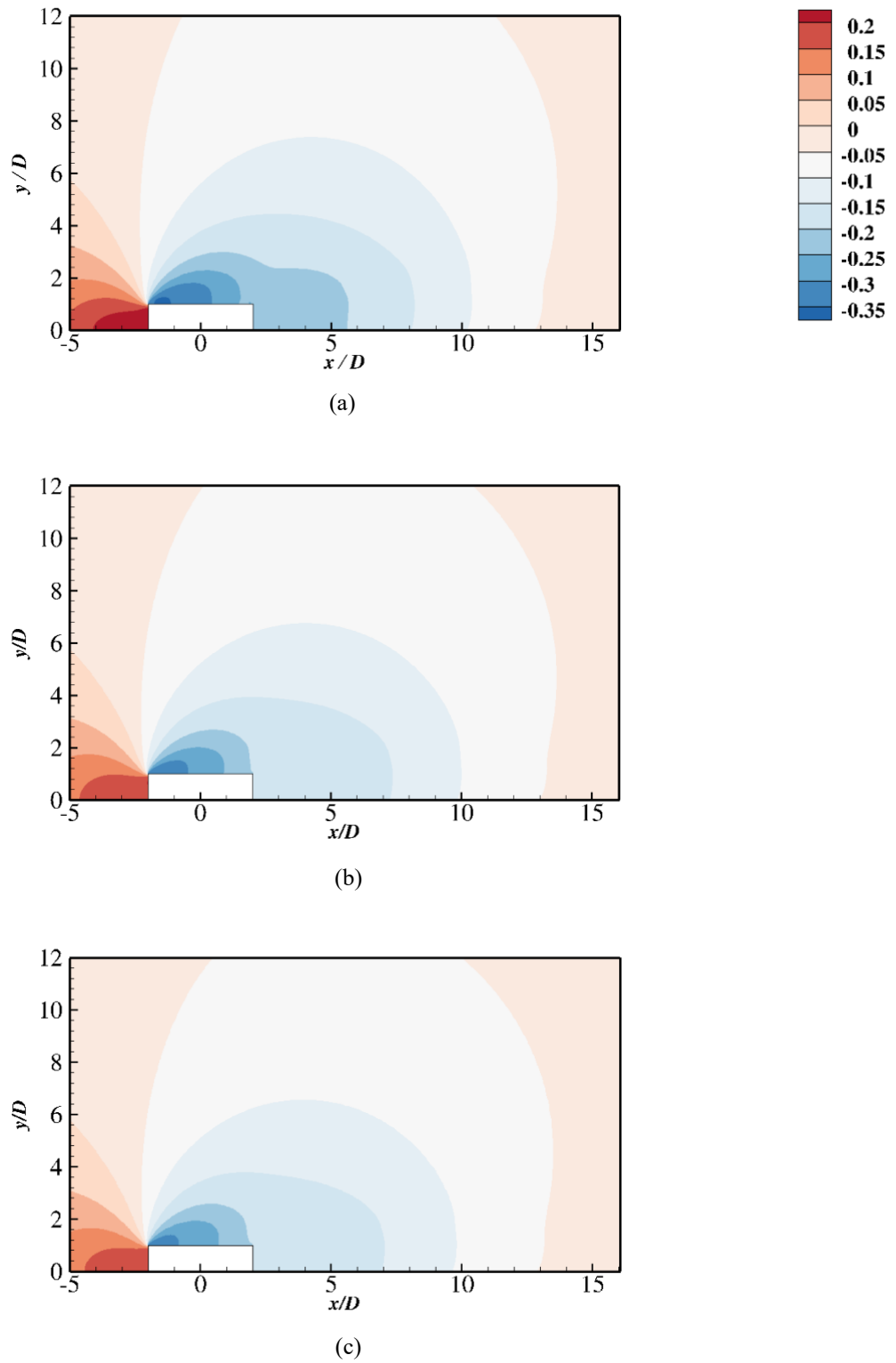
Figure A.27: Velocity contour for trapezoidal cylinder with $\alpha = 45°$ immersed at $Re = 0.5 \times 10^6$ with various boundary layer thicknesses (a) $\delta/D = 0.73$, (b) $\delta/D = 1.96$ and (c) $\delta/D = 2.52$.
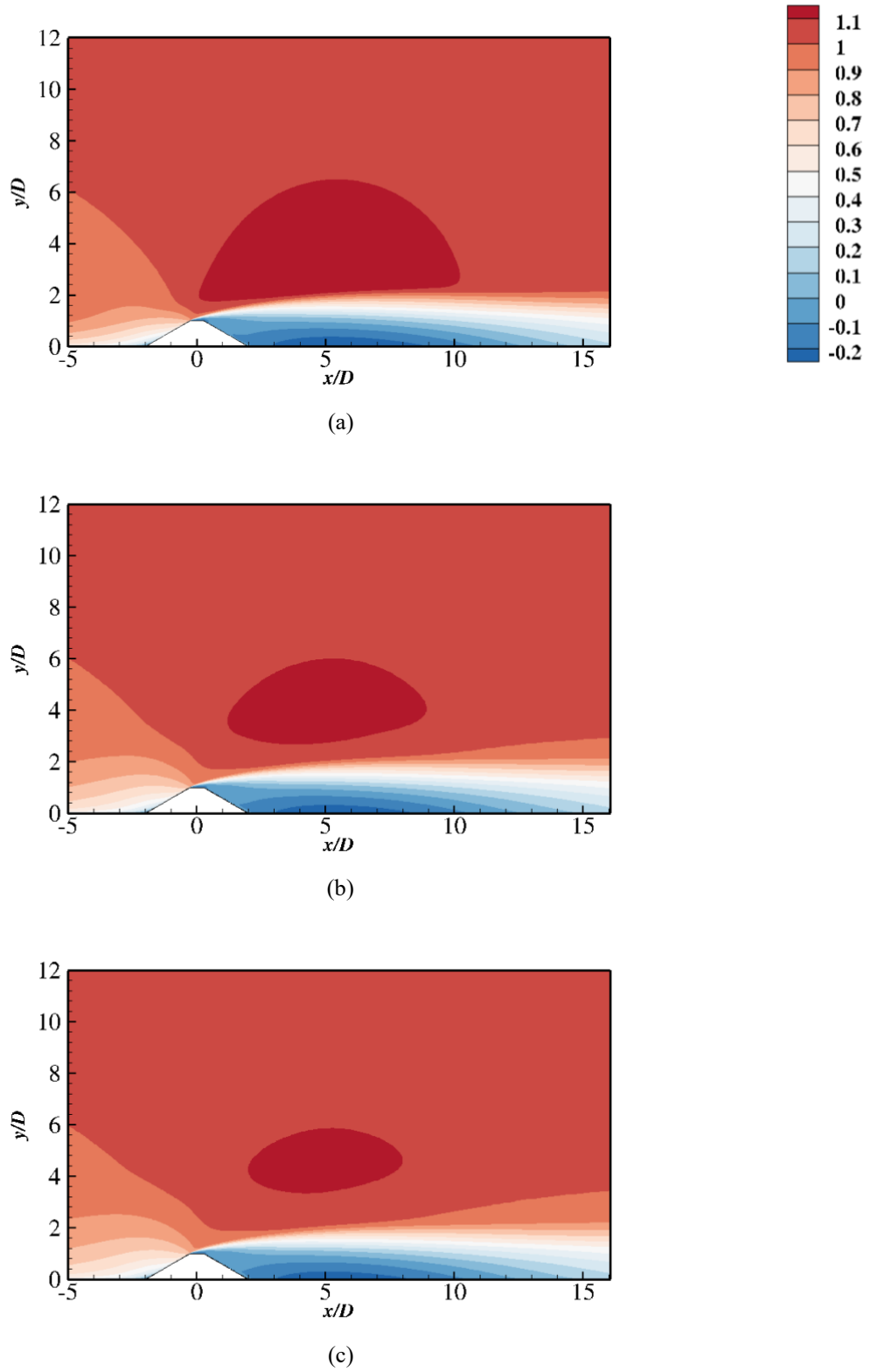
Figure A.28: Velocity contour for trapezoidal cylinder with $\alpha = 60°$ immersed at $Re = 0.5 \times 10^6$ with various boundary layer thicknesses (a) $\delta/D = 0.73$, (b) $\delta/D = 1.96$ and (c) $\delta/D = 2.52$.

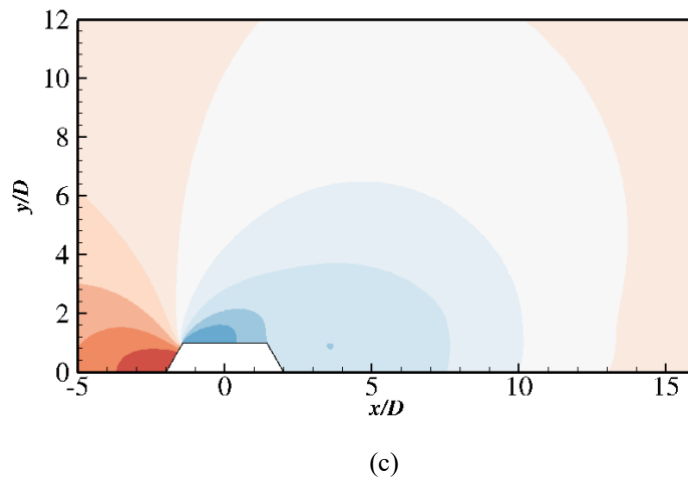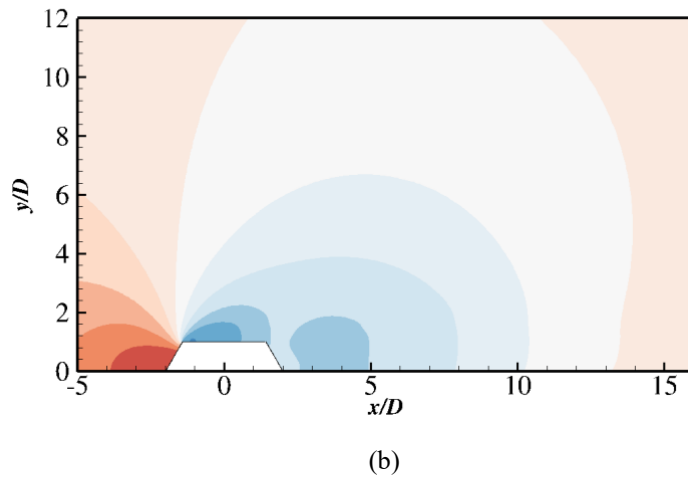# Appendix F  Pressure Distribution



(a)

(b)

(c)

Figure A.29: Pressure distribution for the rectangular cylinder with $\alpha = 0°$ at $Re = 1.0 \times 10^6$ with various boundary layer thicknesses (a) $\delta/D = 0.73$, (b) $\delta/D = 1.96$ and (c) $\delta/D = 2.52$.
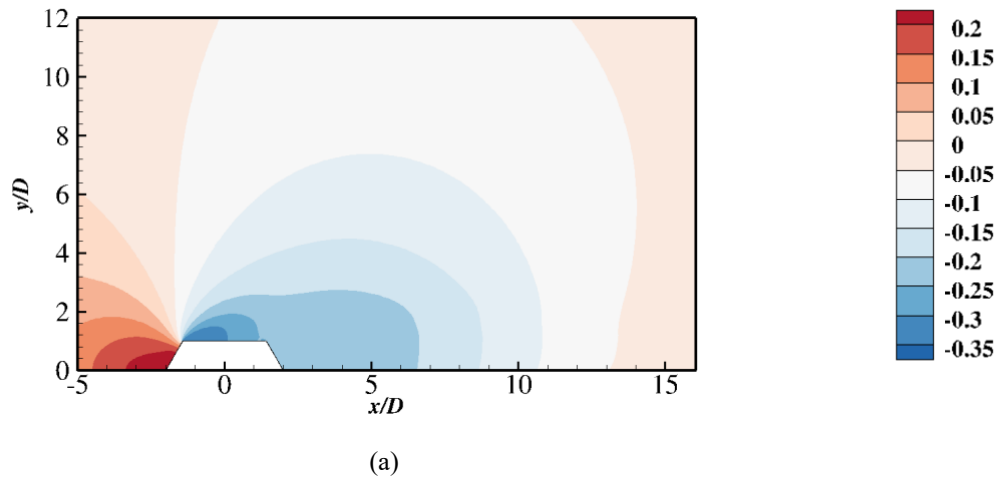
Figure A.30: Pressure distribution for the trapezoidal cylinder with $\alpha = 30°$ at $Re = 1.0 \times 10^6$ with various boundary layer thicknesses (a) $\delta/D = 0.73$, (b) $\delta/D = 1.96$ and (c) $\delta/D = 2.52$.

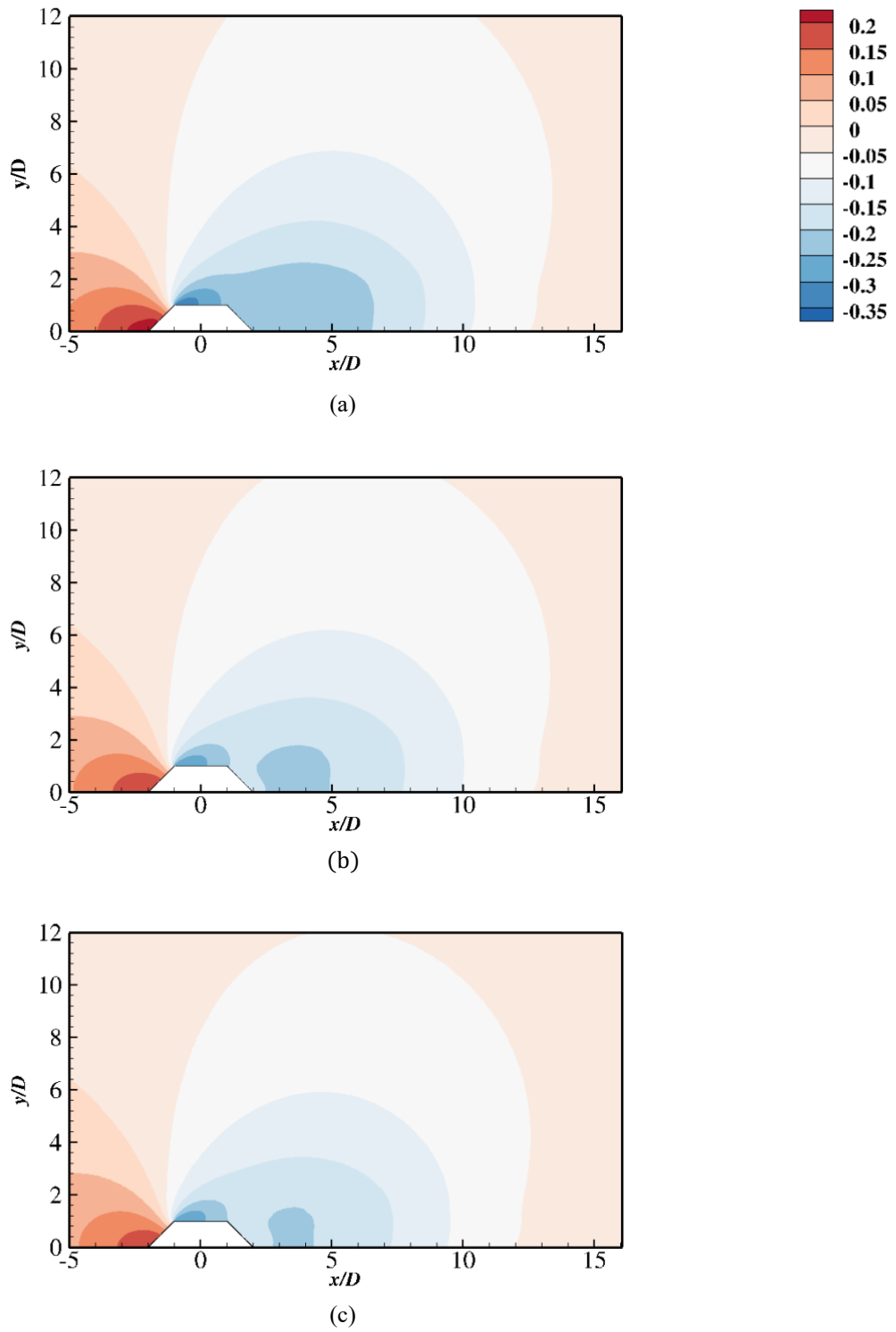Figure A.31: Pressure distribution for the trapezoidal cylinder with $\alpha = 45°$ at $Re = 1.0 \times 10^6$ with various boundary layer thicknesses (a) $\delta/D = 0.73$, (b) $\delta/D = 1.96$ and (c) $\delta/D = 2.52$.

Figure A.32: Pressure distribution for the trapezoidal cylinder with $\alpha = 60^{\circ}$ at $\mathrm{Re} = 1.0 \times 10^6$ with various boundary layer thicknesses (a) $\delta/D = 0.73$, (b) $\delta/D = 1.96$ and (c) $\delta/D = 2.52$.

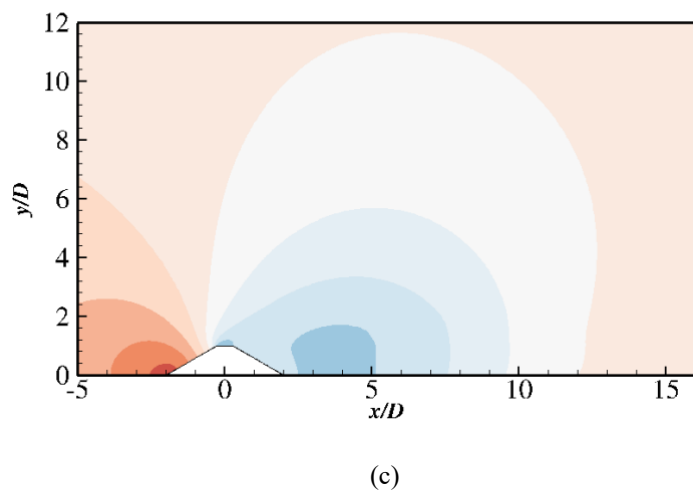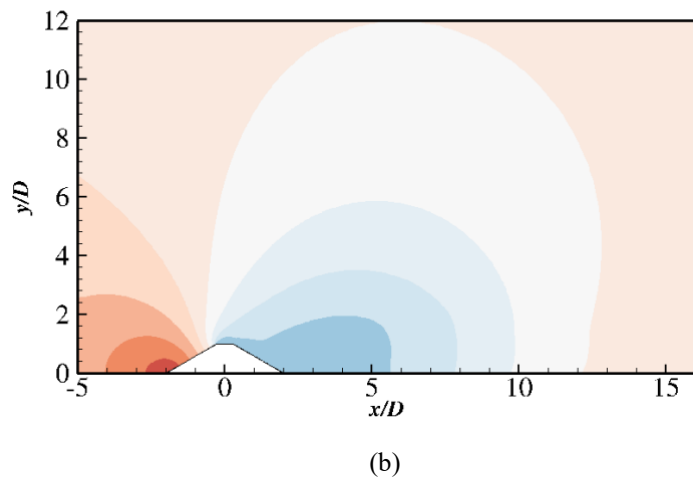Figure A.33: Pressure distribution for the rectangular cylinder with $\alpha = 0°$ at $\mathrm{Re} = 2.0 \times 10^6$ with various boundary layer thicknesses (a) $\delta/D = 0.73$, (b) $\delta/D = 1.96$ and (c) $\delta/D = 2.52$.
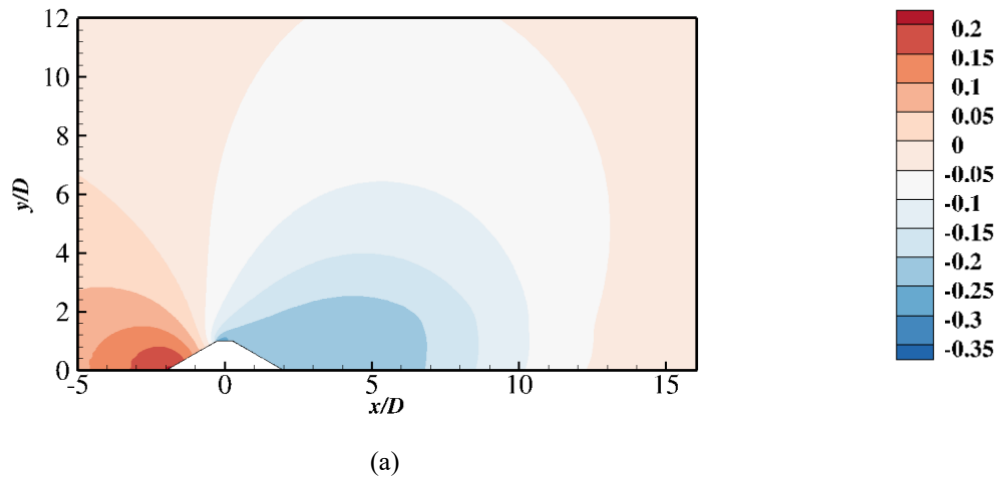
Figure A.34: Pressure distribution for the trapezoidal cylinder with $\alpha = 30°$ at $\text{Re} = 2.0 \times 10^6$ with various boundary layer thicknesses (a) $\delta/D = 0.73$, (b) $\delta/D = 1.96$ and (c) $\delta/D = 2.52$.

Figure A.35: Pressure distribution for the trapezoidal cylinder with $\alpha = 45°$ at $Re = 2.0 \times 10^6$ with various boundary layer thicknesses (a) $\delta/D = 0.73$, (b) $\delta/D = 1.96$ and (c) $\delta/D = 2.52$.

Figure A.36: Pressure distribution for the trapezoidal cylinder with $\alpha = 60°$ at $Re = 2.0 \times 10^6$ with various boundary layer thicknesses (a) $\delta/D = 0.73$, (b) $\delta/D = 1.96$ and (c) $\delta/D = 2.52$.
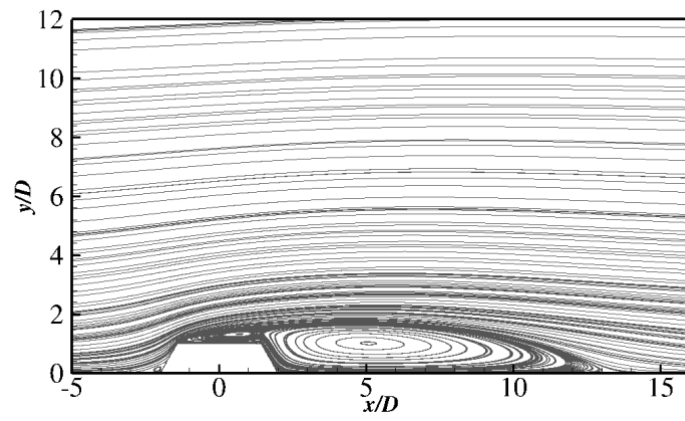
Figure A.37: Pressure distribution for the rectangular cylinder with $\alpha = 0°$ at Re $= 0.5 \times 10^6$ with various boundary layer thicknesses (a) $\delta/D = 0.73$, (b) $\delta/D = 1.96$ and (c) $\delta/D = 2.52$.
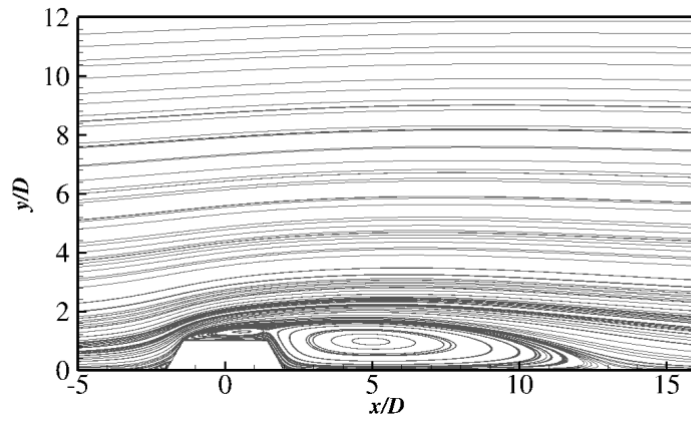
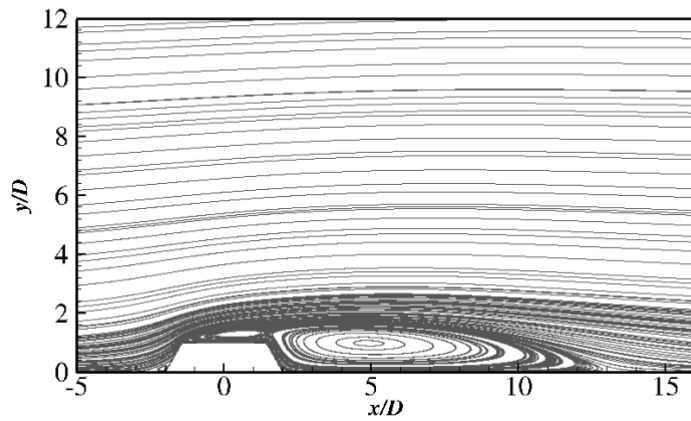Figure A.38: Pressure distribution for the rectangular cylinder with $\alpha = 30°$ at $Re = 0.5 \times 10^6$ with various boundary layer thicknesses (a) $\delta/D = 0.73$, (b) $\delta/D = 1.96$ and (c) $\delta/D = 2.52$.

Figure A.39: Pressure distribution for the rectangular cylinder with $\alpha = 45°$ at $Re = 0.5 \times 10^6$ with various boundary layer thicknesses (a) $\delta/D = 0.73$, (b) $\delta/D = 1.96$ and (c) $\delta/D = 2.52$.

Figure A.40: Pressure distribution for the rectangular cylinder with $\alpha = 60°$ at $Re = 0.5 \times 10^6$ with various boundary layer thicknesses (a) $\delta/D = 0.73$, (b) $\delta/D = 1.96$ and (c) $\delta/D = 2.52$.
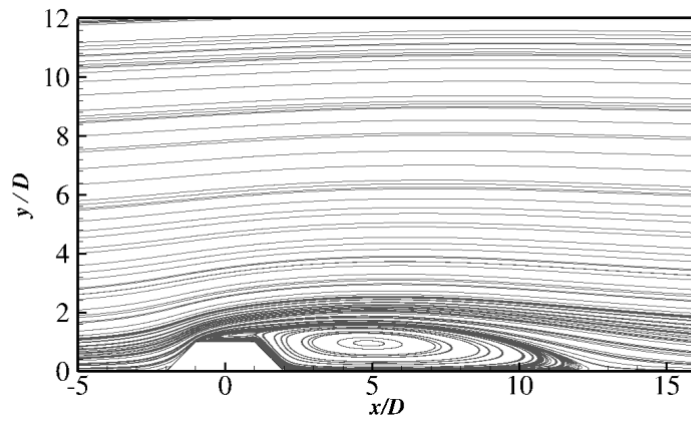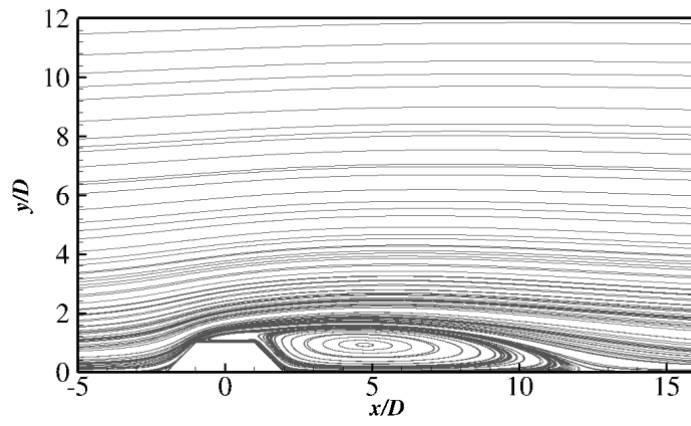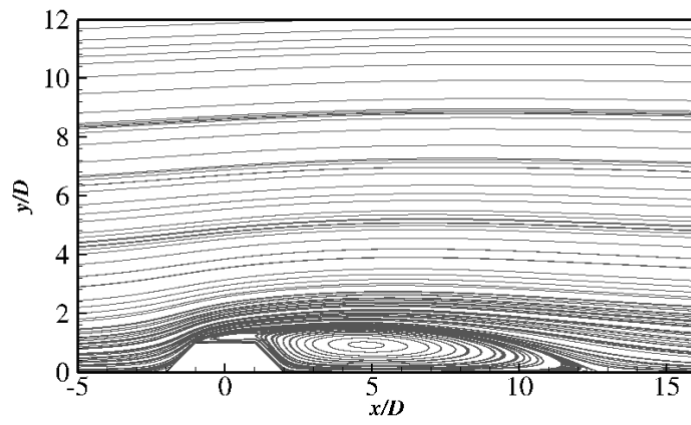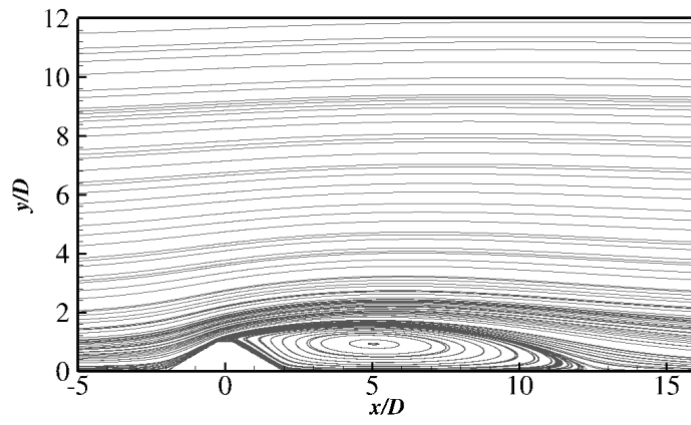
# Appendix G  Stream Lines
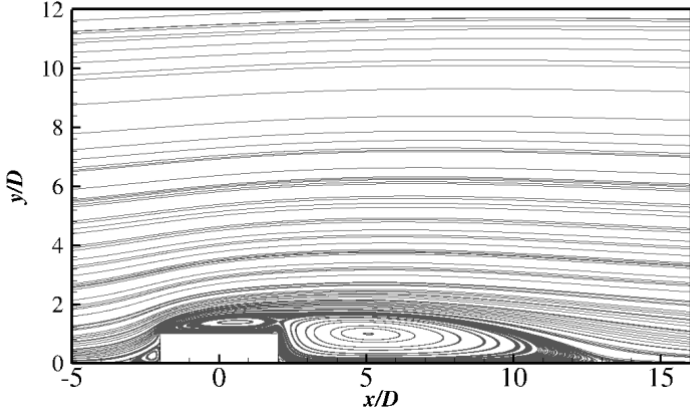


(a)
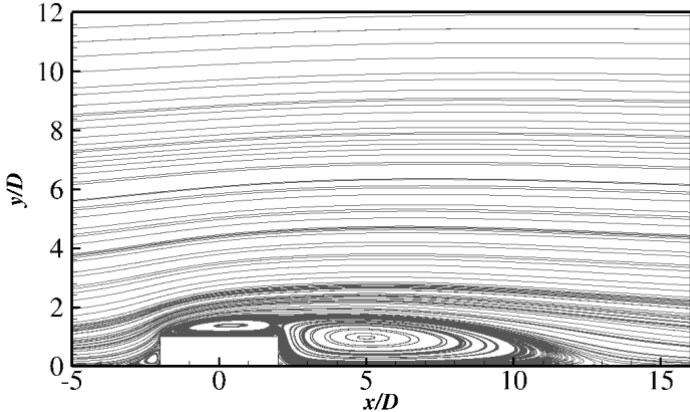


(b)
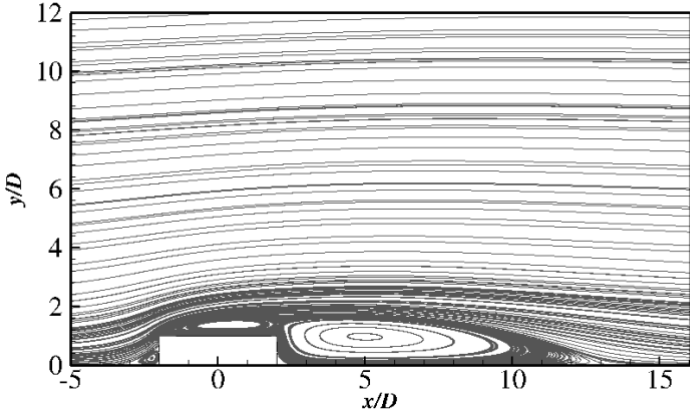


(c)

Figure A.41: Stream lines for rectangular cylinder with $\alpha = 0^\circ$ at $Re = 1 \times 10^6$ with various boundary layer thicknesses (a) $\delta/D = 0.73$, (b) $\delta/D = 1.96$ and (c) $\delta/D = 2.52$.

Figure A.42: Stream lines for rectangular cylinder with $\alpha = 30^\circ$ at Re $= 1 \times 10^6$ with various boundary layer thicknesses (a) $\delta/D = 0.73$, (b) $\delta/D = 1.96$ and (c) $\delta/D = 2.52$.
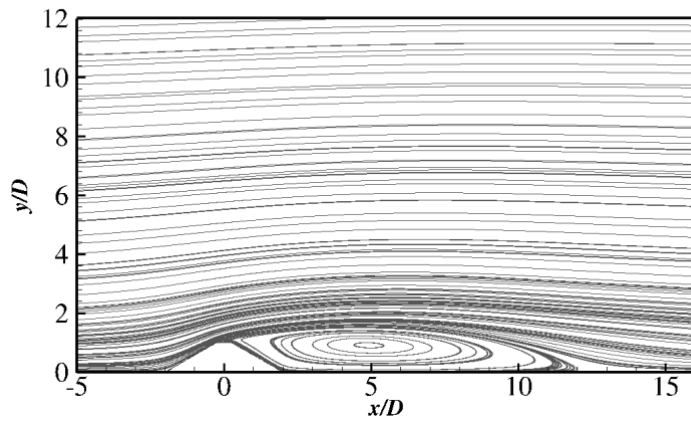
(a)



(b)



(c)

Figure A.43: Stream lines for rectangular cylinder with $\alpha = 45°$ at $Re = 1 \times 10^6$ with various boundary layer thicknesses (a) $\delta/D = 0.73$, (b) $\delta/D = 1.96$ and (c) $\delta/D = 2.52$.
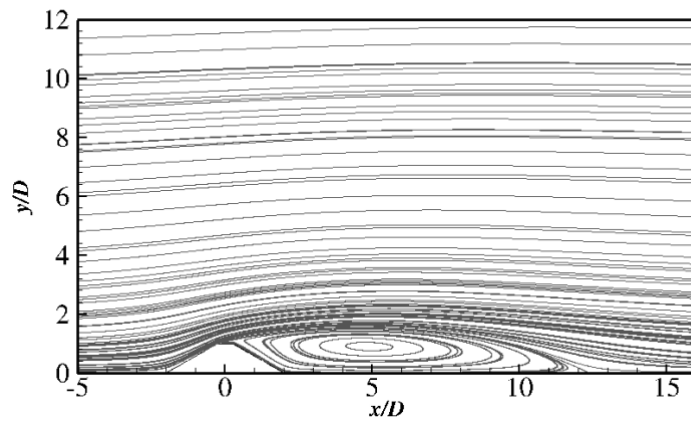
(a)



(b)



(c)

Figure A.44: Stream lines for rectangular cylinder with $\alpha = 60°$ at $Re = 1 \times 10^6$ with various boundary layer thicknesses (a) $\delta/D = 0.73$, (b) $\delta/D = 1.96$ and (c) $\delta/D = 2.52$.